APPLICATIONS OF MULTI-REDUCTION AND MULTI-SOLITON ANALYSIS OF (2+1) ZAKHAROV-KUZNETSOV (ZK) EQUATION

Ali Raza[a,b], **Abdul Hamid Kara**[c], **Sibusiso Moyo**[d]

[a] Department of Mathematics and Statistical Sciences, Lahore School of Economics, Lahore, Pakistan
[b] Department of Mathematical Sciences, University of Stellenbosch, Stellenbosch, South Africa
[c] School of Mathematics, University of the Witwatersrand, Johannesburg, South Africa
[d] School for Data Science and Computational Thinking and Department of Mathematical Sciences, Stellenbosch University, Stellenbosch, 7602, South Africa
[*] Corresponding Author e-mail: Abdul.Kara@wits.ac.za

We study the Zakharov-Kuznetsov (ZK) equation with the triple-power law non-linearity. We determine the invariance properties and construct classes of conservation laws and show how the relationship leads to double reductions of the systems, yielding stable solutions such as travelling waves and solitons. This relationship is determined by recent results involving 'multipliers' that lead to 'total divergent systems'. Multi-solitons analysis is performed using invariance transformation, producing stable multi-soliton structures, alongside vortex soliton solutions that exhibit localized, bell-shaped profiles. A comparison between symmetry and multi-reduction is presented, highlighting the efficacy in achieving integrable outcomes. The physical interpretation of soliton solutions is also discussed in this study, emphasizing their stable propagation and relevance to modeling coherent ion-acoustic and vortex waves in magnetized plasmas.

Keywords: *Double Reduction; Conservation Laws; Multipliers; Zakharov-Kuznetsov Equation; Invariance analysis; Solitons; Multi-solitons; Vortex solitons*

PACS: 02.30.Jr; 02.30.Hq; 47.10.ab; 52.35.-g

1. INTRODUCTION AND BACKGROUND

A large class of equations in space science and mathematical physics are special cases of the Zakharov-Kuznetsov (ZK) equation

$$u_t + G(u)u_x + \sigma(u_{xx} + u_{yy})_x = 0. \tag{1}$$

For example, the triple-power law non-linearity [1] is given by $G(u) = au^n + bu^{2n} + cu^{3n}$, which will be the main focus here. Various other versions have been studied, inter Biswas, A and Zerrad [2]. The Zakharov-Kuznetsov (ZK) equation is used to model non-linear ion-acoustic waves [3] through a plasma [4, 5] in the presence of a magnetic field and also construed as an extension of the Korteweg-de Vries (KdV) equation in higher dimension, where the u_{xxx} and u_{xyy} are levels of dispersion. The ZK equation plays a valuable role for understanding multidimensional wave phenomena in plasma physics [6, 7] to study ion-acoustic solitons [8] that maintain shape and weak turbulence. With applications in space physics and fusion research, the ZK equation offers opportunities to explore facts regarding wave interactions, stability, and turbulence in two and three-dimensional plasma systems by building non-linearity and dispersive effects.

The Lie symmetry approach is now an established route for the reduction of differential equations and its advantages in the analysis of nonlinear partial differential equations (PDEs) is vast. The method centres around the algebra of one parameter Lie groups of transformations that are admitted by the PDE; once known, the reduction of the PDE is standard and may lead to exact (symmetry invariant) solutions [9, 10].

There are a number of reasons to find conserved densities of PDEs. Some conservation laws are physical (e.g., conservation of momentum and energy) and others facilitate analysis of the PDE and predicts integrability. Also, some reasons are related to the numerical solution of PDEs. For example, one should check whether the conserved quantities are in fact constant [11]. For instance, if $u = u(t, x, y)$ and $u \to 0$ for $|x| \to \pm\infty$, the conserved form $D_t\Phi^t + D_x\Phi^x + D_y\Phi^y = 0$ implies

$$\int_{-\infty}^{\infty} D_t\Phi^t = constant, \tag{2}$$

for all solutions of the PDE. Lastly, the use of symmetry properties of a given system of partial differential equations to construct or generate new conservation laws from known conservation laws has been investigated extensively [12–14].

We will discuss the line travelling wave reductions for ZK equation (1) with a 2-dimensional symmetry algebra in (2+1)-dimensions such as line solitons and eikonal waves, via invariance under two commuting translations given by

$$X_1 = \left(\mu^2 + \nu^2\right)\partial_t + \mu\partial_x + \nu\partial_y, \quad X_2 = \nu\partial_x - \mu\partial_y. \tag{3}$$

Reduction under the above type of commuting translation symmetries is very common in applications and yields interesting types of solutions called line travelling wave solutions, under similarity invariant transformations, $\zeta = \mu x + \nu y - t$ and $u(t, x, y) = U(\zeta)$. The physics of the line travelling wave is presented in [15] and yields the solutions corresponding to the reduction

$$u(t, x, y) \rightarrow U(\zeta), \tag{4}$$

and satisfy the reduced ODE obtained from the PDE via double reduction under the condition of symmetry invariance that is associated with a conservation laws and can be expressed by the canonical transformation

$$(\partial_t, \partial_x, \partial_y, \partial_u) \rightarrow (\partial_\zeta, \partial_\rho, \partial_\chi, \partial_\nu), \tag{5}$$

under

$$x \rightarrow \zeta = \mu x + \nu y - t, \tag{6}$$
$$y \rightarrow \rho = c^2 t; \quad c = 1/\sqrt{\mu^2 + \nu^2}, \tag{7}$$
$$t \rightarrow \chi = \frac{x}{\nu} \quad (\text{or} = -\frac{y}{\mu}), \tag{8}$$
$$u \rightarrow u = U(\zeta), \tag{9}$$

for which the pair of symmetries jointly take the form as

$$\mathrm{X}_1 = \partial_\rho, \quad \mathrm{X}_2 = \partial_\chi. \tag{10}$$

This transformations sends a conservation law $\mathrm{Div}(T, \Phi^x, \Phi^y) = 0$ to an equivalent canonical form $\mathrm{Div}(\bar{T}, \bar{\Phi}^\rho, \bar{\Phi}) = 0$ and can be expressed in conserved vector form

$$(T, \Phi^x, \Phi^y) \rightarrow (\bar{T}, \bar{\Phi}^\rho, \bar{\Phi}^\chi) \tag{11}$$

Finally, the reduction of conservation laws can be obtained as every invariant conservation law $D_\zeta \bar{T} + D_\rho \bar{\Phi}^\rho + D_\chi \bar{\Phi}^\chi = 0$ reduces to $D_\zeta \Psi = 0$ which is a first integral $\Psi = k_1$, where k_1 is a constant. The explicit formula for the first integral is given by

$$\Psi(\zeta, U, U', \ldots) = \bar{T} + \int \left(\partial_\rho \bar{\Phi}^\rho + \partial_\chi \bar{\Phi}^\chi \right) d\zeta.$$

This is important to note that the double reduction can only be carried out if the conservation law (T, Φ^x, Φ^y) is associated with X_1 and X_2, as studied in [12]. Since association of symmetries with conservation laws is challenging and the calculations are tedious, the symmetry association with conservation laws is equivalent to and can easily be built using multipliers instead of conservation laws. The association of symmetry with a multiplier is studied in [16].

2. SYMMETRY GENERATORS AND CONSERVATION LAWS

We now present some preliminaries [17, 18] [19, 20]. Consider an rth-order system of partial differential equations (PDEs) of n independent variables $x = (x^1, x^2, \ldots, x^n)$ and m dependent variables $u = (u^1, u^2, \ldots, u^m)$

$$G^\mu(x, u, u_{(1)}, \ldots, u_{(r)}) = 0, \quad \mu = 1, \ldots, \tilde{m}, \tag{12}$$

where $u_{(1)}, u_{(2)}, \ldots, u_{(r)}$ denote the collections of all first, second, ..., rth-order partial derivatives, that is, $u_i^\alpha = D_i(u^\alpha), u_{ij}^\alpha = D_j D_i(u^\alpha), \ldots$ respectively, with the total differentiation operator with respect to x^i given by

$$D_i = \frac{\partial}{\partial x^i} + u_i^\alpha \frac{\partial}{\partial u^\alpha} + u_{ij}^\alpha \frac{\partial}{\partial u_j^\alpha} + \ldots, \quad i = 1, \ldots, n, \tag{13}$$

where the summation convention is used whenever appropriate. A current $\Phi = (\Phi^1, \ldots, \Phi^n)$ is conserved if it satisfies

$$D_i \Phi^i = 0, \tag{14}$$

along the solutions of (12). It can be shown that every admitted conservation law arises from *multipliers* $Q_\mu(x, u, u_{(1)}, \ldots)$ such that

$$Q_\mu G^\mu = D_i \Phi^i, \tag{15}$$

holds identically (i.e., off the solution space) for some current Φ^i.

We determine the conserved flows by first constructing the multipliers Q_μ which are obtained by noting that **the Euler(-Lagrange) operator, $\frac{\delta}{\delta u^\alpha}$, annihilates total divergences**, i.e., a defining equation, for Q_μ, would be

$$\frac{\delta}{\delta u^\alpha}[Q_\mu G^\mu] = 0. \tag{16}$$

The conserved flow Φ may be obtained in a number of ways, for instance, by a well known 'homotopy' formula. We consider second multiplier in the space of $(x, y, t, u, u_x, u_t, u_y, u_{xx}, u_{tx}, u_{xy}, u_{ty}, u_{yy}, u_{tt})$ given by

$$Q := f\left(x, y, t, u, u_x, u_t, u_y, u_{xx}, u_{tx}, u_{xy}, u_{ty}, u_{yy}, u_{tt}\right)$$

The symbolic computation provide us the set of multipliers for ZK equation (1) given by

$$Q = c_1 u_{tt} + c_1 u_{xx} + \frac{c_1 u^{n+1}}{\sigma(n+1)} + \frac{bc_1 u^{2n+1}}{\sigma(2n+1)} + \frac{cc_1 u^{3n+1}}{\sigma(3n+1)} + c_2 u + F(y)$$

The multiplier Q_1 is arbitrary function of y given by

$$Q_1 = F(y) = y.$$

Multiplier Q_2 and Q_3 are

$$Q_2 = u, \quad Q_3 = u_{tt} + u_{xx} + \frac{u^{n+1}}{\sigma(n+1)} + \frac{bu^{2n+1}}{\sigma(2n+1)} + \frac{cu^{3n+1}}{\sigma(3n+1)}.$$

The Conservation laws corresponding to multiplier $Q_1 = 1$ and $Q_2 = u$ respectively are given by

$$(T_1, \Phi_1^y, \Phi_1^x) = (u, \tfrac{2}{3}\sigma u_{xy}, \tfrac{1}{6n^3+11n^2+6n+1}[6n^3\sigma u_{xx} + 2n^3\sigma u_{yy} + 6u^{n+1}an^2 + 3u^{2n+1}bn^2$$
$$+2u^{3n+1}cn^2 + 11n^2\sigma u_{xx} + \tfrac{11}{3}n^2\sigma u_{yy} + 5u^{n+1}an + 4u^{2n+1}bn + 3u^{3n+1}cn$$
$$+6n\sigma u_{xx} + 2n\sigma u_{yy} + u^{n+1}a + u^{2n+1}b + u^{3n+1}c + \sigma u_{xx} + \tfrac{1}{3}\sigma u_{yy}]).$$

and

$$(T_1, \Phi_1^y, \Phi_1^x) = (\tfrac{1}{2}u^2, \tfrac{1}{3}\sigma\left(2uu_{xy} - u_x u_y\right), \tfrac{1}{18n^3+66n^2+72n+24}[-33n^2\sigma u_x{}^2 - 36n\sigma u_x{}^2$$
$$-9n^3\sigma u_x{}^2 + 30u^{2+n}an + 18u^{2+3n}cn - 3n^3\sigma u_y{}^2 - 11n^2\sigma u_y{}^2 - 12n\sigma u_y{}^2$$
$$+18u^{2+n}an^2 + 24u^{2+2n}bn + 6u^{2+3n}cn^2 + 9u^{2+2n}bn^2 + 24u\sigma u_{xx} + 8u\sigma u_{yy}$$
$$+12u^{2+n}a + 12u^{2+2n}b + 12u^{2+3n}c - 12\sigma u_x{}^2 - 4\sigma u_y{}^2 + 18n^3\sigma uu_{xx} + 66n^2\sigma uu_{xx}$$
$$+72n\sigma uu_{xx} + 6n^3\sigma uu_{yy} + 22n^2\sigma uu_{yy} + 24n\sigma uu_{yy}]).$$

In the next section, we will check the association of multipliers with symmetries so that we can use conservation law theorem to perform double reduction.

3. DOUBLE REDUCTION AND INVARIANT SOLUTIONS

Applications to double reductions has been studied in various ways [21, 22] via conservation Law theorem under double reduction theory. In this study, we discussed the double reduction via multiplier association. Furthermore, for the $(1 + 2)$ case, if $X = \xi\partial_x + \theta\partial_y + \tau\partial_t + \eta\partial_u$ is a Lie point symmetry that leaves a scalar PDE in (12), say,

$$G(x, t, u, u_x, u_y, u_t, u_{xx} \ldots) = 0, \tag{17}$$

invariant with

$$XG = RG, \tag{18}$$

and

$$\lambda = D_t\tau + D_x\xi + D_y\theta, \tag{19}$$

such that

$$XQ + (R + \lambda)Q = 0, \tag{20}$$

then X is associated with the corresponding conserved flow $\Phi = (T, \phi^x, \phi^y)$ and, via X and Φ, double reduction may be obtained [15, 16]. Here, $D_t T + D_x \phi^x + D_y \phi^y = 0|_{(17)}$. Moreover, in transformed coordinates (ζ, ρ, χ, U), $\bar{X}_1 = \partial_\rho$ and $\bar{X}_2 = \partial_\chi$ so that

$$X_1(\rho) = 1, \qquad X_2(\chi) = 1,$$

and $\bar{\Phi} = (\bar{T}, \phi^\rho, \phi^\chi)$ leads to $D_\zeta \bar{T} + D_\rho \phi^\rho + D_\chi \phi^\chi = 0$. Thus,

$$D_t T + D_x \phi^x + D_y \phi^y = -\frac{dT}{d\zeta} + c^2 \frac{dT}{d\rho} + \mu \frac{d\Phi^x}{d\zeta} + \frac{1}{\nu} \frac{d\Phi^x}{d\chi} + \nu \frac{d\Phi^y}{d\zeta}, \tag{21}$$

so that

$$\begin{aligned} \bar{T} &= -T + \mu \Phi^x + \nu \Phi^y, \\ \phi^\rho &= c^2 T, \\ \phi^\chi &= \tfrac{1}{\nu} \Phi^x. \end{aligned} \tag{22}$$

Finally, we obtain the double reduction of the original system by following

$$\Psi = \bar{T} + \int_{-\infty}^{\infty} (\frac{d\Phi^\rho}{d\rho} + \frac{d\Phi^\chi}{d\chi}) d\zeta = 0. \tag{23}$$

given by

$$k = \bar{T}|_{\zeta, U, U', \dots}, \tag{24}$$

where k is a constant - for details, see [15]. Finally the equation (24) provide us reduced ODEs, which are second order ODEs given by

$$\begin{aligned} \mu (1+n)b(1+3n)U(\zeta)^{1+2n} &- 6(-\tfrac{1}{3} c\mu (1+n)U(\zeta)^{1+3n} \\ +(-\mu \sigma (\mu^2 + \nu^2)(1+n)\tfrac{d^2}{d\zeta^2}U(\zeta) &- U(\zeta)^{1+n} a\mu \\ +U(\zeta)(1+n))(\tfrac{1}{3}+n))(\tfrac{1}{2}+n) &= k_1(6n^3 + 11n^2 + 6n + 1), \end{aligned} \tag{25}$$

ODE (25) is second order reducible ODE with missing independent variable ζ.

$$\frac{d^2}{d\zeta^2}U(\zeta) = \frac{1}{6} \frac{C}{(1+n)\mu\sigma(\mu^2 + \nu^2)(\tfrac{1}{3}+n)(\tfrac{1}{2}+n)}, \tag{26}$$

where

$$\begin{aligned} C = [k_1(6n^3 + 11n^2 + 6n + 1) &- 3\mu(1+n)b(\tfrac{1}{3}+n)(U(\zeta))^{1+2n} \\ +6(-\tfrac{1}{3}c\mu(1+n)(U(\zeta))^{1+3n} &+ (-(U(\zeta))^{1+n}a\mu \\ +U(\zeta)(1+n))(\tfrac{1}{3}+n))(\tfrac{1}{2}+n)]. \end{aligned}$$

For $n = 1$, (27) has solution in integral representation takes the form given by

$$\zeta - \left(\int^{U(\zeta)} \frac{30\mu\sigma(\mu^2 + \nu^2)}{\sqrt{-30\mu\sigma(\mu^2+\nu^2)(3\Omega^5 c\mu + 5\Omega^4 b\mu + 10\Omega^3 a\mu + 60c_1\mu^3\sigma + 60c_1\mu\nu^2\sigma - 30\Omega^2 - 60\Omega_1)}} d\Omega \right) - c_2 = 0$$

On the other hand, ODE (27) is second order non-linear ODE with missing independent variable ζ presented by

$$\begin{aligned} 3(\tfrac{2}{3}+n)\mu(2+n)b(U(\zeta))^{2+2n} &+ 6(1+n)(\tfrac{1}{3}c\mu(2+n)(U(\zeta))^{2+3n} \\ +((U(\zeta))^{2+n}a\mu - \tfrac{1}{2}(-2\mu\sigma U(\zeta)(\mu^2+\nu^2)\tfrac{d^2}{d\zeta^2}U(\zeta) &+ \mu\sigma(\mu^2+\nu^2)(\tfrac{d}{d\zeta}U(\zeta))^2 \\ +(U(\zeta))^2)(2+n))(\tfrac{2}{3}+n)) &= k_2(6n^3 + 22n^2 + 24n + 8). \end{aligned} \tag{27}$$

For $n = 1$, (27) has solution in its integral representation given by

$$\int^{U(\zeta)} \left(-\frac{\sqrt{30}\mu\sigma(\mu^2 + \nu^2)}{\sqrt{\mu\sigma(\mu^2+\nu^2)(-3\Omega^5 c\mu - 5\Omega^4 b\mu + 30\Omega\mu^3\sigma c_1 + 30\Omega\mu\nu^2\sigma c_1 - 10\Omega^3 a\mu + 30\Omega^2 - 60k_2)}} \right) d\Omega - \zeta - c_2 = 0$$

3.1. Analysis of ODE (25) and Travelling Wave Solution

An analysis of (25) is presented in this section. ODE (25) can further reduce using invariance analysis. The ODE (25) reduces to first order ODE by single reduction using the symmetry $X_1 = \partial\zeta$. The reduced ODE is given by

$$6w(\alpha)\left(\tfrac{d}{d\alpha}w(\alpha)\right)\mu n^3 \nu^2\sigma + 11w(\alpha)\left(\tfrac{d}{d\alpha}w(\alpha)\right)\mu n^2 \nu^2\sigma + 6w(\alpha)\left(\tfrac{d}{d\alpha}w(\alpha)\right)\mu n\nu^2\sigma$$

$$+3\,\mu\,b\alpha^{1+2\,n}n^2 + 2\,c\mu\,\alpha^{1+3\,n}n^2 + 6\,n^2\alpha^{1+n}a\mu + 4\,\mu\,b\alpha^{1+2\,n}n + 3\,c\mu\,\alpha^{1+3\,n}n$$

$$+5\,n\alpha^{1+n}a\mu + w\,(\alpha)\left(\frac{d}{d\alpha}w\,(\alpha)\right)\mu^3\sigma + \alpha^{1+n}a\mu + \mu\,b\alpha^{1+2\,n} + c\mu\,\alpha^{1+3\,n} - 6\,k_1\,n^3 - 11\,k_1\,n^2$$

$$-6\,k_1\,n - \alpha - k_1 - 6\,\alpha\,n - 11\,\alpha\,n^2 - 6\,\alpha\,n^3 + 6\,w\,(\alpha)\left(\frac{d}{d\alpha}w\,(\alpha)\right)\mu^3n\sigma + w\,(\alpha)\left(\frac{d}{d\alpha}w\,(\alpha)\right)\mu\,v^2\sigma$$

$$+6\,w\,(\alpha)\left(\frac{d}{d\alpha}w\,(\alpha)\right)\mu^3n^3\sigma + 11\,w\,(\alpha)\left(\frac{d}{d\alpha}w\,(\alpha)\right)\mu^3n^2\sigma = 0, \tag{28}$$

under the similarity variables $w\,(\alpha) = \frac{d}{dx}U\,(\zeta)$ and $\alpha = U\,(\zeta)$. Using Lie symmetry, we get a single reduction as symmetry reduces second order ODE (25) to first order ODE (28), solving with respect to α get us to the invariant solution given by

$$w\,(\alpha) = -\frac{\sqrt{A}}{\sigma\,\mu\,(3\,n+2)\,(1+2\,n)\,(1+3\,n)\,(n+2)\,(1+n)\,(\mu^2+v^2)}, \tag{29}$$

where

$$A = -648(1+n)(\tfrac{1}{3}+n)(\tfrac{1}{9}(1+n)\mu(\tfrac{1}{2}+n)c(n+2)\alpha^{3n+2}$$

$$+(\tfrac{1}{3}+n)(\tfrac{1}{4}b\mu(n+2)\alpha^{2n+2} + (\tfrac{1}{2}+n)(a\mu\alpha^{n+2} - 1/2(n+2)(1+n)(c_1\mu^3\sigma +$$

$$c_1\mu v^2\sigma + \alpha^2 + 2k_1\alpha)))(n+\tfrac{2}{3}))(\mu^2+v^2)\mu(\tfrac{1}{2}+n)\sigma(n+2/3)(n+2).$$

The invariant solution can be written as
$$U(\zeta) = w(\alpha)\zeta + c_1.$$

The invariant solution in integral representation is given by

$$\zeta + \int^{U(\zeta)}\frac{\sigma\,\mu\,(3\,n+2)\,(1+2\,n)\,(1+3\,n)\,(n+2)\,(1+n)\,(\mu^2+v^2)}{\sqrt{A}}d\Omega + c_1 = 0, \tag{30}$$

where

$$A = -648(1+n)(\mu^2+v^2)(\tfrac{1}{2}+n)(\tfrac{1}{3}+n)\sigma(n+\tfrac{2}{3})\mu(n+2)(\tfrac{1}{9}(1$$

$$+n)(\tfrac{1}{2}+n)c\mu(n+2)\Omega^{3n+2} + (\tfrac{1}{3}+n)(n+\tfrac{2}{3})(\tfrac{1}{4}b\mu(n+2)\Omega^{2n+2} +$$

$$(\tfrac{1}{2}+n)(a\mu\Omega^{n+2} - \tfrac{1}{2}(1+n)(c_1\mu^3\sigma + c_1\mu v^2\sigma + (\Omega)(\Omega + 2k_1))(n+2)))).$$

In the similar way, solution ODE (25) in integral representation corresponding to the values of $n = 1$, $n = 2$ and $n = 3$ are presented, respectively

$$\int^{U(\zeta)}\frac{\sqrt{30}\mu\,\sigma\,(\mu^2+v^2)}{\sqrt{-10\left(-3\,c_1\,\mu^3\sigma + \left(3/10\Omega^5c + \tfrac{1}{2}\Omega^4b + \Omega^3a - 3\,v^2c_1\,\sigma\right)\mu - 3\,(\Omega)\,(\Omega + 2\,k_1)\right)\sigma\,(\mu^2+v^2)\,\mu}}d\Omega - \zeta - c_2 = 0,$$

$$\int^{U(\zeta)}\frac{2\sqrt{105}\mu\,\sigma\,(\mu^2+v^2)}{\sqrt{-70\,\sigma\,(\mu^2+v^2)\,\mu\left(-6\,c_1\,\mu^3\sigma + (3/14\Omega^8c + 2/5\Omega^6b + \Omega^4a - 6\,v^2c_1\,\sigma)\mu - 6\,(\Omega)\,(\Omega + 2\,k_1)\right)}}d\Omega - \zeta - c_2 = 0,$$

$$\int^{U(\zeta)}\frac{2\sqrt{385}\mu\,\sigma\,(\mu^2+v^2)}{\sqrt{-154\,\sigma\,(\mu^2+v^2)\left(-10\,c_1\,\mu^3\sigma + \left(2/11\,c\Omega^{11} + \frac{5\,b\Omega^8}{14} + a\Omega^5 - 10\,v^2c_1\,\sigma\right)\mu - 10\,(\Omega)\,(\Omega + 2\,k_1)\right)\mu}}d\Omega - \zeta - c_2 = 0.$$

The ODE (25) is cumbersome and its solution is presented above in integral form as the general value of n and k_1. Suppose a solution of the form given by
$$U(\zeta) = G(\zeta)e^{\lambda\zeta}.$$

Where $G(\zeta)$ is to be determined, and λ is a constant. This assumption reduces the ODE (25) to a manageable equation

$$-6(-\mu\sigma(\mu^2+v^2)(1+n)e^{\lambda\zeta}\lambda^2 + e^{\lambda\zeta}(1+n))(\tfrac{1}{3}+n)(\tfrac{1}{2}+n)G(\zeta)$$

$$+3\mu(1+n)b(\tfrac{1}{3}+n)(G(\zeta)e^{\lambda\zeta})^{1+2n} - 6(-\tfrac{1}{3}c\mu(1+n)(G(\zeta)e^{\lambda\zeta})^{1+3n}$$

$$+(-\mu\sigma(\mu^2+v^2)(1+n)(2(\tfrac{d}{d\zeta}G(\zeta))\lambda e^{\lambda\zeta} + (\tfrac{d^2}{d\zeta^2}G(\zeta))e^{\lambda\zeta})$$

$$-(G(\zeta)e^{\lambda\zeta})^{1+n}a\mu)(\tfrac{1}{3}+n))(\tfrac{1}{2}+n) = k_1(6n^3 + 11n^2 + 6n + 1). \tag{31}$$

By factoring out $e^{\lambda\zeta}$ from the above equation, comparing nonlinear terms of $G(\zeta)$ and by simplifying, we get the following condition

$$6\left(\frac{1}{2}+n\right)\left(-1 + \mu\sigma\left(\mu^2 + v^2\right)\lambda^2\right)(1+n)\left(\frac{1}{3}+n\right) = 0, \tag{32}$$

that yields the values of λ given by

$$\lambda_1 = \frac{1}{\sqrt{\mu^3\sigma + \mu v^2\sigma}}, \quad \lambda_2 = -\frac{1}{\sqrt{\mu^3\sigma + \mu v^2\sigma}}. \tag{33}$$

Finally, it provide us the solutions of the form $U(\zeta) = Ge^{\lambda\zeta}$, where G is a constant, as we received $G'(\zeta) = 0$. The solutions are given by

$$U(\zeta) = c_1 e^{\frac{1}{\sqrt{\mu^3\sigma + \mu v^2\sigma}}\zeta} + c_2 e^{-\frac{1}{\sqrt{\mu^3\sigma + \mu v^2\sigma}}\zeta}. \tag{34}$$

Thus, the solution of the ZK equation (1) can be obtained in original variables by substituting the value of $\zeta = \mu x + v y - t$ and $u(t, x, y) = U(\zeta)$ presented by

$$u(t, x, y) = c_1 e^{\frac{1}{\sqrt{\mu^3\sigma + \mu v^2\sigma}}(\mu x + v y - t)} + c_2 e^{-\frac{1}{\sqrt{\mu^3\sigma + \mu v^2\sigma}}(\mu x + v y - t)}. \tag{35}$$

This solution represent travelling wave solution and its behaviour over time for different values of parameters is presented in Figure-1.
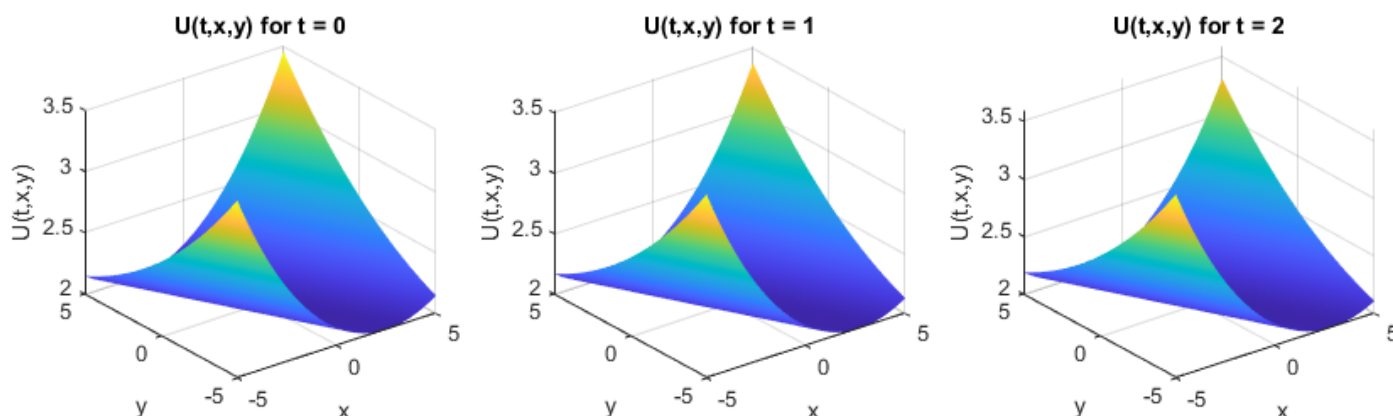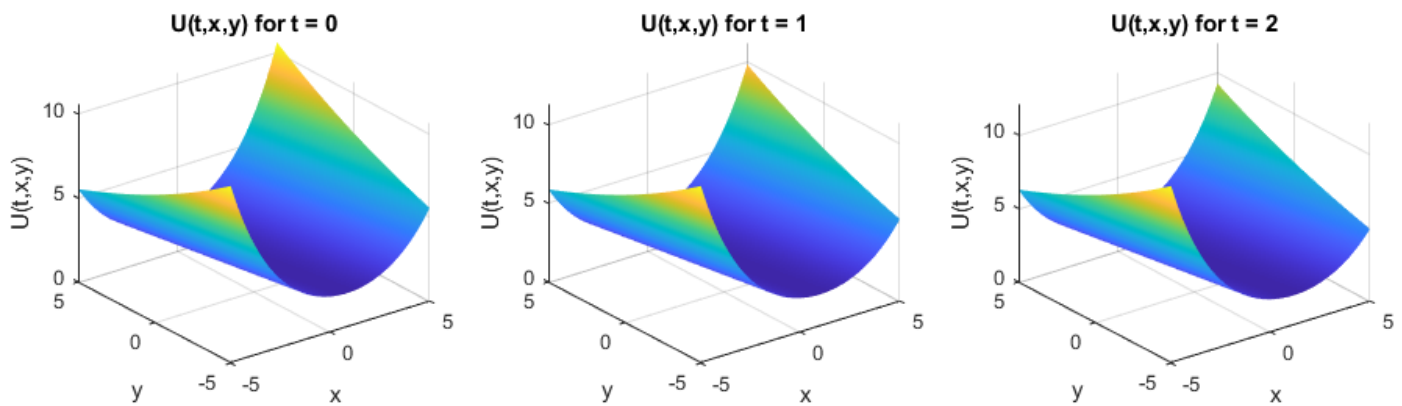

Figure 1. Travelling wave $u(t, x, y)$ over time

For another set of parameters, the solution $u(t, x, y)$ is presented in Figure-2, which is depicting the wave behaviour over time t.

3.2. Analysis of ODE (27) and Travelling Wave Solution

An analysis of (27) is presented in this section. ODE (27) can further reduce using invariance analysis. The ODE (27) reduces to first order ODE by single reduction using the symmetry $X_1 = \partial\zeta$. The reduced ODE is given by

$$-6k_2n^3 - 22k_2n^2 - 24k_2n - 8k_2 + 4c\mu\alpha^{2+3n} + 6w(\alpha)(\tfrac{d}{d\alpha}w(\alpha))\alpha\mu^3n^3\sigma$$
$$+22w(\alpha)(\tfrac{d}{d\alpha}w(\alpha))\alpha\mu^3n^2\sigma + 24w(\alpha)(\tfrac{d}{d\alpha}w(\alpha))\alpha\mu^3n\sigma + 8w(\alpha)(\tfrac{d}{d\alpha}w(\alpha))\alpha\mu v^2\sigma$$
$$-11\alpha^2n^2 - 3\alpha^2n^3 - 12\alpha^2n + 6w(\alpha)(\tfrac{d}{d\alpha}w(\alpha))\alpha\mu n^3 v^2\sigma + 22w(\alpha)(\tfrac{d}{d\alpha}w(\alpha))\alpha\mu n^2 v^2\sigma$$
$$+24w(\alpha)(\tfrac{d}{d\alpha}w(\alpha))\alpha\mu n v^2\sigma + 8w(\alpha)(\tfrac{d}{d\alpha}w(\alpha))\alpha\mu^3\sigma - 3(w(\alpha))^2\mu n^3 v^2\sigma - 11(w(\alpha))^2\mu n^2 v^2\sigma$$
$$-12(w(\alpha))^2\mu n v^2\sigma + 3\mu b\alpha^{2+2n}n^2 + 2c\mu\alpha^{2+3n}n^2 + 6n^2\alpha^{2+n}a\mu + 8\mu b\alpha^{2+2n}n + 6c\mu\alpha^{2+3n}n$$
$$+10n\alpha^{2+n}a\mu - 11(w(\alpha))^2\mu^3n^2\sigma - 12(w(\alpha))^2\mu^3n\sigma - 4(w(\alpha))^2\mu v^2\sigma - 3(w(\alpha))^2\mu^3n^3\sigma - 4\alpha^2$$

Figure 2. Travelling wave $u(t, x, y)$ over time

$$+4\mu b a^{2+2n} - 4(w(\alpha))^2 \mu^3 \sigma + 4\alpha^{2+n} a\mu = 0, \tag{36}$$

under the similarity variables $w(\alpha) = \frac{d}{d\zeta} U(\zeta)$ and $\alpha = U(\zeta)$. Using Lie symmetry, we get a single reduction as symmetry reduces second order ODE (27) to first order ODE (36) in $w(\alpha)$. Solving (36) yield us the invariant solution given by

$$w(\alpha) = 1/18 \frac{\sqrt{-648\alpha AC(\frac{1}{9}Cc\mu B(D)\alpha^{3+3n} + A(\frac{1}{4}b\mu(D)\alpha^{2n+3} + (\Psi)B)E)(\mu^2 + v^2)E\mu\sigma B(D)}}{\sigma\mu\alpha(\mu^2 + v^2)ABE(D)C},$$

where,

$$\frac{2}{3} + n = A, 2 + 3n = 3A, n + \frac{1}{2} = B, 2n + 1 = 2B,$$

$$1 + n = C, 1 + n = C, 2 + n = D, n + \frac{1}{3} = E, 3n + 1 = 3E,$$

$$\alpha^{n+3}a\mu - \frac{1}{2}\alpha(2 + n)(1 + n)\left(\alpha\mu^3\sigma c_1 + \alpha\mu v^2\sigma c_1 + \alpha^2 - 2k_2\right) = \Psi.$$

Using similarity variable, the invariant solution can be written as

$$U(\zeta) = w(\alpha)\zeta + c_1.$$

The invariant solution $U(\zeta)$ is given by

$$\zeta - \int^{U(\zeta)} 18 \frac{\sigma\mu\Omega ABE(D)C(\mu^2 + v^2)}{\sqrt{-648(\frac{1}{9}C\mu cB(D)\Omega^{3A} + (\frac{1}{4}b\mu(D)\Omega^{2+2n} + (\Psi)B)AE)C\mu B(\mu^2 + v^2)\Omega^2 A\sigma E(D)}} d\Omega + c_2 = 0,$$

where

$$\frac{2}{3} + n = A, 2 + 3n = 3A, n + \frac{1}{2} = B, 2n + 1 = 2B,$$

$$1 + n = C, 1 + n = C, 2 + n = D, n + \frac{1}{3} = E, 3n + 1 = 3E,$$

$$a^{2+n}a\mu - \frac{1}{2}(2 + n)(1 + n)\left(a\mu^3\sigma c_1 + a\mu v^2\sigma c_1 + a^2 - 2k_2\right) = \Psi.$$

The ODE (27) is complex and its solution even for $n = 1$ and for particular value of $k_2 = 0$ is challenging to find as presented

$$\int^{U(\zeta)} \frac{\sqrt{30}(\mu^2 + v^2)\sigma\mu}{\sqrt{(\mu^2 + v^2)\sigma\mu(-3c\Omega^4\mu + 30c_1\mu^3\sigma + 30c_1\mu v^2\sigma - 5b\Omega^3\mu - 10\Omega^2 a\mu + 30\Omega)\Omega}} d\Omega - \zeta - c_2 = 0.$$

For ODE (27), we will find the solution of the form given by

$$U(\zeta) = G(\zeta)e^{\lambda\zeta},$$

where $G(\zeta)$ is to be determined, and λ is a constant. This assumption reduces the ODE (27) to a manageable one.

$$3\mu(n + \tfrac{2}{3})(2 + n)b(G(\zeta)e^{\lambda\zeta})^{2+2n} + 6(\tfrac{1}{3}c\mu(2 + n)(G(\zeta)e^{\lambda\zeta})^{2+3n} + (a\mu(G(\zeta)e^{\lambda\zeta})^{2+n}$$

$$+\tfrac{1}{2}(e^{\lambda\zeta})^2(2G(\zeta)\mu\sigma(\mu^2 + \nu^2)\tfrac{d^2}{d\zeta^2}G(\zeta) - \mu\sigma(\mu^2 + \nu^2)(\tfrac{d}{d\zeta}G(\zeta))^2 + 2G(\zeta)\mu\sigma\lambda(\mu^2 + \nu^2)\tfrac{d}{d\zeta}G(\zeta)$$

$$+(G(\zeta))^2(\lambda^2\mu^3\sigma + \lambda^2\mu\nu^2\sigma - 1))(2 + n))(n + \tfrac{2}{3}))(1 + n) = k_2(6n^3 + 22n^2 + 24n + 8) \tag{37}$$

By factoring out $e^{\lambda\zeta}$ from the above equation, comparing nonlinear terms of $G(\zeta)$ and by simplifying, we get the following condition

$$3\,(1 + n)\,(n + 2/3)\,(2 + n)\left(-1 + \mu\,\sigma\,\left(\mu^2 + \nu^2\right)\lambda^2\right) = 0, \tag{38}$$

that yields the values of λ given by

$$\lambda_1 = \frac{1}{\sqrt{\mu^3\sigma + \mu\nu^2\sigma}}, \quad \lambda_2 = -\frac{1}{\sqrt{\mu^3\sigma + \mu\nu^2\sigma}}. \tag{39}$$
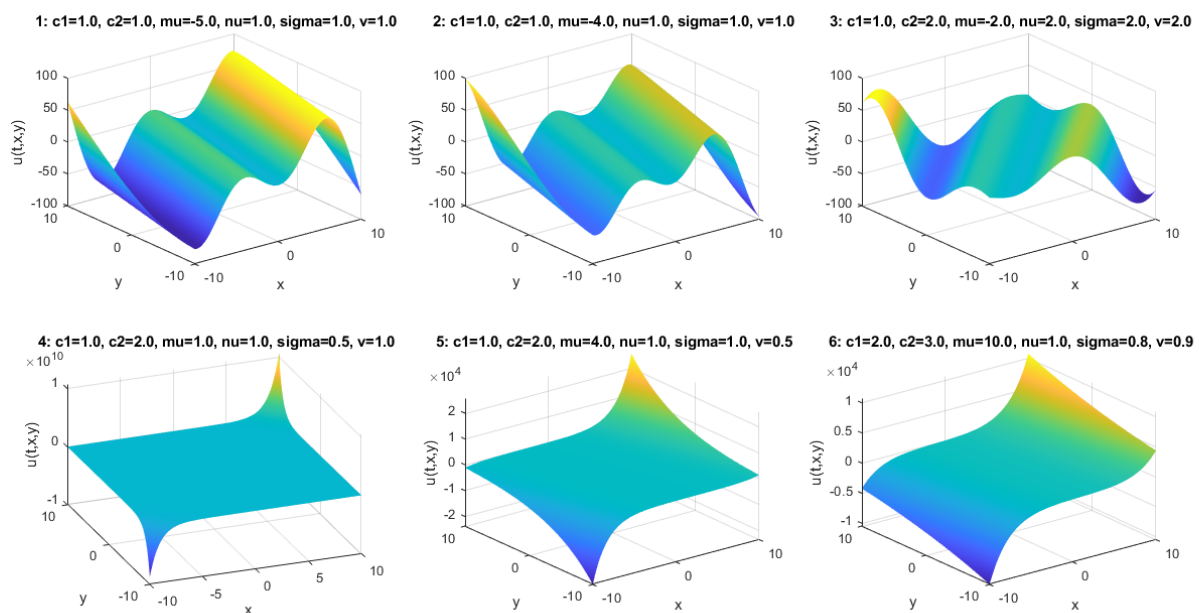
Finally, it provide us the solutions of the form $U(\zeta) = Ge^{\lambda\zeta}$, where $G(\zeta) = c_1\zeta + c_2$ is a constant, as we received $G''(\zeta) = 0$. The solutions are given by

$$U(\zeta) = (c_1\zeta + c_2)e^{\frac{1}{\sqrt{\mu^3\sigma+\mu\nu^2\sigma}}\zeta} + (c_1\zeta + c_2)e^{-\frac{1}{\sqrt{\mu^3\sigma+\mu\nu^2\sigma}}\zeta} \tag{40}$$

Thus, the solution of the ZK equation (1) can be obtained in original variables by substituting the value of $\zeta = \mu x + \nu y - t$ and $u(t, x, y) = U(\zeta)$ presented by

$$u(t, x, y) = [c_1(\mu x + \nu y - t) + c_2]e^{\frac{1}{\sqrt{\mu^3\sigma+\mu\nu^2\sigma}}(\mu x+\nu y-t)} + [c_1(\mu x + \nu y - t) + c_2]e^{-\frac{1}{\sqrt{\mu^3\sigma+\mu\nu^2\sigma}}(\mu x+\nu y-t)}$$

The solution is presented in Figure-3.

Figure 3. Travelling wave $u(t, x, y)$ over time

This solution represent travelling wave solution and its behaviour over time for different values of parameters.

4. A COMPARISON BETWEEN SYMMETRY REDUCTION AND MULTI-REDUCTION VIA MULTIPLIERS

In this section, we study the symmetry classification and possible reductions of ZK equation (1) based on the parameters involved in function $G(u) = au^n + bu^{2n} + cu^{3n}$ containing triple power non-linearities. The ZK equation (1) has three translation symmetries given by

$$X_1 = D_t, \quad X_2 = D_x, \text{ and } X_3 = D_y, \tag{41}$$

which has corresponding single reduction from $(1 + 2)$ ZK equation (1) to $(1 + 1)$ second order PDE in (α, β)-space given by respectively

$$
\begin{aligned}
(\tfrac{\partial}{\partial\alpha}F(\alpha,\beta))a(F(\alpha,\beta))^n + (\tfrac{\partial}{\partial\alpha}F(\alpha,\beta))b(F(\alpha,\beta))^{2n} + (\tfrac{\partial}{\partial\alpha}F(\alpha,\beta))c(F(\alpha,\beta))^{3n} \\
+ \tfrac{\partial^3}{\partial\alpha^3}F(\alpha,\beta) + \tfrac{\partial^3}{\partial\beta^2\partial\alpha}F(\alpha,\beta) = 0,
\end{aligned}
\tag{42}
$$

with similarity variables $[\{U(x,y,t) = F(x,y)\}, \{\alpha = x, \beta = y\}]$.

,

$$
\tfrac{\partial}{\partial\alpha}F(\beta,\alpha) = 0,
\tag{43}
$$

with similarity variables $[\{U(x,y,t) = F(y,t)\}, \{\alpha = t, \beta = y\}]$.

and

$$
\begin{aligned}
\tfrac{\partial}{\partial\alpha}F(\beta,\alpha) + (\tfrac{\partial}{\partial\beta}F(\beta,\alpha))a(F(\beta,\alpha))^n + (\tfrac{\partial}{\partial\beta}F(\beta,\alpha))b(F(\beta,\alpha))^{2n} \\
+ (\tfrac{\partial}{\partial\beta}F(\beta,\alpha))c(F(\beta,\alpha))^{3n} + \tfrac{\partial^3}{\partial\beta^3}F(\beta,\alpha)\} = 0
\end{aligned}
\tag{44}
$$

with similarity variables $[\{U(x,y,t) = F(x,t)\}, \{\alpha = t, \beta = x\}]$.

Lie symmetries provide only single reduction upto a independent variable and we received $(1 + 1)$ reduced PDE from $(1 + 2)$ PDE. In order to get invariant solutions, it require further analysis to study the problem, which is even challenging to solve one dimensional PDE. Even reduction under symmetry generators

$$
X^1 = X_1 + X_2, \quad X^2 = X_1 + X_3, \text{ and } X^3 = X_1 + X_2 + X_3
\tag{45}
$$

provide us the single reduction to $(1 + 1)$ PDE in (α, β)-space given by respectively

$$
\begin{aligned}
\tfrac{\partial}{\partial\beta}F(\alpha,\beta) - (\tfrac{\partial}{\partial\beta}F(\alpha,\beta))a(F(\alpha,\beta))^n - (\tfrac{\partial}{\partial\beta}F(\alpha,\beta))b(F(\alpha,\beta))^{2n} \\
- (\tfrac{\partial}{\partial\beta}F(\alpha,\beta))c(F(\alpha,\beta))^{3n} - \tfrac{\partial^3}{\partial\beta^3}F(\alpha,\beta) - \tfrac{\partial^3}{\partial\beta\partial\alpha^2}F(\alpha,\beta) = 0
\end{aligned}
\tag{46}
$$

with similarity variables $[\{U(x,y,t) = F(y, -x + t)\}, \{\alpha = y, \beta = -x + t\}]$.

,

$$
\begin{aligned}
\tfrac{\partial}{\partial\beta}F(\alpha,\beta) + (\tfrac{\partial}{\partial\alpha}F(\alpha,\beta))a(F(\alpha,\beta))^n + (\tfrac{\partial}{\partial\alpha}F(\alpha,\beta))b(F(\alpha,\beta))^{2n} \\
+ (\tfrac{\partial}{\partial\alpha}F(\alpha,\beta))c(F(\alpha,\beta))^{3n} + \tfrac{\partial^3}{\partial\alpha^3}F(\alpha,\beta) + \tfrac{\partial^3}{\partial\beta^2\partial\alpha}F(\alpha,\beta) = 0
\end{aligned}
\tag{47}
$$

with similarity variables $[\{U(x,y,t) = F(x, -y + t)\}, \{\alpha = x, \beta = -y + t\}]$.

and

$$
\begin{aligned}
\tfrac{\partial}{\partial\alpha}F(\beta,\alpha) - (\tfrac{\partial}{\partial\beta}F(\beta,\alpha))a(F(\beta,\alpha))^n - a(F(\beta,\alpha))^n\tfrac{\partial}{\partial\alpha}F(\beta,\alpha) - (\tfrac{\partial}{\partial\beta}F(\beta,\alpha))b(F(\beta,\alpha))^{2n} \\
- b(F(\beta,\alpha))^{2n}\tfrac{\partial}{\partial\alpha}F(\beta,\alpha) - (\tfrac{\partial}{\partial\beta}F(\beta,\alpha))c(F(\beta,\alpha))^{3n} - c(F(\beta,\alpha))^{3n}\tfrac{\partial}{\partial\alpha}F(\beta,\alpha) - 2\tfrac{\partial^3}{\partial\beta^3}F(\beta,\alpha) \\
- 4\tfrac{\partial^3}{\partial\beta^2\partial\alpha}F(\beta,\alpha) - 3\tfrac{\partial^3}{\partial\beta\partial\alpha^2}F(\beta,\alpha) - \tfrac{\partial^3}{\partial\alpha^3}F(\beta,\alpha) = 0
\end{aligned}
\tag{48}
$$

with similarity variables $[\{U(x,y,t) = F(-x + y, -x + t)\}, \{\alpha = -x + t, \beta = -x + y\}]$.

So, multi-reduction using conservation laws analysis is better approach to study higher order and higher dimensional model.

5. MULTI-SOLITON SOLUTIONS VIA INVARIANCE TRANSFORMATION

The early history of solitons is presented in [23] and the forms of solitons we presented in this study is discussed in [24, 25]. In this section we shall discuss soliton and multi-soliton solutions for ZK equation (1). The solutions can be expressed as $u(t,x,y) \rightarrow f(\alpha x + \beta y - vt)$, where the solitons propagates along the x and y directions with velocity v. As we discussed earlier the line travelling wave reductions for ZK equation (1) with a 2-dimensional symmetry algebra in (2+1)-dimensions such as line solitons via invariance under two commuting translations given by

$$
X_1 = \left(\alpha^2 + \beta^2\right)\partial_t + \alpha u\partial_x + \beta\partial_y, \quad X_2 = \beta\partial_x - \alpha\partial_y.
\tag{49}
$$

Reduction under above type of commuting translation symmetries is very common in application and yield interesting types of solutions called line travelling wave solutions or line soliton solutions, under similarity invariant transformations

$\zeta = \alpha x + \beta y - \gamma t$ and $u(t, x, y) = f(\zeta)$, where γ is the spped of. The physics of the line travelling wave is presented in [15] and yield the solutions correspond to the reduction

$$u(t, x, y) \rightarrow f(\alpha x + \beta y - \gamma t) \tag{50}$$

and satisfy the reduced ODE. Under the transformation

$$u(x, t, y) = f(\zeta), \; \zeta = \alpha x + \beta y - \gamma t$$

the ZK equation (1) reduces to ODE given by

$$\gamma \frac{d}{d\zeta} f(\zeta) + (a(f(\zeta))^n + b(f(\zeta))^{2n} + c(f(\zeta))^{3n}) \alpha \frac{d}{d\zeta} f(\zeta)$$
$$+ \sigma (\alpha^3 \frac{d^3}{d\zeta^3} f(\zeta) + \alpha \beta^2 \frac{d^3}{d\zeta^3} f(\zeta)) = 0 \tag{51}$$

It can be further simplified to

$$\alpha \sigma \left(\alpha^2 + \beta^2 \right) \left(\frac{d^2}{d\zeta^2} f(\zeta) \right) + \frac{a\alpha f(\zeta)^{n+1}}{n+1} + \frac{b\alpha f(\zeta)^{2n+1}}{2n+1} + \frac{c\alpha f(\zeta)^{3n+1}}{3n+1} + \gamma f(\zeta) = 0$$

To determine the soliton, we look for a solution that decays to zero as $\zeta \rightarrow \pm\infty$. For the construction of solitons, one way to find solitary wave profile is to consider *sech* function

$$f(\zeta) = A \operatorname{sech}^2(B\zeta)$$

where A, and B are constants to be determined in terms of wave velocity v, the coefficients a, b, c of the non-linearities u^n, u^{2n}, u^{3n} and dispersion's coefficient σ. The ODE under the solitary wave profile takes the form

$$6\sigma(\alpha^2 + \beta^2) A \operatorname{sech}(B\zeta)^2 (\tanh(B\zeta)^2 - \tfrac{1}{3}) B^2 \alpha + \frac{a\alpha(A\operatorname{sech}(B\zeta)^2)^{n+1}}{n+1}$$
$$+ \frac{b\alpha(A\operatorname{sech}(B\zeta)^2)^{2n+1}}{2n+1} + \frac{c\alpha(A\operatorname{sech}(B\zeta)^2)^{3n+1}}{3n+1} + \gamma A \operatorname{sech}(B\zeta)^2 = 0 \tag{52}$$

For the soliton solutions to hold, we match the coefficients of the non-linear terms and receive the following conditions

$$-2\sigma \left(\alpha^2 + \beta^2 \right) B^2 \alpha + \gamma = 0,$$
$$6\sigma \left(\alpha^2 + \beta^2 \right) A + \tfrac{1}{2} \frac{\gamma}{\sigma(\alpha^2+\beta^2)} = 0.$$

that yield us the values of B and A respectively, in terms of parameters α, β, γ and σ given by

$$B = \pm \tfrac{1}{2} \frac{\gamma\sqrt{2}}{\sqrt{\alpha\sigma(\alpha^2+\beta^2)\gamma}},$$
$$A = -\tfrac{1}{12} \frac{\gamma}{\sigma^2(\alpha^2+\beta^2)^2}.$$

By substituting values of A and B back in soliton profile provides us the soliton solution of the form

$$u(t, x, y) = \left[-\frac{1}{12} \frac{\gamma}{\sigma^2 \left(\alpha^2 + \beta^2 \right)^2} \right] \operatorname{sech}^2 \left(\frac{1}{2} \frac{\gamma\sqrt{2}}{\sqrt{\alpha\sigma \left(\alpha^2 + \beta^2 \right) \gamma}} (\alpha x + \beta y - \gamma t) \right)$$

The 3D plot of the soliton solution is presented in Figure-4.

Now, we can discuss the superposition of two solitons for the construction of multi-solitons structure of the form
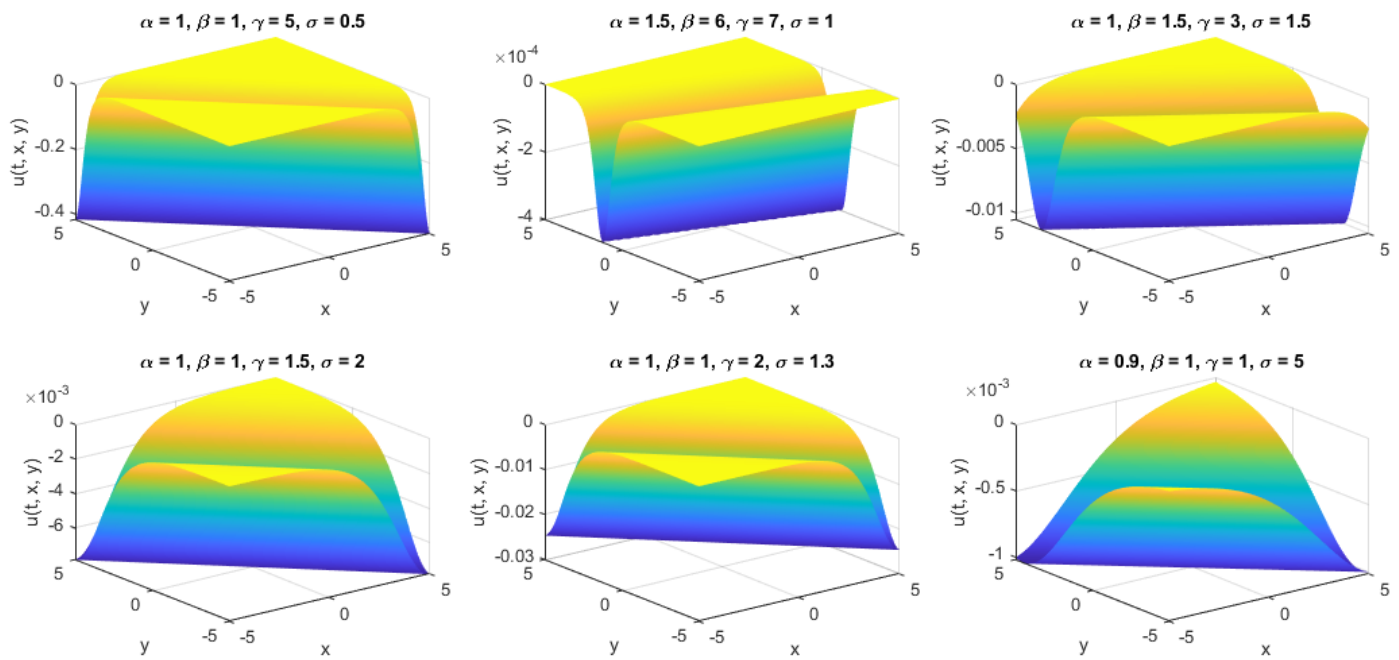
$$u(t, x, y) = f_1 \left(\alpha_1 x + \beta_1 y - \gamma_1 t \right) + f_2 \left(\alpha_2 x + \beta_2 y - \gamma_2 t \right)$$

where the solitary wave profile for two-soliton solutions is

$$f_1 \left(\zeta_1 \right) = A_1 \operatorname{sech}^2 \left(B_1 \zeta_1 \right),$$
$$f_2 \left(\zeta_2 \right) = A_2 \operatorname{sech}^2 \left(B_2 \zeta_2 \right).$$

and

$$\zeta_1 = \alpha_1 x + \beta_1 y - \gamma_1 t,$$

Figure 4. Soliton $u(t, x, y)$ with different parameters

$$\zeta_2 = \alpha_2 x + \beta_2 y - \gamma_2 t.$$

Each soliton can be determined by its own velocity, amplitude, and width based on the parameters $A_1, B_1, \alpha_1, \beta_1, \gamma_1$ for the first soliton and $A_2, B_2, \alpha_2, \beta_2, \gamma_2$ for the second soliton. By following the same ansatz, the two-soliton solutions can be presented by

$$u(t, x, y) = A_1 \operatorname{sech}^2 (B_1 (\alpha_1 x + \beta_1 y - \gamma_1 t)) + A_2 \operatorname{sech}^2 (B_2 (\alpha_2 x + \beta_2 y - \gamma_2 t))$$

$$B_1 = B_2 = \frac{1}{2} \frac{\gamma \sqrt{2}}{\sqrt{\alpha \sigma (\alpha^2 + \beta^2) \gamma}}, \quad A_1 = A_2 = -\frac{1}{12} \frac{\gamma}{\sigma^2 (\alpha^2 + \beta^2)^2}.$$

The two-soliton takes the form

$$u(t, x, y) = \sum_{i=1}^{2} [-\frac{1}{12} \frac{\gamma_i}{\sigma^2 (\alpha_i^2 + \beta_i^2)^2}] \operatorname{sech}^2 \left(\frac{1}{2} \frac{\gamma_i \sqrt{2}}{\sqrt{\alpha_i \sigma (\alpha_i^2 + \beta_i^2) \gamma_i}} (\alpha_i x + \beta_i y - \gamma_i t) \right).$$

The 3D plot of the two-soliton solution is presented in Figure-5.

For different velocities, when $\gamma_1 \neq \gamma_2$, the elastic collision occurs and pass through each other. Finally, we can generalise the solitons into multi-solitons by superposing more solitons and can be represented by

$$u(t, x, y) = \sum_{i=1}^{n} [-\frac{1}{12} \frac{\gamma_i}{\sigma^2 (\alpha_i^2 + \beta_i^2)^2}] \operatorname{sech}^2 \left(\frac{1}{2} \frac{\gamma_i \sqrt{2}}{\sqrt{\alpha_i \sigma (\alpha_i^2 + \beta_i^2) \gamma_i}} (\alpha_i x + \beta_i y - \gamma_i t) \right).$$
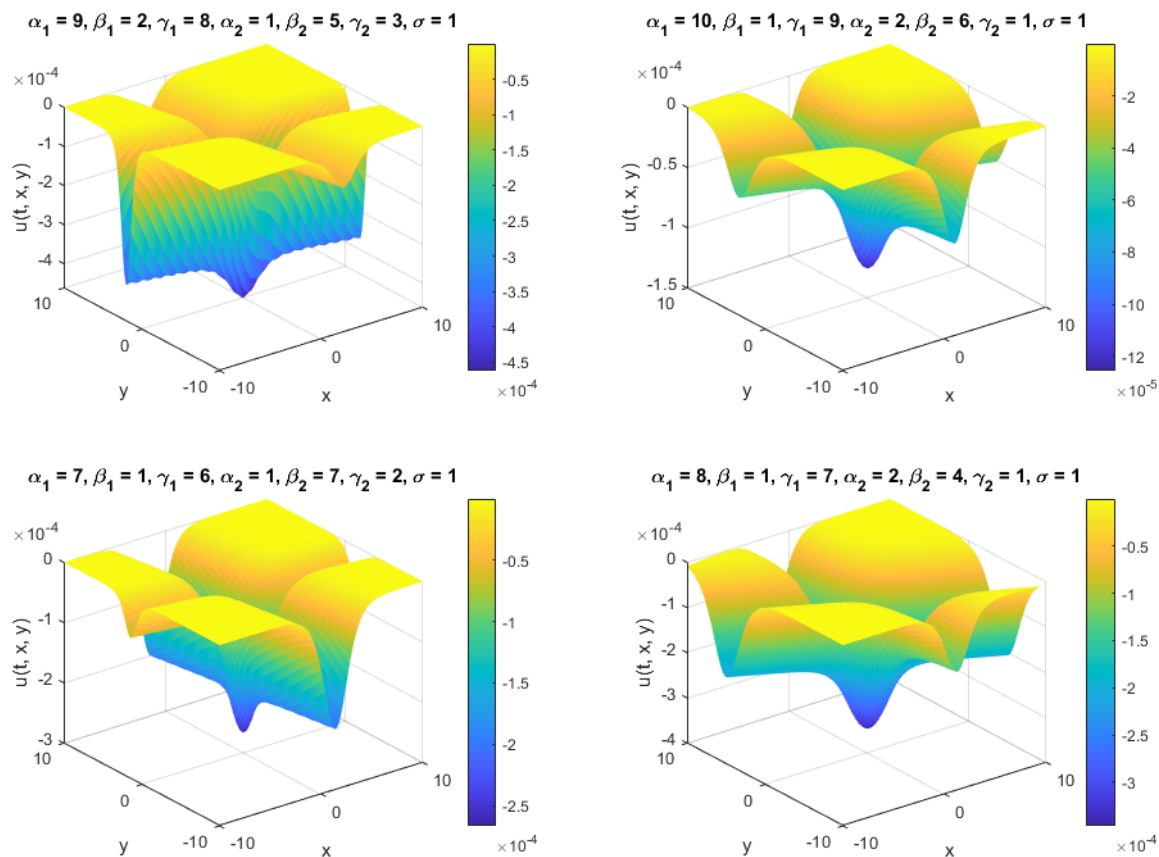
6. VORTEX SOLITON SOLUTIONS

We study the vortex type [26, 27] of solitons for ZK equation (1) in both spatial dimensions x and y that exhibit a vortex structure like a rotating wave. We seek the vortex solitons by using the transformation

$$u(t, x, y) \rightarrow u(r, \theta, t),$$

where,

$$x = r \cos \theta, \quad y = r \sin \theta, \quad r = \sqrt{x^2 + y^2},$$

Figure 5. Soliton $u(t, x, y)$ with different parameters

r represents the radial distance and θ is the vortex angle. The Laplacian in polar coordinates provide us the Zakharov-Kuznetsov equation in polar coordinates given by

$$u_t + \left(au^n + bu^{2n} + cu^{3n}\right)\frac{\partial u}{\partial r} + \sigma\left(\frac{\partial^2 u}{\partial r^2} + \frac{1}{r^2}\frac{\partial^2 u}{\partial \theta^2}\right)_r = 0 \tag{53}$$

Ansatz for vortex solitons can be applied to find solutions with a nontrivial phase of the form

$$u(r, \theta, t) = U(r)e^{i\zeta}, \quad \zeta = m\theta - \omega t$$

Under the above transformation the ZK equation in ploar coordinates (53) reduces to ODE given by

$$-U(r)\omega + (aU(r)^n + bU(r)^{2n} + cU(r)^{3n})(\frac{\mathrm{d}}{\mathrm{d}r}U(r)) + \sigma(\frac{\mathrm{d}^3}{\mathrm{d}r^3}U(r) - \frac{m^2}{r^2}\frac{\mathrm{d}}{\mathrm{d}r}U(r)) = 0 \tag{54}$$

Above ODE represents the radial profile of vortex solitons. The soliton must decay to zero as $r \to \infty$, which ensures the localization of the solution. To find vortex solitons, we consider $sech$ function

$$U(r) = Ar^m \operatorname{sech}^2(Br)$$

where A, and B are constants to be determined in terms of the coefficients a, b, c of the non-linearities u^n, u^{2n}, u^{3n} and dispersion's coefficient σ. The ODE under the solitary wave profile takes the form

$$-Ar^m \operatorname{sech}(Br)^2\omega$$

$$+ \left(a\left(Ar^m \operatorname{sech}(Br)^2\right)^n + b\left(Ar^m \operatorname{sech}(Br)^2\right)^{2n} + c\left(Ar^m \operatorname{sech}(Br)^2\right)^{3n}\right)\left(\frac{\partial}{\partial r}\left(Ar^m \operatorname{sech}(Br)^2\right)\right)\omega$$

$$+\sigma\left(\frac{\partial^3}{\partial r^3}\left(Ar^m \operatorname{sech}(Br)^2\right) - \frac{m^2\left(\frac{\partial}{\partial r}\left(Ar^m \operatorname{sech}(Br)^2\right)\right)}{r^2}\right) = 0 \tag{55}$$

For the soliton solutions to hold, we match the coefficients of the non-linear terms in r and receive the following conditions

$$\frac{1}{4}B^2 m\sigma + 3\sigma m\left(m - \frac{2}{3}\right) = 0$$

$$\frac{1}{24}\omega + \frac{1}{4}B^2 m\sigma = 0$$

$$16\sigma B^3 + 18B^2 m\sigma + 16\sigma B\left(-\frac{1}{4}m^2 + \frac{3}{8}m\right) = 0$$

$$ABm^2\sigma - 5B^2\sigma - AB = 0$$

which respectively provide us the the values of B and A given by

$$B_1 = \pm 2\sqrt{-3m + 2},$$
$$B_2 = \pm\frac{1}{6}\frac{\sqrt{-6\sigma m\omega}}{\sigma m},$$
$$B_3 = -\frac{9}{16}m + \frac{1}{16}\sqrt{145m^2 - 96m}.$$

$$A_1 = -\frac{10(3m-2)\sigma}{\sqrt{-3m+2}\left(m^2\sigma - 1\right)},$$
$$A_2 = -\frac{5\omega\sigma}{\sqrt{-6m\sigma\omega}\left(m^2\sigma - 1\right)},$$
$$A_3 = \frac{5}{16}\frac{\sigma\left(-9m + \sqrt{145m^2 - 96m}\right)}{m^2\sigma - 1}.$$

Finally yields the vortex soliton solutions of the form

$$u(r,\theta,t) = Ar^m \operatorname{sech}^2(Br)\mathrm{e}^{i(m\theta - \omega t)},$$

Three vortex solutions obtained based on the values of $A1, A2, A3$ and $B1, B2, B3$.

$$u_1(r,\theta,t) = -\frac{10(3m - 2)\sigma}{\sqrt{-3m + 2}\left(m^2\sigma - 1\right)}r^m \operatorname{sech}^2(2r\sqrt{-3m + 2})\mathrm{e}^{i(m\theta - \omega t)},$$

$$u_2(r,\theta,t) = -\frac{5\omega\sigma}{\sqrt{-6m\sigma\omega}\left(m^2\sigma - 1\right)}r^m \operatorname{sech}^2(\frac{1}{6}\frac{\sqrt{-6\sigma m\omega}}{\sigma m}r)\mathrm{e}^{i(m\theta - \omega t)},$$

The plot of the vortex solutions $u_1(r,\theta,t)$ is presented in Figure-6 and $u_2(r,\theta,t)$ in Figure-7.

$$u_3(r,\theta,t) = \frac{5}{16}\frac{\sigma\left(-9m + \sqrt{145m^2 - 96m}\right)}{m^2\sigma - 1}r^m \operatorname{sech}^2((-\frac{9}{16}m + \frac{1}{16}\sqrt{145m^2 - 96m})r)\mathrm{e}^{i(m\theta - \omega t)}.$$

Plot of solution $u_3(r,\theta,t)$ is presented in Figure-8 for different values of m.

For plotting solutions $u_1(r,\theta,t)$ and $u_2(r,\theta,t)$ we considered these values for amplitude $m = 6$, for scaling of the secant hyperbolic $\sigma = 1$, and $\omega = 1$, which determine the angular frequency of the oscillation. The contour plot for vortex solution $u_3(r,\theta,t)$ is presented in Figure-9.

In this study, we presented vortex solution $u_1(r,\theta,t), u_2(r,\theta,t)$, and $u_3(r,\theta,t)$ of ZK equation (1) in polar coordinates includes a radial exponent r^m and a secant hyperbolic function $\operatorname{sech}(r)$ and a exponential term $\mathrm{e}^{i(m\theta - \omega t)}$, where m, σ, and ω are key parameters. For vortex solution $u_3(r,\theta,t)$ we presented four different graphs based on the values of amplitude m. The parameters involved affect the overall appearance and magnitude of the solutions. We can clearly see how parameters like radial exponent and secant profile affect the vortex solitons's decay and oscillation patterns over space.

7. DISCUSSION OF RESULTS IN PLASMA PHYSICS

The plasma waves generated in the model discussed here are stable. This is particularly the case related to travelling wave solutions. The vortex solutions are in line with a bell-shaped solitary wave solution which suggests that electric field potential, electric field and magnetic field are stable. Some of the figures indicate a nonlinear ion-acoustic solitary wave like behaviour of the wave. In all of the cases, the spread of the waves is stable with little or no chaotic type structure following the initial waves. The amplitudes of the waves, indicated by the magnitudes of the complex cases in some of the cases, display wave behaviours that are stable.
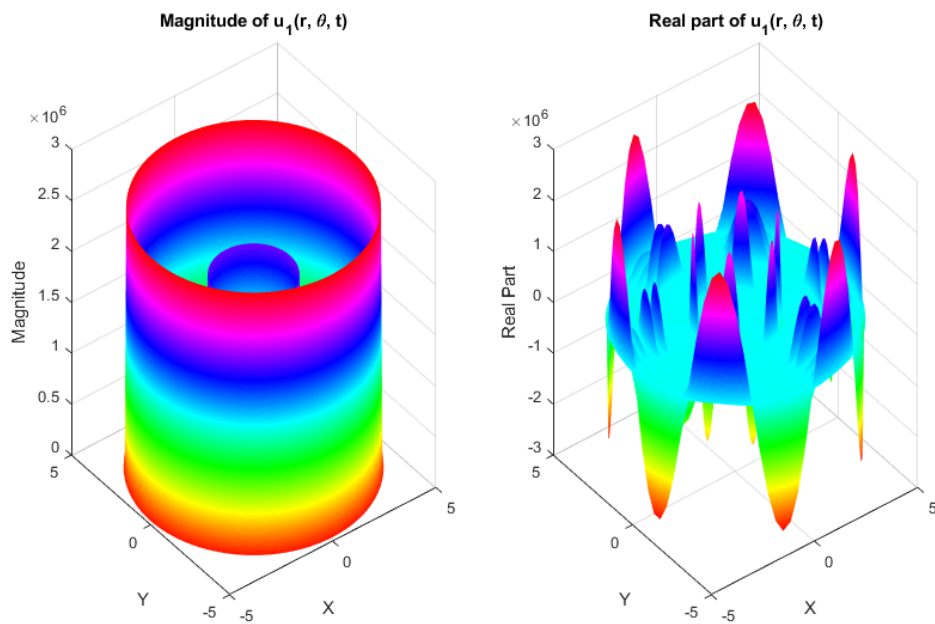
Figure 6. 3D plot of the real part and magnitude of $u_1(r, \theta, t)$
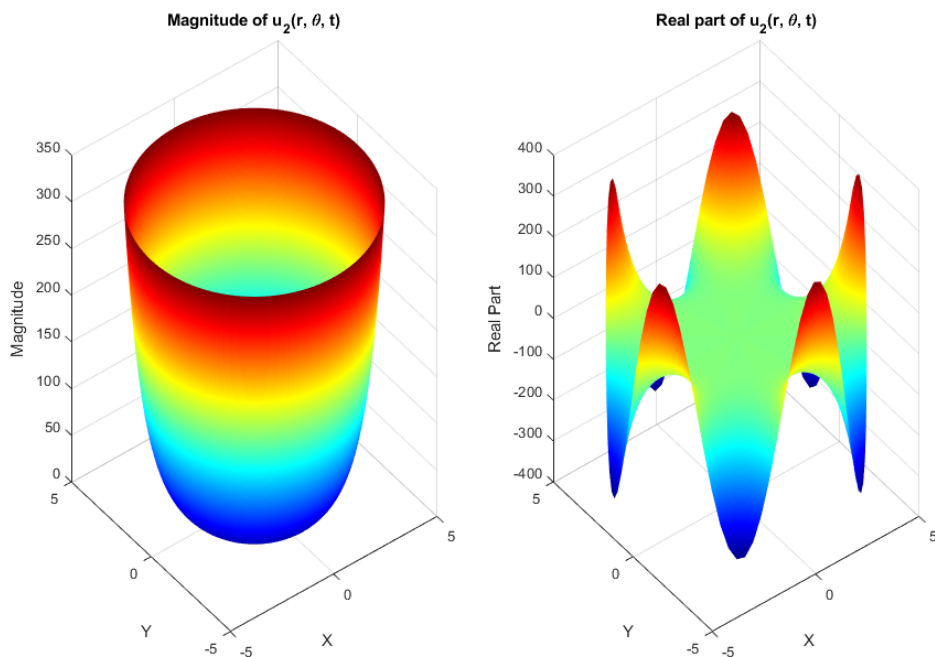
Figure 7. 3D plot of the real part and magnitude of $u_2(r, \theta, t)$

The analysis of the Zakharov-Kuznetsov (ZK) equation (1) with triple-power law nonlinearity reveals that the plasma waves generated in this model exhibit stability of the travelling wave solutions. These solutions, derived through double reduction approach and invariance transformations, demonstrate consistent and predictable propagation characteristics across two spatial dimensions and time. The stability of these waves is a critical finding, as it underscores their potential relevance in modeling multidimensional wave phenomena in plasma physics, such as ion-acoustic waves in magnetized plasmas.

The travelling wave solutions, represented as line solitons, for example (Figures 1-3) maintain their shape and speed over time, a hallmark of soliton behavior. This stability is attributed to the balance between the nonlinear effects introduced
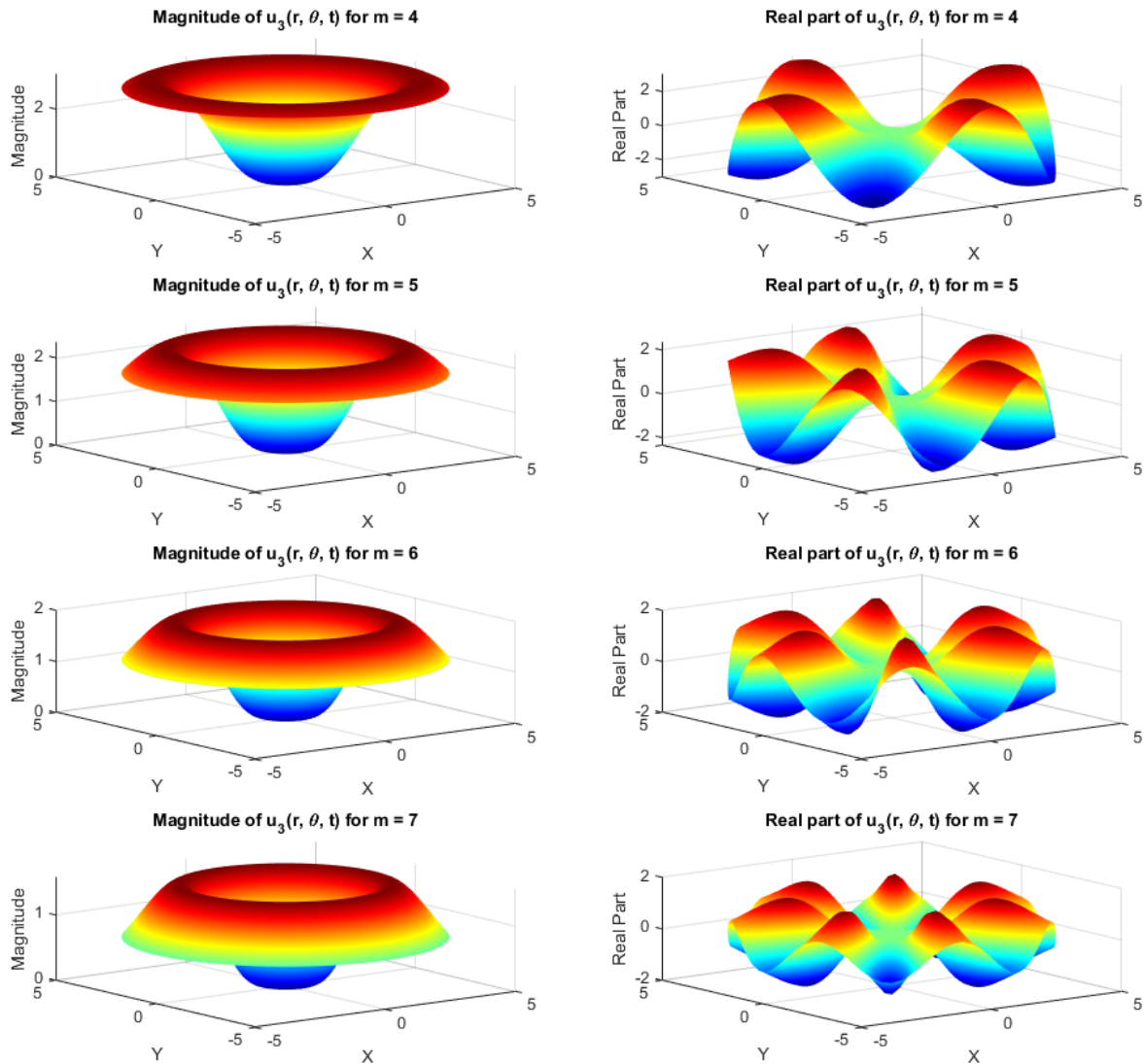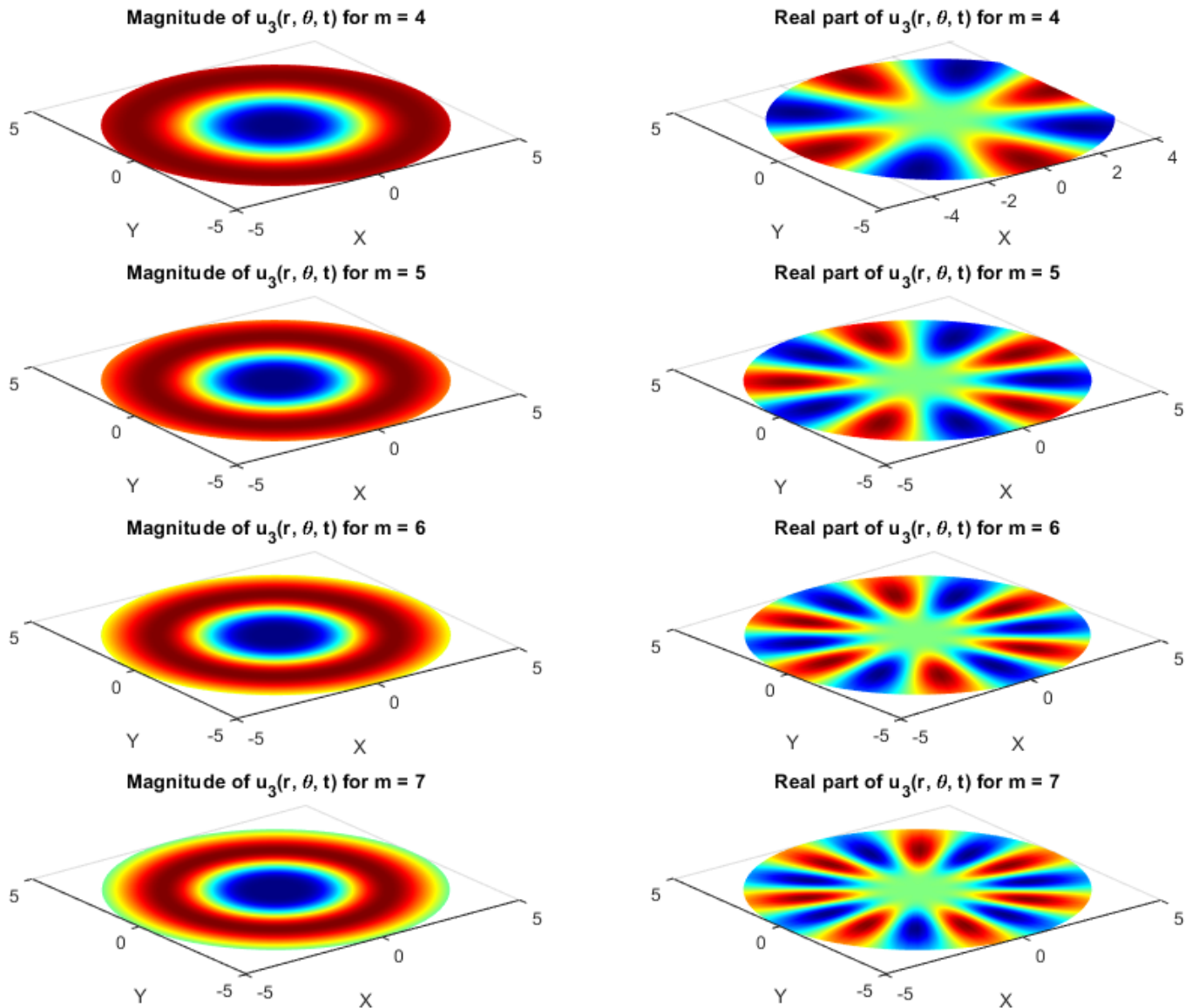
Figure 8. Real part and magnitude of $u_3(r, \theta, t)$

by the triple-power law terms, $G(u) = au^n + bu^{2n} + cu^{3n}$ and the dispersive effects captured by the terms $\sigma(u_{xx} + u_{yy})_x$ in the ZK equation. The absence of significant chaotic or turbulent structures following the initial wave propagation further reinforces the robustness of these solutions. This behavior aligns with the physical interpretation of ion-acoustic solitary waves, which are known to preserve their integrity in plasma environments under the influence of a magnetic field, as noted in prior studies [3, 5].

Similarly, the vortex soliton solutions (Figures 6-9) exhibit a stable, bell-shaped solitary wave profile, characterized by a radial decay governed by the sech^2 function and a phase-dependent oscillatory structure. This suggests that the associated electric field potential, electric field, and magnetic field components remain stable over time and space. The vortex solutions, expressed in polar coordinates as $u(r, \theta, t) = U(r)e^{i(m\theta - \omega t)}$, demonstrate a localized rotating wave pattern that decays to zero as $r \rightarrow \infty$, ensuring the confinement of energy and the absence of unbounded growth or instability. The stability of these vortex structures is particularly significant in the context of plasma physics, where such solutions can model coherent structures like ion-acoustic vortices in two-dimensional systems.

The figures accompanying the travelling wave and vortex soliton solutions provide visual confirmation of this stability. For instance, the 3D plots of the travelling wave solutions (Figures 1-3) depict smooth, non-dispersive wave fronts that propagate without distortion, while the vortex soliton plots (Figures 6-9) illustrate a consistent magnitude and oscillatory pattern across varying parameters, such as the topological charge m. Notably, some figures indicate a non-linear ion-

Figure 9. Real part and magnitude of $u_3(r, \theta, t)$

acoustic solitary wave-like behaviour, characterized by a steepened wave profile that remains stable over time, a feature consistent with experimental observations of ion-acoustic solitons in magnetized plasmas [8].

The amplitudes of the waves, particularly in the complex vortex soliton cases, further highlight their stable behaviour. The magnitude plots (Figures 6-9) show that the wave intensity remains bounded and predictable, with no evidence of amplification or dissipation that would suggest instability. This stability is likely a consequence of the symmetry-invariant conservation laws derived in the study, which impose constraints on the system that prevent chaotic divergence. The use of multipliers to construct these conservation laws facilitates the double reduction process, yielding reduced ODEs that admit stable, integrable solutions.

In all cases, whether travelling waves, multi-solitons, or vortex solitons, the spread of the waves remains controlled, with little to no chaotic structure emerging after the initial wave formation. This stability is particularly pronounced in the multi-soliton solutions (Figure 5), where elastic collisions between solitons occur without loss of form, a property indicative of integrability in the ZK system. Such behavior is consistent with the physical context of weak turbulence in

plasma systems, where solitons maintain their coherence despite interactions, which is a important phenomenon of wave dynamics in space physics and fusion research [6, 7].

Overall, the stable wave behavior observed in this study suggests that the ZK equation with triple-power law nonlinearity provides a robust framework for modeling plasma waves in higher-dimensional settings. The findings have implications for understanding the stability and interaction of nonlinear waves in magnetized plasmas, potentially aiding in the design of experiments or simulations aimed at exploring ion-acoustic solitons and vortex structures in real-world plasma environments.

8. CONCLUSION

A large class of Zakharov-Kuznetsov (ZK) equation with the triple-power law non-linearity were studied. We have shown how a study of the relationship between symmetries and multipliers are attained and then utilised to obtain double reduction from (1+2) ZK equation to an ODE. We determined the invariance properties and constructed classes of conservation laws and discussed how the relationship leads to double reductions of the systems, ensuring stable solutions. Multi-solitons analysis is performed using invariance transformation and vortex soliton solutions. A comparison between symmetry and multi-reduction is presented, highlighting the advantage in producing integrable, stable outcomes. The physical interpretation of soliton solutions is also discussed in this study, emphasizing their stable propagation, evidenced by localized profiles, elastic collisions, and conserved quantities, which models coherent ion-acoustic and vortex waves in magnetized plasmas, offering valuable understanding of wave dynamics in space physics and fusion research.

ORCID

 Ali Raza, https://orcid.org/0000-0002-7593-9923; **Abdul Hamid Kara**, https://orcid.org/0000-0002-0231-0198;
 Sibusiso Moyo, https://orcid.org/0000-0001-5613-7290

REFERENCES

[1] Y. Li, and Y. Kai, "Chaotic behavior of the Zakharov-Kuznetsov equation with dual-power law and triple-power law nonlinearity," AppliedMath, **3**(1), 1-9 (2022). https://doi.org/10.3390/appliedmath3010001

[2] A. Biswas, and E. Zerrad, "1-soliton solution of the Zakharov–Kuznetsov equation with dual-power law nonlinearity," Communications in Nonlinear Science and Numerical Simulation, **14**(9-10), 3574-3577 (2009). https://doi.org/10.1016/j.cnsns.2008.10.004

[3] N.A. El-Bedwehy, and W.M. Moslem, "Zakharov-Kuznetsov-Burgers equation in superthermal electron-positron-ion plasma," Astrophysics and Space Science, **335**, 435-442 (2011). https://doi.org/10.1007/s10509-011-0742-6

[4] N.S. Saini, B.S. Chahal, A.S. Bains, and C. Bedi, "Zakharov-Kuznetsov equation in a magnetized plasma with two temperature superthermal electrons," Physics of Plasmas, **21**(2), 022114 (2014). https://doi.org/10.1063/1.4865590

[5] A.R. Seadawy, "Three-dimensional nonlinear modified Zakharov–Kuznetsov equation of ion-acoustic waves in a magnetized plasma," Computers & Mathematics with Applications, **71**(1), 201-212 (2016). https://doi.org/10.1016/j.camwa.2015.11.006

[6] B.T. Matebese, A.R. Adem, C.M. Khalique, and A. Biswas, "Solutions of Zakharov-Kuznetsov equation with power law nonlinearity in (1+3) dimensions," Physics of Wave Phenomena, **19**, 148-154 (2011). https://doi.org/10.3103/S1541308X11020117

[7] Y. Xiao, "Impacts of a general power law on soliton for a (2+1)-dimensional Zakharov–Kuznetsov equation in magnetized quantum plasmas," Results in Physics, **47**, 106340 (2023). https://doi.org/10.1016/j.rinp.2023.106340

[8] M. Iqbal, A.R. Seadawy, D. Lu, and X. Xia, "Construction of bright–dark solitons and ion-acoustic solitary wave solutions of dynamical system of nonlinear wave propagation," Modern Physics Letters A, **34**(37), 1950309 (2019). https://doi.org/10.1142/S0217732319503097

[9] N.H. Ibragimov, *Transformation groups applied to mathematical physics*, vol. 3, (Springer Science and Business Media, 1984).

[10] P.J. Olver, *Applications of Lie groups to differential equations*, vol. 107, (Springer Science & Business Media, 1993).

[11] Ü. Göktaş, and W. Hereman, "Computation of conservation laws for nonlinear lattices," Physica D: Nonlinear Phenomena, **123**(1-4), 425-436 (1998). https://doi.org/10.1016/S0167-2789(98)00140-7

[12] A.H. Kara, and F.M. Mahomed, "Relationship between symmetries andconservation laws," International Journal of Theoretical Physics, **39**, 23-40 (2000). https://doi.org/10.1023/A:1003686831523

[13] A.H. Kara, and F.M. Mahomed, "A basis of conservation laws for partial differential equations," Journal of Nonlinear Mathematical Physics, **9**(Suppl 2), 60-72 (2002). https://doi.org/10.2991/jnmp.2002.9.s2.6

[14] A.H. Kara, and F.M. Mahomed, "Noether-type symmetries and conservation laws via partial Lagrangians," Nonlinear Dynamics, **45**, 367-383 (2006). https://doi.org/10.1007/s11071-005-9013-9

[15] S.C. Anco, and M.L. Gandarias, "Symmetry multi-reduction method for partial differential equations with conservation laws," Communications in Nonlinear Science and Numerical Simulation, **91**, 105349 (2020). https://doi.org/10.1016/j.cnsns.2020.105349

[16] S.C. Anco, and A.H. Kara, "Symmetry-invariant conservation laws of partial differential equations," European Journal of Applied Mathematics, **29**(1), 78-117 (2018). https://doi.org/10.1017/S0956792517000055

[17] P.J. Olver *Application of Lie Groups to Differential Equations*, (Springer, New York, NY, USA, 1986).

[18] N.H. Ibragimov, *Selected works*, vol. II, (ALGA Publications, Karlskrona, Sweden, 2006).

[19] R. Naz, "Conservation laws for some compacton equations using the multiplier approach," Applied Mathematics Letters, **25**(3), 257-261 (2012). https://doi.org/10.1016/j.aml.2011.08.019

[20] R. Naz, "Conservation laws for some systems of nonlinear partial differential equations via multiplier approach," Journal of Applied Mathematics, **2012**(1), 871253 (2012). https://doi.org/10.1155/2012/871253

[21] M.L. Gandarias, M.R. Durán, and C.M. Khalique, "Conservation laws and travelling wave solutions for double dispersion equations in (1+1) and (2+1) dimensions," Symmetry, **12**(6), 950 (2020). http://dx.doi.org/10.3390/sym12060950

[22] R. Naz, M.D. Khan, and I. Naeem, "Conservation laws and exact solutions of a class of non linear regularized long wave equations via double reduction theory and Lie symmetries," Communications in Nonlinear Science and Numerical Simulation, **18**(4), 826-834 (2013). https://doi.org/10.1016/j.cnsns.2012.09.011

[23] J.E. Allen, "The early history of solitons (solitary waves)," Physica Scripta, 57(3), 436 (1998). https://doi.org/10.1088/0031-8949/57/3/016

[24] A. Kasman, *Glimpses of soliton theory: the algebra and geometry of nonlinear PDEs*, vol. 100, (American Mathematical Society, 2023).

[25] M.S. Khatun, M.F. Hoque, and M.A. Rahman, "Multisoliton solutions, completely elastic collisions and non-elastic fusion phenomena of two PDEs," Pramana - J. Phys. **88**, 86 (2017). https://doi.org/10.1007/s12043-017-1390-3

[26] T. Soomere, "Solitons interactions," in: *Solitons. Encyclopedia of Complexity and Systems Science Series*, edited by M.A.Helal, (Springer, New York, US, 2022), pp. 257-288.

[27] K. Staliunas, "Vortices and dark solitons in the two-dimensional nonlinear Schrödinger equation," Chaos, Solitons & Fractals, 4(8-9), 1783-1796 (1994). https://doi.org/10.1016/0960-0779(94)90111-2

ЗАСТОСУВАННЯ МУЛЬТИРЕДУКЦІЇ ТА МУЛЬТИСОЛІТОННОГО АНАЛІЗУ (2+1) РІВНЯННЯ ЗАХАРОВА-КУЗНЄЦОВА (ZK)

Алі Раза[a,b], **Абдул Хамід Кара**[c], **Сібусісо Мойо**[d]

[a]*Департамент математики та статистичних наук, Лахорська школа економіки, Лахор, Пакистан*

[b]*Департамент математичних наук, Університет Стелленбоша, Стелленбош, Південна Африка*

[c]*Школа математики, Університет Вітватерсранд, Йоганнесбург, Південна Африка*

[d]*Школа даних та обчислювального мислення та факультет математичних наук, Університет Стелленбоша, Стелленбош, 7602, Південна Африка*

Досліджено рівняння Захарова-Кузнєцова (З.К.) з триступеневою нелінійністю. Ми визначаємо властивості інваріантності та будуємо класи законів збереження та показуємо, як зв'язок призводить до подвійного скорочення систем, що дає стабільні рішення, такі як біжучі хвилі та солітони. Цей зв'язок визначається нещодавніми результатами, пов'язаними з «мультипліка-торами», які призводять до «загальних розбіжних систем». Мультисолітонний аналіз виконується за допомогою інваріантного перетворення, утворюючи стабільні багатосолітонні структури разом із вихровими солітонними рішеннями, які демонструють локалізовані дзвоноподібні профілі. Представлено порівняння між симетрією та множинним скороченням, підкреслюючи ефе-ктивність у досягненні інтегрованих результатів. У цьому дослідженні також обговорюється фізична інтерпретація солітонних розчинів, наголошується на їх стабільному поширенні та актуальності для моделювання когерентних іонно-звукових і вихрових хвиль у намагніченій плазмі.

Ключові слова: *подвійне скорочення; закони збереження; множники; рівняння Захарова-Кузнєцова; аналіз інваріантності; солітони; мультисолітони; вихрові солітони*

KDV AND MKDV ION-ACOUSTIC SOLITARY WAVES IN A POSITRON-BEAM PLASMA WITH KANIADAKIS DISTRIBUTED ELECTRONS

Rafia Khanam[a], **Satyendra Nath Barman**[b]

aDepartment of Mathematics, Gauhati University, Guwahati-781014, Assam, India
bB. Borooah College, Guwahati-781007, Assam, India
*Corresponding Author e-mail: rafiakhanam353@gmail.com

Theoretical and numerical studies of ion-acoustic solitary waves (IASWs) in an unmagnetized plasma with ions, positron beams under pressure variation, and kaniadakis distributed electrons have been conducted. The potential wave amplitude is calculated by applying the reductive perturbation approach to reduce the controlling set of normalized fluid equations to Korteweg-de Vries (KdV) and modified Korteweg-de Vries (mKdV) equations. In mKdV solutions, only compressive solitons are found, whereas both compressive and rarefactive KdV solitons are found to exist for different values of σ, σ_b, and ν. The parameter k has no effect on the IASWs of the KdV equation, but have contribution in mKdV solitons. It is also shown that the inclusion of nonthermal electrons drastically changes the basic properties of ion-acoustic solitons and creates a new parametric regime.

Keywords: *Ion-acoustic Solitary waves; Positron-beams; KdV equation; mKdV equation; Kaniadakis distribution*

PACS: 52.35.Fp, 52.35.Qz, 52.35.Sb, 41.75.Fr

1. INTRODUCTION

The reductive perturbation approach provides an excellent description of the ion-acoustic solitary wave studies in ions, positron-beams plasma with nonthermal electrons. In order to do this, the development progresses from the typical ion-electron-positron components to ions, positron beams and nonthermal electrons, reaching an intriguing stage of study. Theoretically, several researchers have investigated the existence of ion-acoustic solitary waves in positron beam plasma systems during the past few decades [1–22]. Greaves and Surko [23] have examined the electron-positron beam-plasma experiment for the first time. Coleman [24] has studied positron beams and their applications in various field. Sarma et al. [25] have investigated relativistic positron beams in nonlinear ion-acoustic solitary waves in an electron-positron-ion plasma. Lynn and Schultz [26] have investigated how positron beams interact with surfaces, thin films, and interfaces. The totally nonlinear acoustic waves in a plasma with superthermal electrons and positron beam impact were examined by Shan et al. [27]. Ion acoustic shock waves in the presence of superthermal electrons and the interaction of a classical positron beam have been explored by Shah et al. [28]. Moreover, Shah et al. [29] investigated the interaction of nonlinear waves with a classical positron beam in nonextensive astrophysical plasmas in an astrophysical naturally moderated setting. Hogan [30] has researched plasma acceleration caused by electron and positron beams. Research on nonlinear ion-acoustic solitary waves in a weakly relativistic electron-positron-ion plasma with relativistic electron and positron beams was conducted by Barman and Talukdar [31]. Roy et al. [32] have investigated the effects of relativistic positron beams on ion-acoustic breather, periodic, and solitary waves in the ionospheric area of earth using the mKdV equation and the KdV framework.

A lot of attention has been paid to numerous entropic forms that generalize the conventional Boltzmann-Gibbs Shannon one over the last few decades. Initially, Renyi [33] introduced the generalization of the Boltzmann-Gibbs (BG) statistics. Later it was developed by Tsallis [34]. The Tsallis nonextensive theory was one such theory that showed its effectiveness in managing particular complicated systems and also showed an astonishingly high degree of agreement with experimental evidence [35]. Quantum entanglement, blackbody radiation, and the k-statistics derived from the kaniadakis entropy [36] were all reviewed within the theoretical framework. It has been investigated how the putative k-deformed distributions caused by the kaniadakis entropy relate to cosmic rays [37], quark-gluon plasma production [38], interacting photon and atom kinetics [39], and nonlinear kinetics [40]. It has been investigated [41, 42] for arbitrary amplitude electron-acoustic waves in unmagnetized plasma with a k-deformed kaniadakis electron distribution. Kalita *et al.* [43] have investigated nonlinear dust ion acoustic solitary waves in an unmagnetized plasma involving kaniadakis distributed electrons and temperature ratio. Khalid *et al.* [44] have conducted research using kaniadakis distributed electrons in dust ion acoustic solitary waves in unmagnetized plasma. High relativistic effect on dust-ion-acoustic solitary waves in unmagnetized plasma with kaniadakis distributed electrons has been investigated by Das and Das [45]. Raut *et al.* [46] have investigated dust ion acoustic shock waves, soliton, and bi-soliton in unmagnetized plasma with electrons dispersed according to kaniadakis in both planar and nonplanar geometry. Tribeche and Lourek's [47] have studied on the function of the k-deformed kaniadakis distribution in nonlinear plasma waves. Irshad *et al.* [48] have studied the influence of

the k-deformed kaniadakis distribution on the modulational instability of electron-acoustic waves in a non-Maxwellian plasma.

In this paper we have established the existence of KdV and mKdV solitons in a three-component plasma consisting of ions, positron beams, and kaniadakis distributed electrons using the reductive perturbation approach. KdV solutions contain both compressive and rarefactive solitons, but only compressive solitons are present in mKdV solitons for the effects of σ, σ_b, ν, and k. The structure of our paper is as follows: in Section [1] , we have presented the usual 'Introduction' ; in Section [2], we have mentioned the 'Basic Equations Governing the Dynamics of Motion'; Section [3] and Section [4] include the 'Derivation of KdV and mKdV Equation and Its Solution'; Section [5] is incorporated the 'Results and Discussions'; and in Section [6] we have presented the 'Conclusion' of the outcome.

2. BASIC EQUATIONS GOVERNING THE DYNAMICS OF MOTION

We have considered the propagation of three component collisionless ion-acoustic waves in a warm unmagnetized plasma with ion, positron-beam and nonthermal electrons. For such a plasma model, the basic equations governing the plasma dynamics of ion-acoustic waves are described by the following normalized equations

$$\frac{\partial n}{\partial t} + \frac{\partial (nu)}{\partial x} = 0 \tag{1}$$

$$\frac{\partial u}{\partial t} + u\frac{\partial u}{\partial x} = -\left(\frac{\partial \phi}{\partial x} + \frac{\sigma}{n}\frac{\partial p}{\partial x}\right) \tag{2}$$

$$\frac{\partial p}{\partial t} + u\frac{\partial p}{\partial x} = -3p\frac{\partial u}{\partial x} \tag{3}$$

$$\frac{\partial n_b}{\partial t} + \frac{\partial (n_b w)}{\partial x} = 0 \tag{4}$$

$$\frac{\partial w}{\partial t} + w\frac{\partial w}{\partial x} = -\left(\frac{\partial \phi}{\partial x} + \frac{\sigma_b}{n_b}\frac{\partial p_b}{\partial x}\right) \tag{5}$$

$$\frac{\partial p_b}{\partial t} + w\frac{\partial p_b}{\partial x} = -3p_b\frac{\partial w}{\partial x} \tag{6}$$

$$\frac{\partial^2 \phi}{\partial x^2} = (1 - \nu)n_e - n - \nu n_b \tag{7}$$

where n, n_b, u, w, p, and p_b respectively denote the ion number density, positron-beam number density, the ion fluid velocity, positron-beam fluid velocity, pressure variation of ion and the pressure variation of positron-beam. Also $\nu = n_{b0}/n_0$ is the positron beam to ion number density ratio; $\sigma = T_i/T_e$ is the ion to electron temperature ratio; $\sigma_b = T_b/T_e$ is the positron beam to electron temperature ratio. In the above equations, the particle number densities n, n_b and n_e are normalized by unperturbed electron number density n_{e0}; velocity u, w by the ion-acoustic speed $c_s = (T_e/m_i)^{1/2}$; pressures p by the characteristic ion pressure eT_i; the time t by the inverse of the characteristic ion plasma frequency $\omega_{pi}^{-1} = (m/4\pi n_0 e^2)^{1/2}$; the distance x by the Debye length $\lambda_{De} = (T_e/4\pi n_0 e^2)^{1/2}$.

The electrons follow k-deformed KD [38] which is expressed as:

$$f_e^{(k)}(u_b) = A_k exp_k \left(-\frac{m_e u_b^2/2 - e\varphi}{T_e}\right)$$

with $(u, w) = u_b$

$$exp_k(x) = \left(\sqrt{1 + k^2 x^2} + kx\right)^{\frac{1}{k}},$$

and A_k is the normalized constant indicated by :

$$A_k = n_{e0}\left(\frac{m_e|k|}{\pi T_e}\right)^{3/2} \frac{\Gamma(\frac{1}{2|k|} + \frac{3}{4})}{\Gamma(\frac{1}{2|k|} - \frac{3}{4})}\left(1 + \frac{3}{2}|k|\right).$$

The following standard integration is applied for calculating A_k :

$$\int_0^\infty x^{s-1} exp_k(-x)dx = \frac{[1 + (s-2)|k|]|2k|^{-s}\Gamma(\frac{1}{2|k|} - \frac{s}{2})}{[1 - (s-1)|k|]^2 - k^2 \Gamma(\frac{1}{2|k|} + \frac{s}{2})}\Gamma(s)$$

Here, k is a real parameter and Γ stands for the universal gamma function that indicates the degree of deformation. The inequality $|k| < 1$ must hold for real value of the parameter.

The quantity k represents the dispersion from the Maxwellian distribution; hence, when $k \to 0$, the KD function is transformed into the Maxwell-Boltzmann distribution as follows:

$$\lim_{k \to 0} f_e^{(k)}(u_b) = n_{e0}(\frac{m_e}{2\pi T_e})^{\frac{3}{2}} exp\left(-\frac{(m_e u_b^2/2) - e\varphi}{T_e}\right)$$

with

$$\lim_{k \to 0} exp_k(x) \approx exp(x).$$

Prior to continuing, it is crucial to limit the acceptable range of k. Calculation of the mean square speed $\prec u_b^2 \succ$ requires the following:

$$\prec u_b^2 \succ = \frac{\iiint u_b^2 f_e^{(k)}(u_b) d^3 u_b}{\iiint f_e^{(k)}(u_b) d^3 u_b} = \frac{2T_e/m_e}{|2k|^{5/2}(1 + \frac{5}{2}|k|)} \frac{\Gamma(\frac{1}{2|k|} - \frac{5}{4})}{\Gamma(\frac{1}{2|k|} + \frac{5}{4})}$$

To preserve the physical meaning of $\prec u_b^2 \succ$, which necessitates that $\prec u_b^2 \succ$ be finite and whose value diverges at $k \to 0.4$, the appropriate value of k must satisfy the inequality $k < 0.4$. It should be mentioned that this restriction is taken into account while determining A_k and the particles' average kinetic energy, $m \prec u_b^2 \succ /2$, and that the interacting particles are ignored, i.e., $\phi = 0$.

By integrating $f_e^{(k)}(u_b)$ throughout velocity space, the electron density is calculated and is as follows:

$$n_e = \left(\sqrt{1 + k^2\phi^2} + k\phi\right)^{\frac{1}{k}},$$

$$\implies n_e = 1 + \phi + \frac{1}{2}\phi^2 + \frac{(1 - k^2)}{6}\phi^3 + \dots \tag{8}$$

3. DERIVATION OF KDV EQUATION AND ITS SOLUTIONS

To derive the KdV equation from (1)-(8), we apply the reductive perturbation method. we consider a new set of stretched variables as

$$\xi = \epsilon^{1/2}(x - Ut), \quad \tau = \epsilon^{3/2}t \tag{9}$$

where U is the waves' phase velocity and ϵ is a small, non-dimensional parameter that quantifies the degree of nonlinearity. The flow variables are then expanded asymptotically about the stable equilibrium state in terms of ϵ as follows:

$$\begin{aligned}
n &= n_0 + \epsilon n_1 + \epsilon^2 n_2 + \epsilon^3 n_3 + \dots \\
u &= \epsilon u_1 + \epsilon^2 u_2 + \epsilon^3 u_3 + \dots \dots \dots \\
p &= p_0 + \epsilon p_1 + \epsilon^2 p_2 + \epsilon^3 p_3 + \dots \\
n &= n_{b0} + \epsilon n_{b1} + \epsilon^2 n_{b2} + \epsilon^3 n_{b3} + \dots \\
w &= \epsilon w_1 + \epsilon^2 w_2 + \epsilon^3 w_3 + \dots \dots \\
p &= p_{b0} + \epsilon p_{b1} + \epsilon^2 p_{b2} + \epsilon^3 p_{b3} + \dots \\
\phi &= \epsilon \phi_1 + \epsilon^2 \phi_2 + \epsilon^3 \phi_3 + \dots \dots
\end{aligned} \right\} \tag{10}$$

Using the transformation (9) and the expansions (10) in the equations (1)-(8) and equating the coefficients of the first lowest-order of ϵ with the use of the boundary conditions $n_1 = n_{b1} = 0$, $u_1 = w_1 = 0$, $\phi_1 = 0$ at $|\xi| \longrightarrow \infty$, we get

$$\left.\begin{aligned}
n_1 &= \frac{n_0\phi_1}{U^2 - 3\sigma}; \quad u_1 = \frac{U\phi_1}{U^2 - 3\sigma}; \quad p_1 = \frac{3p_0\phi_1}{U^2 - 3\sigma}; \\
n_{b1} &= \frac{n_{b0}\phi_1}{U^2 - 3\sigma_b}; \quad w_{b1} = \frac{U\phi_1}{U^2 - 3\sigma_b}; \quad p_{b1} = \frac{3p_{b0}\phi_1}{U^2 - 3\sigma_b}
\end{aligned}\right\} \tag{11}$$

From equation (4) we get,

$$(1 - \nu)\phi_1 - n_1 - \nu n_{b1} = 0 \tag{12}$$

Using the expressions of n_1 and n_{b1} from (11), the expression for phase speed U is found as

$$U^2 = \frac{-y \pm \sqrt{y^2 - 4xz}}{2x} \tag{13}$$

where $x = 1 - \nu$
$$y = -3(1 - \nu)(\sigma + \sigma_b) - n_0 - \nu n_{b0}$$

$$z = 9\sigma\sigma_b(1 - \nu) + 3(n_0\sigma_b + \nu\sigma n_{b0})$$

Again, equating the coefficients of second higher-order terms of ϵ from (1)-(6), we get the followings,

$$\frac{\partial n_1}{\partial \tau} - U\frac{\partial n_2}{\partial \xi} + n_0\frac{\partial u_2}{\partial \xi} + \frac{\partial(n_1 u_1)}{\partial \xi} = 0 \tag{14}$$

$$n_0\frac{\partial u_1}{\partial \tau} - Un_0\frac{\partial u_2}{\partial \xi} - Un_1\frac{\partial u_1}{\partial \xi} + n_0u_1\frac{\partial u_1}{\partial \xi} + \sigma\frac{\partial p_2}{\partial \xi} + n_0\frac{\partial \phi_2}{\partial \xi} + n_1\frac{\partial \phi_1}{\partial \xi} = 0 \tag{15}$$

$$\frac{\partial p_1}{\partial \tau} - U\frac{\partial p_2}{\partial \xi} + u_1\frac{\partial p_1}{\partial \xi} + 3p_0\frac{\partial u_2}{\partial \xi} + 3p_1\frac{\partial u_1}{\partial \xi} = 0 \tag{16}$$

$$\frac{\partial n_{b1}}{\partial \tau} - U\frac{\partial n_{b2}}{\partial \xi} + n_{b0}\frac{\partial w_2}{\partial \xi} + \frac{\partial(n_{b1}w_1)}{\partial \xi} = 0 \tag{17}$$

$$n_{b0}\frac{\partial w_1}{\partial \tau} - Un_{b0}\frac{\partial w_2}{\partial \xi} - Un_{b1}\frac{\partial w_1}{\partial \xi} + n_{b0}w_1\frac{\partial w_1}{\partial \xi} + \sigma_b\frac{\partial p_{b2}}{\partial \xi} + n_{b0}\frac{\partial \phi_2}{\partial \xi} + n_{b1}\frac{\partial \phi_1}{\partial \xi} = 0 \tag{18}$$

$$\frac{\partial p_{b1}}{\partial \tau} - U\frac{\partial p_{b2}}{\partial \xi} + w_1\frac{\partial p_{b1}}{\partial \xi} + 3p_{b0}\frac{\partial w_2}{\partial \xi} + 3p_{b1}\frac{\partial w_1}{\partial \xi} = 0 \tag{19}$$

Similarly, from equation(7), we obtain

$$\frac{\partial^2 \phi_1}{\partial \xi^2} = (1 - \nu)(\phi_2 + \frac{1}{2}\phi_1^2) - n_2 - \nu n_{b2}$$

$$\implies \frac{\partial^3 \phi_1}{\partial \xi^3} = (1 - \nu)\frac{\partial \phi_2}{\partial \xi} + (1 - \nu)\phi_1\frac{\partial \phi_1}{\partial \xi} - \frac{\partial n_2}{\partial \xi} - \nu\frac{\partial n_{b2}}{\partial \xi} \tag{20}$$

Now, putting the values of $\partial n_0/\partial \xi$ and $\partial n_{b0}/\partial \xi$ from (14)-(19) and using the relations (20), the KdV equation is obtained as

$$\frac{\partial \phi_1}{\partial \tau} + p\phi_1\frac{\partial \phi_1}{\partial \xi} + q\frac{\partial^3 \phi_1}{\partial \xi^3} = 0 \tag{21}$$

where the nonlinear coefficients p and dispersion coefficient q are given by

$$p = \frac{3n_0(U^2 - 3\sigma_b)^3(U^2 + \sigma) + 3\nu n_{b0}(U^2 - 3\sigma)^3(U^2 + \sigma_b) - (1 - \nu)(U^2 - 3\sigma)^3(U^2 - 3\sigma_b)^3}{2U(U^2 - 3\sigma)(U^2 - 3\sigma_b)\left[(U^2 - 3\sigma_b)^2 n_0 + (U^2 - 3\sigma)^2\nu n_{b0}\right]};$$

$$q = \frac{(U^2 - 3\sigma)^2(U^2 - 3\sigma_b)^2}{2U\left[(U^2 - 3\sigma_b)^2 n_0 + (U^2 - 3\sigma)^2\nu n_{b0})\right]}$$

A new transformation $\eta = \xi - V\tau$ is introduced to discover the stationary solitary wave solutions to the Korteweg-de Vries(KdV) equation(21). In this transformation, V represents the soliton speed in the linear $\eta-$space. The solution for the solitary wave can be obtained by integrating this transformation into the partial differential equation (21) as

$$\phi_1 = \phi_0 \operatorname{sech}^2\left(\frac{\eta}{\Delta}\right) \tag{22}$$

where $\phi_0 = 3V/p$ is the amplitude of the ion-acoustic soliton, and $\Delta = \sqrt{4q/V}$ is the width of the ion-acoustic soliton.

4. DERIVATION OF THE MKDV AND ITS SOLUTION

Equation (21) shows that the nonlinear coefficient p is determined by the plasma parameters ν, σ, σ_b. Higher order nonlinearity requires $p = 0$ in the KdV Eqn. (21). Consequently, the critical density ν_c is obtained, which may be computed as

$$\nu_c = \frac{2(U^2 - 3\sigma)^3(U^2 - 3\sigma_b)^3 - 3n_0(U^2 - 3\sigma)^3(U^2 + \sigma)}{2(U^2 - 3\sigma)^3(U^2 - 3\sigma_b)^3 + 3n_{b0}(U^2 - 3\sigma)^3(U^2 + \sigma_b)} \tag{23}$$

In order to characterize the system at or near the critical point ν_c given in (23). Different stretched variables are provided for higher-order non-linearity as:

$$\eta = \epsilon(x - Ut), \quad \tau = \epsilon^3 t \tag{24}$$

Utilizing the new stretched variables of (24) and expansions (10), the equations (1)-(6) provide the same (13) for the phase velocity U. The second higher order perturbation of ϵ can be obtained as

$$
\left.
\begin{aligned}
n_2 &= \frac{3n_0(U^2+\sigma)\phi_1^2}{2(U^2-3\sigma)^3} + \frac{n_0\phi_2}{U^2-3\sigma}, \qquad & n_{b2} &= \frac{3n_{b0}(U^2+\sigma_b)\phi_1^2}{2(U^2-3\sigma_b)^3} + \frac{n_{b0}\phi_2}{U^2-3\sigma_b}, \\[2mm]
u_2 &= \frac{(U^3+9U\sigma)\phi_1^2}{2(U^2-3\sigma)^3} + \frac{U\phi_2}{U^2-3\sigma}, \qquad & w_2 &= \frac{(U^3+9U\sigma_b)\phi_1^2}{2(U^2-3\sigma_b)^3} + \frac{U\phi_2}{U^2-3\sigma_b}, \\[2mm]
p_2 &= \frac{3n_0(5U^2-3\sigma)\phi_1^2}{2(U^2-3\sigma)^3} + \frac{3n_0\phi_2}{U^2-3\sigma}, \qquad & p_{b2} &= \frac{3n_{b0}(5U^2-3\sigma_b)\phi_1^2}{2(U^2-3\sigma_b)^3} + \frac{3n_{b0}\phi_2}{U^2-3\sigma_b}
\end{aligned}
\right\}
\tag{25}
$$

Next, we enter the values of n_2 in the associated second-order partial differential equation to the relation

$$
(1-\nu_c)\left(\phi_2+\frac{1}{2}\phi_1^2\right) - n_2 - \nu_c n_{b2} = 0
\tag{26}
$$

We obtain the following equations by taking into account the third higher order terms of ϵ from (1)-(6).

$$
\frac{\partial n_1}{\partial \tau} - U\frac{\partial n_3}{\partial \xi} + n_0\frac{\partial u_3}{\partial \xi} + \frac{\partial (n_1 u_2)}{\partial \xi} + \frac{\partial (n_2 u_1)}{\partial \xi} = 0
\tag{27}
$$

$$
n_0\frac{\partial u_1}{\partial \tau} - Un_0\frac{\partial u_3}{\partial \xi} - Un_1\frac{\partial u_2}{\partial \xi} - Un_2\frac{\partial u_1}{\partial \xi} + n_0 u_1\frac{\partial u_2}{\partial \xi} + n_0 u_2\frac{\partial u_1}{\partial \xi} + n_1 u_1\frac{\partial u_1}{\partial \xi} + \sigma\frac{\partial p_3}{\partial \xi}
$$
$$
+ n_0\frac{\partial \phi_3}{\partial \xi} + n_1\frac{\partial \phi_2}{\partial \xi} + n_2\frac{\partial \phi_1}{\partial \xi} = 0
\tag{28}
$$

$$
\frac{\partial p_1}{\partial \tau} - U\frac{\partial p_3}{\partial \xi} + u_1\frac{\partial p_2}{\partial \xi} + u_2\frac{\partial p_1}{\partial \xi} + 3p_0\frac{\partial u_3}{\partial \xi} + 3p_1\frac{\partial u_2}{\partial \xi} + 3p_2\frac{\partial u_1}{\partial \xi} = 0
\tag{29}
$$

$$
\frac{\partial n_{b1}}{\partial \tau} - U\frac{\partial n_{b3}}{\partial \xi} + n_{b0}\frac{\partial w_3}{\partial \xi} + \frac{\partial (n_{b1} w_2)}{\partial \xi} + \frac{\partial (n_{b2} w_1)}{\partial \xi} = 0
\tag{30}
$$

$$
n_{b0}\frac{\partial w_1}{\partial \tau} - n_{b0}U\frac{\partial w_3}{\partial \xi} - Un_{b1}\frac{\partial w_2}{\partial \xi} - Un_{b2}\frac{\partial w_1}{\partial \xi} + n_{b0}w_1\frac{\partial w_2}{\partial \xi} + n_{b0}w_2\frac{\partial w_1}{\partial \xi} + n_{b1}w_1\frac{\partial w_1}{\partial \xi} + \sigma_b\frac{\partial p_{b3}}{\partial \xi}
$$
$$
+ n_{b0}\frac{\partial \phi_3}{\partial \xi} + n_{b1}\frac{\partial \phi_2}{\partial \xi} + n_{b2}\frac{\partial \phi_1}{\partial \xi} = 0
\tag{31}
$$

$$
\frac{\partial p_{b1}}{\partial \tau} - U\frac{\partial p_{b3}}{\partial \xi} + w_1\frac{\partial p_{b2}}{\partial \xi} + w_2\frac{\partial p_{b1}}{\partial \xi} + 3p_{b0}\frac{\partial w_3}{\partial \xi} + 3p_{b1}\frac{\partial w_2}{\partial \xi} + 3p_{b2}\frac{\partial w_1}{\partial \xi} = 0
\tag{32}
$$

Eliminating n_3, n_{b3}, u_3 and w_3 from equations (27)–(32) we get,

$$
\frac{\partial \phi}{\partial \tau} + p'\phi^2\frac{\partial \phi}{\partial \xi} + q'\frac{\partial^3 \phi}{\partial \xi^3} = 0
\tag{33}
$$

where the higher order nonlinear coefficient p' and dispersion coefficient q' are given by

$$
p' = \frac{15U^2\left[U^2+6\sigma+\nu_c(U^2+6\sigma_b)\right] + 27(\sigma^2+\nu_c\sigma_b^2) - (1-k^2)(1-\nu_c)(U^2-3\sigma)^5(U^2-3\sigma_b)^5}{4U(U^2-3\sigma)^3(U^2-3\sigma_b)^3\left[(U^2-3\sigma_b)^2 n_0 + (U^2-3\sigma)^2\nu_c n_{b0})\right]},
$$

$$
q' = \frac{(U^2-3\sigma)^2(U^2-3\sigma_b)^2}{2U\left[(U^2-3\sigma_b)^2 n_0 + (U^2-3\sigma)^2\nu_c n_{b0}\right]}
$$

Using the same transformation and following the steps outlined in section[3], the solutions of mKdV equation (33) is obtained as

$$
\phi_1' = \sqrt{\frac{6V}{p'}}\,\operatorname{sech}\left(\sqrt{\frac{V}{q'}}\,\chi\right)
\tag{34}
$$

where V represents the soliton speed; $\phi_0' = \sqrt{6V/p'}$ and $\Delta' = \sqrt{q'/V}$ indicate, respectively, the amplitude and width of the solitary waves represented by the mKdV equation(33).

5. RESULTS AND DISCUSSIONS

The present work has examined the characteristics of ion-acoustic solitary waves (IASWs) in the context of kaniadakis-deformed electrons k. A numerical analysis is done on the effects of different plasma parameters on the variations of nonlinear term p and dispersion term q given in (21). These parameters include ion-to-electron temperature ratio $\sigma(=T_i/T_e)$, positron beam-to-electron temperature ratio $\sigma_b(=T_b/T_e)$, positron-beam to ion number density ν and the deformation parameter k.
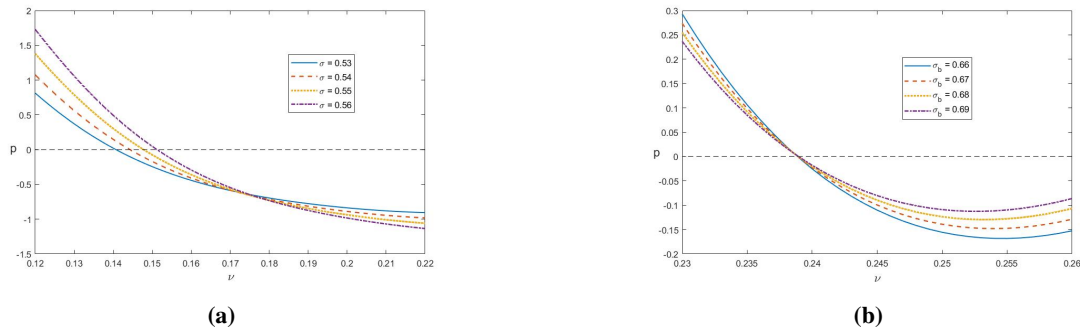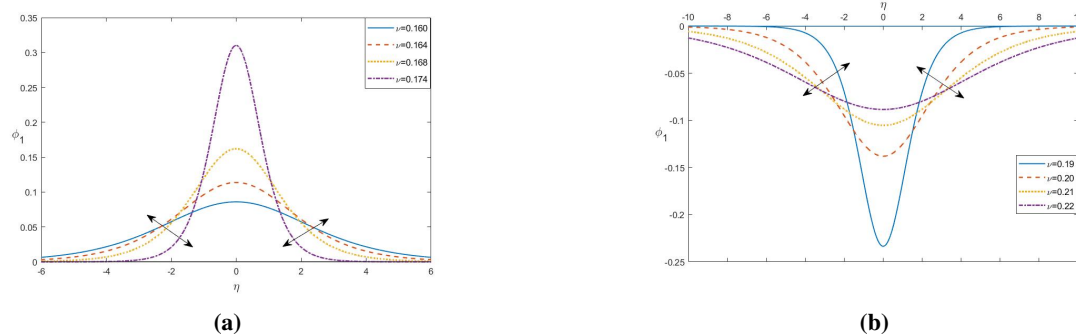

Figure 1. Variation of p versus ν for different values of (a) σ and (b) σ_b.

Figure(1a-1b) describes the variation of nonlinearity of the plasma system for different values of (a) $\sigma = 0.53, 0.54, 0.55, 0.56$ with $\sigma_b = 0.11$ and (b) $\sigma_b = 0.66, 0.67, 0.68, 0.69$ with $\sigma = 0.65$ and other parameters $n_0 = 0.1$, $n_{b0} = 0.1$, $\nu = 0.12$, and $V = 0.05$. The nonlinear coefficient p of the KdV Eq.(21) can have positive, zero and negative values. So, p represents compressive or rarefactive according as $p > 0$ or $p < 0$ and p vanishes or $p \approx 0$ at specific sets of critical values. This represents the singularity shown in Figures (1a) and (1b).
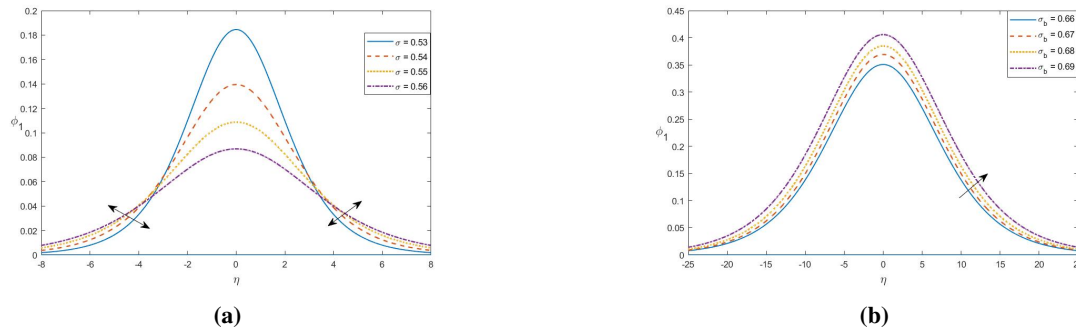
Figure 2. Variation of ϕ_1 versus η for different values of (a) σ and (b) σ_b.

The ion acoustic solitary wave is compressive, as can be seen from Figures (2a-2b). In Figure (2a), the amplitude decreases and the width slightly increases for increasing values of σ with the same fixed values as mentioned in Figure (1), while in Figure (2b), both the amplitude and width rises as increase values of σ_b.

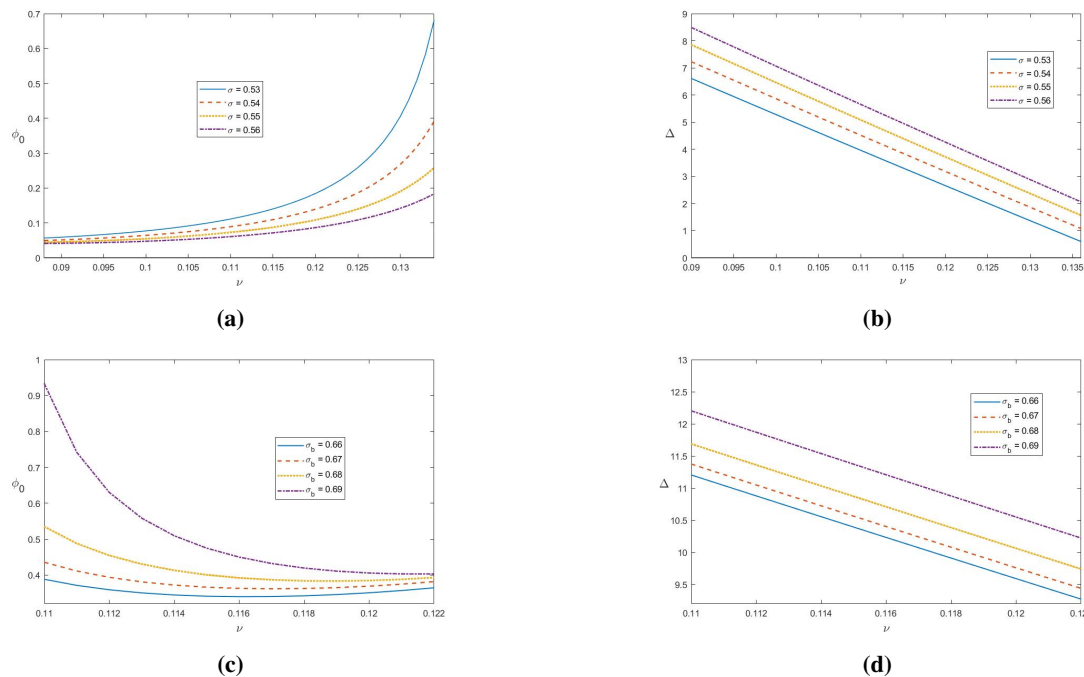**Figure 3.** Variation of ϕ_1 versus η for different values of ν.

For fixed parameters as $\sigma_b = 0.11$, $\sigma = 0.65$, $n_0 = 0.1$, $n_{b0} = 0.1$, and $V = 0.05$, how the number density ν effects on the propagating ion-acoustic solitary waves are shown in Figure [3]. The soliton type is observed to have changed

from compressive to rarefactive at ν depending on σ and σ_b. With rising values of $\nu < \nu_c$, the soliton is compressive (Fig.-[3a]) and amplitude of positive potential ion-acoustic solitary waves increases notably while width decreases slightly. Conversely, for increasing values of $\nu > \nu_c$, the soliton is rarefactive (Fig.-[3b]) and decreases the pulse of negative potential ion-acoustic solitary waves in both amplitude and width. It is noticed that ν plays a crucial role for the existence of both compressive and rarefactive solitons.


(a)   (b)
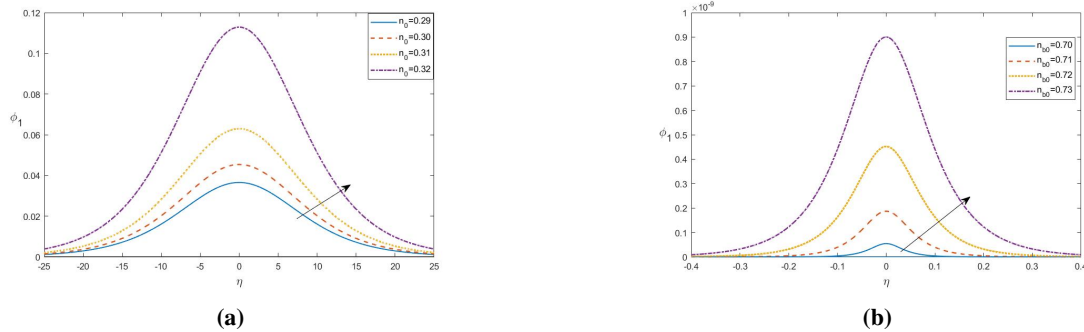
Figure 4. Variation of ϕ_1 versus η for different values of (a) n_b and (b) n_{b0}.

The variation of the amplitude and width of the fast compressive KdV soliton profiles for different values of ion number density n_0 effect is shown in Figure (4a) and positron beam number density n_{b0} effect is shown in Figure (4b). It is seen that both the amplitude and the width of the fast compressive KdV soliton increases with the increase of n_0 and n_{b0}.
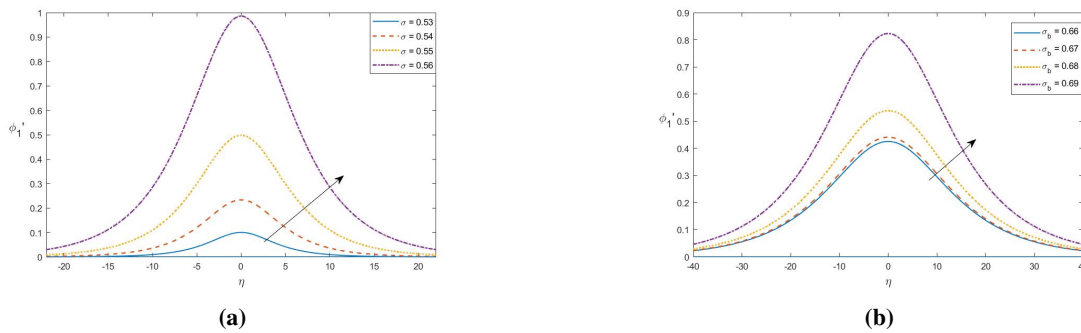

(a)   (b)

(c)   (d)

Figure 5. Variation of ϕ_0 versus ν for different values of (a) σ and (c) σ_b and variation of Δ versus ν for different values of (b) σ and (d) σ_b

In Figure (5a), the fast compressive KdV soliton's amplitude gradually increases in the lower range of $\nu \leq 0.14$ for different values of σ, and for fixed values of $\sigma_b = 0.11$, $n_0 = 0.1$, $n_{b0} = 0.1$, and $V = 0.05$, while in Figure (5c), the amplitude reduces in the lower range of $\nu \leq 0.122$ for different values of σ_b. However, the width decreases uniformly for both the cases. In Figure (6a), the fast compressive KdV soliton amplitude increases as the increasing values of $\nu = 0.160, 0.164, 0.168, 0.174$ for fixed other parameters $\sigma = 0.65$, $n_0 = 0.1$, $n_{b0} = 0.1$, $k = 0.3$ and $V = 0.05$, and Figure (6b) shows that for the fast compressive mKdV soliton, the amplitude monotonically increases for the same various values of ν and also same fixed values. In Figure (6c), the fast rarefactive KdV soliton amplitude increases as the increasing values of $\nu = 0.19, 0.20, 021, 0.22$ for fixed same values in Figure (6a), and Figure (6d) shows that for the fast compressive mKdV soliton, amplitude decreases for the same various values of ν. However, calculation reveals that the width exhibits a consistent character, with the same set of parametric values for every graph in Figure (6).

(a)

(b)

(c)

(d)
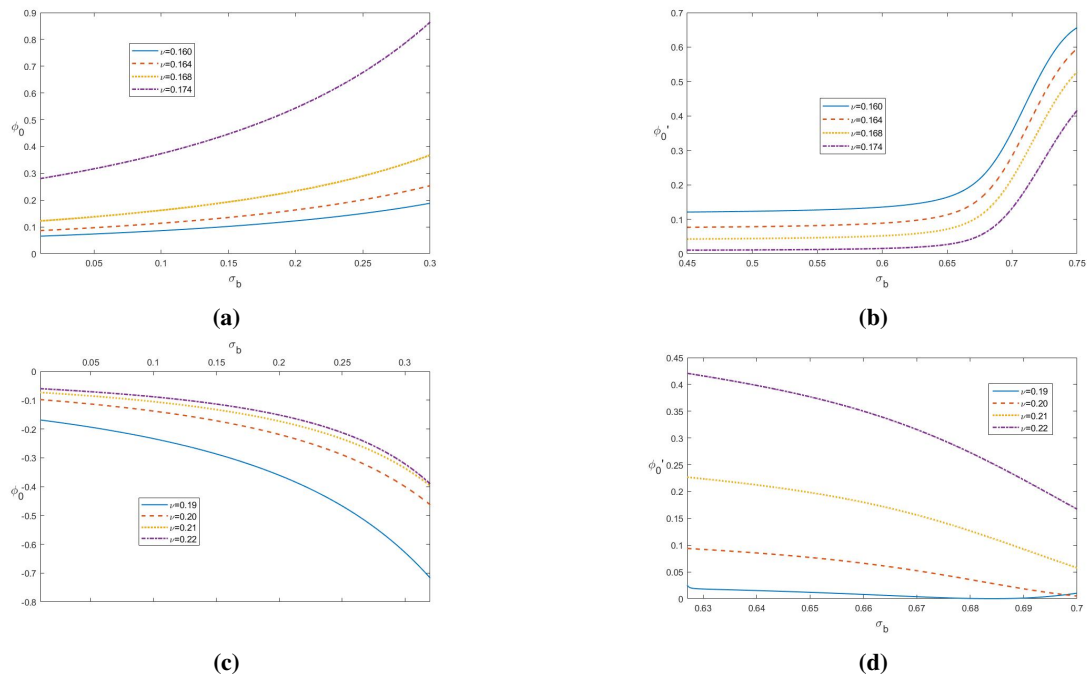
Figure 6. Variation of ϕ_0 versus σ_b for different values of ν in (a) and (c), and variation of ϕ_0' versus σ_b in different values of ν for (b) and (d).

(a)

(b)

Figure 7. Variation of ϕ_1' versus η for different values of (a) σ and (b) σ_b.

Next, we plot the higher-order solitary wave potential $\phi_1'(\eta)$ versus η for fixed values of $n_0 = 0.1$, $n_{b0} = 0.1$, $k = 0.3$ and $V = 0.05$ in Figure (7a-7b) with varying values of (a) σ with $\nu = 0.12$ and (b) σ_b with $\nu = 0.191$. For both the cases, only compressive mKdV ion-acoustic soliton is found to exist.

(a)

(b)
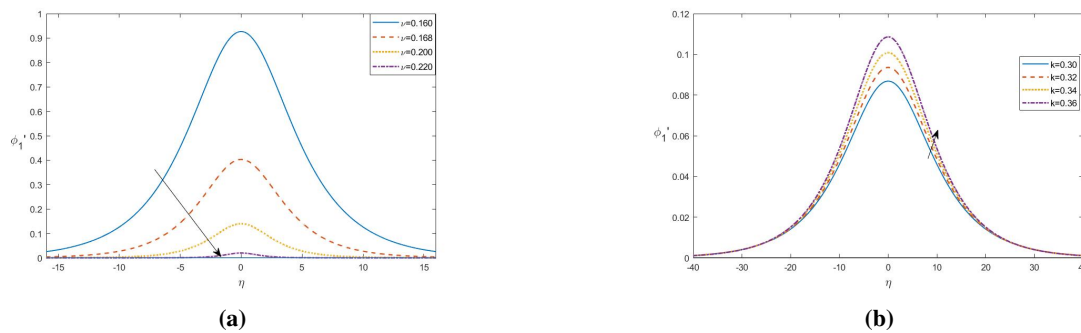
Figure 8. Variation of ϕ_1' versus η for different values of (a) ν with $k = 0.3$ and (b) k.

The variations of $\phi_1'(\eta)$ versus η for various values of (a) $\nu = 0.160, 0.168, 0.200, 0.220$ and (b) $k = 0.30, 0.32, 0.34,$ 0.36 respectively, with other parameters $n_0 = 0.1$, $n_{b0} = 0.1$, $\sigma = 0.65$, $\sigma_b = 0.11$, $\nu = 0.12$ and $V = 0.05$ are shown

in Figures (8a-8b). From both the figures we observed that ϕ_1' is compressive. It can be observed that as ν increases, the ion-acoustic solitary waves amplitude and width decrease monotonically in Figure (8a) and in Figure (8b) the amplitude of compressive ion-acoustic solitary waves is shown to increase as k increases, but the width does not change significantly.

6. CONCLUSION

We have investigated the propagation of ion-acoustic solitary waves in an unmagnetized plasma model with kaniadakis-distributed electrons, ions, and positron beams. The reductive perturbation method is used to derive the KdV and mKdV equations and to obtain their solitary wave solutions. Physical parameters such as ν, the positron beam to ion number density ratio; σ, the ion to electron temperature ratio; σ_b, the positron to electron temperature ratio and the parameter k play a crucial role in giving the soliton character. The outcomes that have been observed in this study can be contracted as follows:

1. It is found that there are two different types of wave modes in the current plasma model: slow acoustic modes and fast ion-acoustic modes. However, we only take into account fast ion-acoustic modes for extracting KdV and mKdV equations, because slow modes do not give any possibility for the existence of soliton.

2. The first order non-linear coefficient p in the KdV equation can be a positive and a negative quantity, while the second order non-linear coefficient p' of the mKdV equation is a positive quantity, depending on the plasma parametric values. Therefore, there exists both compressive and rarefactive KdV solitons in the present plasma system.

3. The change in the soliton types from compressive to rarefactive is predicting mainly through the variation of positron beam to ion density ratio parameter ν, depending on σ and σ_b. It is seen that compressive and rarefactive solitons are to exist for the range of $\nu \leq 0.1793$ and $\nu > 0.1793$ respectively.

4. At the critical ν_c, we consider a second order nonlinearity and determine mKdV equation. Only compressive ion acoustic solitary wave structures are feasible in present plasma system.

ORCID

 Rafia Khanam, https://orcid.org/0009-0006-8648-0827; **Satyendra Nath Barman**, https://orcid.org/0000-0003-1136-8364

REFERENCES

[1] B.Boro, A.N. Dev, B.K. Saikia, and N.C. Adhikary, "Nonlinear wave interaction with positron beam in a relativistic plasma: evaluation of hypersonic dust ion acoustic waves," Plasma Physics Reports, **46**(6), 641-652 (2020). https://doi.org/10.1134/S1063780X20060021

[2] S.A.El-Tantawy, M.H. Alshehri, F.Z. Duraihem, and L.S. El-Sherif, "Dark soliton collisions and method of lines approach for modeling freak waves in a positron beam plasma having superthermal electrons," Results in Physics, **19**, 103452 (2020). https://doi.org/10.1016/j.rinp.2020.103452

[3] A.R. Esfandyari, S. Khorram, and A. Rostami, "Ion-acoustic solitons in a plasma with a relativistic electron beam," Physics of Plasmas, **8(11)**, 4753-4761 (2001). https://doi.org/10.1063/1.1399326

[4] M. Vranic, O. Klimo, G. Korn, and S. Weber, "Multi-GeV electron-positron beam generation from laser-electron scattering," Scientific reports, **8**(1), 4702 (2018). https://doi.org/10.1038/s41598-018-23126-7

[5] J. Warwick, T. Dzelzainis, M.E. Dieckmann, W. Schumaker, D. Doria, L. Romagnani, K. Poder, *et al.*, "Experimental observation of a current-driven instability in a neutral electron-positron beam," Physical review letters, **119**(18), 185002 (2017). https://doi.org/10.1103/PhysRevLett.119.185002

[6] S. Ali Shan, A. Ur-Rehman, and A. Mushtaq, "Ion-acoustic solitary waves in a positron beam plasma with electron trapping and nonextensivity effects," Physics of Plasmas, **24**(3), 032104 (2017). https://doi.org/10.1063/1.4978294

[7] R. Khanam, and S.N. Barman, "The Formation of Ion-Acoustic Solitary Waves in a Plasma Having Nonextensive Electrons and Positrons," East European Journal of Physics, (4), 518-525 (2024). https://doi.org/10.26565/2312-4334-2024-4-61

[8] G. Sarri, M.E. Dieckmann, I. Kourakis, A. Di Piazza, B. Reville, C.H. Keitel, and M. Zepf, "Overview of laser-driven generation of electron–positron beams", Journal of Plasma Physics, **81**(4), 455810401 (2015). https://doi.org/10.1017/S002237781500046X

[9] B.C. Kalita, M.K. Kalita, and R.P. Bhatta, "Solitons in a magnetized ion-beam plasma system," Journal of plasma physics, **50**(3), 349-357 (1993). https://doi.org/10.1017/S0022377800017190

[10] M. Khalid, A. Ullah, A. Kabir, H. Khan, M. Irshad, and S.M. Shah, "Oblique propagation of ion-acoustic solitary waves in magnetized electron-positron-ion plasma with Cairns distribution," Europhysics Letters, **138**(6), 63001 (2022). https://doi.org/10.1209/0295-5075/ac765c

[11] M.K. Deka, and A.N. Dev, "Wave propagation with degenerate electron–positron in magnetically quantised ion beam plasma," Pramana, **95**(2), 65 (2021). https://doi.org/10.1007/s12043-021-02081-5

[12] G. Sarri, K. Poder, J.M. Cole, W. Schumaker, A. Di Piazza, B. Reville, T. Dzelzainis, *et al.*, "Generation of neutral and high-density electron–positron pair plasmas in the laboratory," Nature communications, **6**(1), 6747 (2015). https://doi.org/10.1038/ncomms7747

[13] Y.N. Nejoh, "Positron-acoustic waves in an electron–positron plasma with an electron beam," Australian journal of physics, **49**(5), 967-976 (1996). https://doi.org/10.1071/PH960967

[14] B.C. Kalita, R. Das, and H.K. Sarmah, "Weakly relativistic solitons in a magnetized ion-beam plasma in presence of electron inertia," Physics of Plasmas, **18**(1), 012304 (2011). https://doi.org/10.1063/1.3536428

[15] E.F. El-Shamy, W.F. El-Taibany, E.K. El-Shewy, and K.H. El-Shorbagy, "Positron acoustic solitary waves interaction in a four-component space plasma," Astrophysics and Space Science, **338**, 279-285 (2012). https://doi.org/10.1007/s10509-011-0930-4

[16] E. Saberian, A. Esfandyari-Kalejahi, and M. Akbari-Moghanjoughi, "Propagation of ion-acoustic solitary waves in a relativistic electron-positron-ion plasma," Canadian Journal of Physics, **89**(3), 299-309 (2011). https://doi.org/10.1139/P11-024

[17] H.A. Alyousef, S.N. Naeem, M. Irshad, A.U.R. Ata-ur-Rahman, S.M. Ismaeel, and S.A. El-Tantawy, "On the dynamics of large-amplitude ion-acoustic waves in a non-Maxwellian plasma with nonthermal electrons and an electron beam," Physics of Fluids, **36**(3), 035151 (2024). https://doi.org/10.1063/5.0189713

[18] K. Javidan, and D. Saadatmand, "Effect of high relativistic ions on ion acoustic solitons in electron-ion-positron plasmas with nonthermal electrons and thermal positrons," Astrophysics and Space Science, **333**, 471-475 (2011). https://doi.org/10.1007/s10509-011-0645-6

[19] E.I. El-Awady, S.A. El-Tantawy, W.M. Moslem, and P.K. Shukla, "Electron–positron–ion plasma with kappa distribution: Ion acoustic soliton propagation," Physics Letters A, **374**(31-32), 3216-3219 (2010). https://doi.org/10.1016/j.physleta.2010.05.053

[20] N.S. Saini, and I. Kourakis, "Electron beam–plasma interaction and ion-acoustic solitary waves in plasmas with a superthermal electron component," Plasma Physics and Controlled Fusion, **52**(7), 075009 (2010). https://doi.org/10.1088/0741-3335/52/7/075009

[21] A. Esfandyari-Kalejahi, M. Mehdipoor, and M. Akbari-Moghanjoughi, "Effects of positron density and temperature on ion-acoustic solitary waves in a magnetized electron-positron-ion plasma: Oblique propagation," Physics of Plasmas, **16**(5), 052309 (2009). https://doi.org/10.1063/1.3142465

[22] J.N. Han, S.C. Li, X.X. Yang, and W.S. Duan, "Head-on collision of ion-acoustic solitary waves in an unmagnetized electron-positron-ion plasma," The European Physical Journal D, **47**, 197-201 (2008). https://doi.org/10.1140/epjd/e2008-00033-3

[23] R.G. Greaves, and C.M. Surko, "An electron-positron beam-plasma experiment," Physical review letters, **75**(21), 3846 (1995). https://doi.org/10.1103/PhysRevLett.75.3846

[24] P.G.Coleman, Positron beams and their applications, *World Scientific*, 9789810233945, 9810233949 (2000).

[25] R. Sarma, A.P. Misra, and N.C. Adhikary, "Nonlinear ion-acoustic solitary waves in an electron-positron-ion plasma with relativistic positron beam," Chinese Physics B, **27**(10), 105207 (2018). 10.1088/1674-1056/27/10/105207

[26] P.J. Schultz, and K.G. Lynn, "Interaction of positron beams with surfaces, thin films, and interfaces," Reviews of Modern Physics, **60**(3), 701 (1988). https://doi.org/10.1103/RevModPhys.60.701

[27] S. Ali Shan, S.A. El-Tantawy, and W.M. Moslem, "On the fully nonlinear acoustic waves in a plasma with positrons beam impact and superthermal electrons," Physics of Plasmas, **20**(8), 082104 (2013). https://doi.org/10.1063/1.4817280

[28] A. Shah, S. Mahmood, and Q. Haque, "Ion acoustic shock waves in presence of superthermal electrons and interaction of classical positron beam," Physics of Plasmas, **19**(3), 032302 (2012). https://doi.org/10.1063/1.3684659

[29] A. Shah, Q. Haque, and S. Mahmood, "Astrophysical naturally moderated classical positron beam interaction with nonlinear waves in nonextensive astrophysical plasmas," Astrophysics and Space Science, **344**, 119-126 (2013). https://doi.org/10.1007/s10509-012-1305-1

[30] M.J. Hogan, "Electron and positron beam–driven plasma acceleration," Reviews of Accelerator Science and Technology, **9**, 63-83 (2016). https://doi.org/10.1142/S1793626816300036

[31] S.N. Barman, and K. Talukdar, "Nonlinear Ion-Acoustic Solitary Waves in a Weakly Relativistic Electron-Positron-Ion Plasma with Relativistic Electron and Positron Beams," East European Journal of Physics, (4), 79-85 (2024). https://doi.org/

[32] A. Roy, T. Sarkar, S. Roy, and S. Raut, "Impact of relativistic positron beam on ion-acoustic solitary, periodic and breather waves in Earths' ionospheric region through the framework of KdV and modified KdV equation," Physica Scripta, 99(12), 125603 (2024). https://doi.org/10.1088/1402-4896/ad8d36

[33] A. Rényi, "On a new axiomatic theory of probability," Acta Mathematica Academiae Scientiarum Hungaricae, **6**, 285–335 (1955). https://doi.org/10.1007/BF02024393

[34] C. Tsallis, "Possible generalization of Boltzmann-Gibbs statistics," Journal of Statistical Physics, **52**, 479–487 (1988). https://doi.org/10.1007/BF01016429

[35] C. Tsallis, and L.J. Cirto, "Black hole thermodynamical entropy," The European Physical Journal C, **73**, 2487 (2013). https://doi.org/10.1140/epjc/s10052-013-2487-6

[36] G. Kaniadakis, "Non-linear kinetics underlying generalized statistics," Journal of Physics A: Mathematical and Theoretical, **296**, 405–425 (2001). https://doi.org/10.1016/S0378-4371(01)00184-4

[37] G. Kaniadakis, "Statistical mechanics in the context of special relativity," Physical Review E, **66**, 056125 (2002). https://doi.org/10.1103/PhysRevE.66.056125

[38] A.M. Teweldeberhan, H.G. Miller, R. Tegen, "k-deformed statistics and the formation of a quark-gluon plasma," International Journal of Modern Physics E, **12**, 669–673 (2003). https://doi.org/10.1142/S021830130300148X

[39] A. Rossani, and A.M. Scarfone, "Generalized kinetic equations for a system of interacting atoms and photons: theory and simulations," Journal of Physics A: Mathematical and Theoretical, **37**, 4955 (2004). https://doi.org/10.1088/0305-4470/37/18/004

[40] T.S. Biro, and G. Kaniadakis, "Two generalizations of the Boltzmann equation," European Physical Journal B, **50**, 3–6 (2006). https://doi.org/10.1140/epjb/e2006-00112-3

[41] K. Ourabah, A.H. Hamici-Bendimerad, and M. Tribeche, "Quantum entanglement and Kaniadakis entropy," Physica Scripta, **90**, 045101 (2015). https://doi.org/10.1088/0031-8949/90/4/045101

[42] K. Ourabah, and M. Tribeche, "Planck radiation law and Einstein coefficients reexamined in Kaniadakis k-statistics," Physical Review E, **89**, 062130 (2014). https://doi.org/10.1103/PhysRevE.89.062130

[43] J. Kalita, R. Das, K. Hosseini, S. Salahshour, and D. Baleanu: "Some Models in Unmagnetized Plasma involving Kaniadakis Distributed Electrons and Temperature Ratio: Dust Ion Acoustic Solitary Waves," Journal of Applied and Computational Mechanics, **10**(4), 792-800 (2024). https://doi.org/10.22055/jacm.2024.46197.4476

[44] M. Khalid, A. Khan, M. Khan, and F. Hadi, "Dust Ion Acoustic Solitary Waves in Unmagnetized Plasma with Kaniadakis Distributed Electrons," Brazilian Journal of Physics, **51**, 60-65 (2021). https://doi.org/10.1007/s13538-020-00807-1

[45] M. Das, and R. Das, "High Relativistic Impact on Dust-Ion-Acoustic Solitary Waves in Unmagnetised Plasma with Kaniadakis Distributed Electrons," Brazilian Journal of Physics, **54**, 161 (2024). https://doi.org/10.1007/s13538-024-01532-9

[46] S. Raut, K.K. Mondal, P. Chatterjee, and S. Roy, "Dust ion acoustic bi-soliton, soliton, and shock waves in unmagnetized plasma with Kaniadakis-distributed electrons in planar and nonplanar geometry," The European Physical Journal D, **77**, 100 (2023). https://doi.org/10.1140/epjd/s10053-023-00676-8

[47] I. Lourek, and M. Tribeche, "On the role of the k-deformed Kaniadakis distribution in nonlinear plasma waves," Physica A: Statistical Mechanics and its Applications, **441**, 215–220 (2016). https://doi.org/10.1016/j.physa.2015.08.055

[48] M. Irshad, A.R. Ata-ur-Rahman, M. Khalid, S. Khan, B.M. Alotaibi, S.A. El-Sherif, and S.A. El-Tantawy, "Effect of k-deformed Kaniadakis distribution on the modulational instability of electron-acoustic waves in a non-Maxwellian plasma," Physics of Fluids, **35**, 105116 (2023). https://doi.org/10.1063/5.0171327

KdV ТА mKdV ІОННО-АКУСТИЧНІ ПООДИНОКІ ХВИЛІ В ПОЗИТРОННО-ПУЧКОВІЙ ПЛАЗМІ З РОЗПОДІЛЕНИМИ ЕЛЕКТРОНАМИ КАНІАДАКІСА

Рафія Ханам[a], **Сатьендра Натх Барман**[b]

[a]Факультет математики, Університет Гаухаті, Гувахаті-781014, Ассам, Індія
[b]Коледж Б. Бороа, Гувахаті-781007, Ассам, Індія

Проведено теоретичні та чисельні дослідження іонно-акустичних поодиноких хвиль (IAX) у ненамагніченній плазмі з іонами, пучками позитронів при зміні тиску та розподіленими електронами Каніадакіса. Потенційна амплітуда хвилі розраховується шляхом застосування підходу редуктивного збурення для зведення контрольного набору нормалізованих рівнянь рідини до рівнянь Кортевега-де Фріза (KdV) і модифікованих рівнянь Кортевега-де Фріза (mKdV). У mKdV рішеннях зустрічаються лише солітони стиснення, тоді як Встановлено, що для різних значень σ, σ_b і ν існують як стискаючі, так і розріджені солітони KdV. Параметр k також не впливає на IASW рівняння KdV, але має внесок у солітонах mKdV. Також показано, що включення нетеплових електронів різко змінює основні властивості іонно-акустичних солітонів і створює новий параметричний режим.

Ключові слова: *іонно-акустичні одиночні хвилі; позитронні пучки; рівняння KdV; рівняння mKdV; розподіл Каніадакіса*

ION-ACOUSTIC SOLITARY WAVES IN AN UNMAGNETISED DUSTY PLASMA HAVING INERTIALESS ELECTRONS WITH QUANTUM EFFECTS

Satyendra Nath Barman[a], Kingkar Talukdar[b]*

[a]B. Borooah College, Guwahati 781007, Assam, India
[b]Department of Mathematics, Gauhati University, Guwahati 781014, Assam, India
*Corresponding Author e-mail: kingkartalukdar5@gmail.com
Received February 2, 2025; revised February 17, 2025; accepted March 20, 2025

This investigation illustrates the presence and characteristics of compressive and rarefactive solitons in an unmagnetized plasma that includes positive ions, negatively charged dust, inertialess electrons with quantum effect and nonextensively distributed electrons and positrons. For this unmagnetized dusty plasma with positive ions, negatively charged dust, inertialess electrons with quantum effect and nonextensively distributed electrons and positrons, the Korteweg-de Vries (KdV) equation is derived and thus existence and behaviour of compressive and rarefactive soliton is examined. The fluid equations of motion governing the one-dimensional plasma serve as the foundation for the analysis. Using different relational forms of the strength parameter (ε) to stretch the space and time variables results in different nonlinearities. When discussing the effects on soliton amplitude, nonlinearity, and dispersion, various plasma parameters have been considered.

Keywords: *Soliton; q-nonextensive distribution; Reductive perturbation method; KdV equation*
PACS: 52.35.Sb, 52.35.Fp, 52.35.Qz, 52.27.Ep

1. INTRODUCTION

Since electron-positron-ion plasma has so many uses and can be used to observe a variety of astrophysical environments, including the Milky Way galaxy's centre [1], and the production of hard thermal photons with relativistic heavy ion collisions in quark-gluon plasmas [2], it is one of the most crucial areas for researchers to study. Novel statistical techniques like q-nonextensive statistics or Tsallis statistics are gaining popularity. Tsallis statistics yields a power law distribution for all values of q, while the Maxwellian distribution is only obtained for q = 1 [3]. Saini and Shalini have investigated the ion acoustic solitons in a nonextensive plasma with multi-temperature electrons [4]. Shahmansouri and Alinejad [5] discussed two dust ion-acoustic (DIA) solitary wave modes based on population and electron superthermality. When charged dust grains are present in a plasma, the existing plasma wave spectra undergo modifications [6] and several new modes are introduced, such as the dust-acoustic mode [7–8], the dust ion-acoustic mode [9–10], the dust lattice mode [11], etc. Das [12] investigated the combination of the immobile dust charge and relativistic electrons and ion streaming speeds to produce dust-ion acoustic compressive and rarefactive relativistic solitons in a multispecies plasma model for immobile dusty plasma. In astrophysical environments, compact astrophysical objects and the interiors of planets both contain quantum plasmas [13]. In laboratories, quantum plasmas are observed in semiconductors and micromechanical systems [14], in next-generation intense laser–solid density plasma interaction experiments, and in quantum x-ray free-electron lasers [15]. The first study of the quantum counterpart of ion-acoustic waves was conducted by Haas, Garcia, Goedert and Manfredi [16]. They determine a dimensionless parameter that measures the quantum diffraction effects, beginning with the quantum hydrodynamical model. It is demonstrated that the characteristics of solitary waves are significantly impacted by quantum effects [16,17]. Chabrier, Douchin and Potekhin [18] examined the properties of dense plasmas characteristic of the atmospheres of neutron stars and of the interior of massive white dwarfs. Masood [19] used renormalization scheme of quantum electrodynamics (QED) at high temperatures to calculate the effective parameters of relativistic plasma in the early universe. Hasnan, Biswas, Habib, and Sultana [20] have investigated different dust ion acoustic wave modes theoretically and numerically, taking into account a four-component magnetised collisional k-nonthermal plasma that comprises non-inertial k-distributed super thermal electrons, inertial ion fluid, and stationary dust grains of opposite charges. Compressive and rarefactive solitons are demonstrated to exist in a plasma model that includes unmagnetized weak-relativistic positive ions, negative ions, electrons, electron beam and positron beam by Barman and Talukdar [21]. However, in this paper we try to investigate properties of compressive and rarefactive solitons in a non-relativistic plasma model. The reflection of a dust acoustic solitary wave from a potential barrier in a dusty plasma medium was observed experimentally by Kumar, Bandyopadhyay, Singh, Arora and Sen[22], in which experiments were conducted in a DC glow discharge plasma environment using an inverted Π-shaped dusty plasma experimental (DPEx) device. In the presence of Gaussian-shaped and solitary-pulse-type external forces, the damped forced Korteweg–de Vries equation is obtained using the reductive perturbation technique in a dusty plasma with non-thermally distributed electrons by A.Paul, N. Paul, Mondal and Chatterjee [23]. Using the quantum hydrodynamic model, the dynamics of ion-acoustic solitary waves (IASWs) in an unmagnetized, highly relativistic quantum plasma with positive and negative ions and electrons is investigated by Madhukalya, Das, Hosseini, Hincal, Osman and Wazwaz [24].

The treatment takes into consideration that electrons are inertialess, which explains the inertial properties of both positive and negative ions. They have derived Korteweg–de Vries equation using the reductive perturbation method to examine the nonlinear nature of quantum IASWs. The objective of our research is to investigate the presence of solitary plasma waves and their behaviour in a multicomponent plasma model and observe the effects of various parameters on the amplitude, nonlinearity and dispersion of solitons.

In this study, we theoretically investigate the characteristics of nonlinear ion-acoustic solitary waves in a multicomponent plasma composed of positive ions, negatively charged dust, inertialess electrons with quantum effect and nonextensively distributed electrons and positrons. This study examines nonlinear ion-acoustic waves using the reductive perturbation approach. The format of the paper is as follows: The introduction is given in Section (1), followed by the Equations Governing Dynamics of Plasma in Section (2), the KdV equation and its solution in Section (3), Results and Discussions in Section (4) and Conclusions in Section (5).

2. EQUATIONS GOVERNING DYNAMICS OF PLASMA
The fluid equations of motion, governing the collision less dusty plasma in one dimension are:

For positive ion,

$$\frac{\partial n_i}{\partial t} + \frac{\partial (n_i v_i)}{\partial x} = 0, \tag{1}$$

$$\frac{\partial v_i}{\partial t} + v_i \frac{\partial v_i}{\partial x} + \frac{\partial \phi}{\partial x} = 0 \tag{2}$$

For negatively charged dust,

$$\frac{\partial n_d}{\partial t} + \frac{\partial (n_d v_d)}{\partial x} = 0 \tag{3}$$

$$\frac{\partial v_d}{\partial t} + v_d \frac{\partial v_d}{\partial x} - \frac{\partial \phi}{\partial x} = 0. \tag{4}$$

For inertialess electrons with quantum effect,

$$0 = \frac{\partial \phi}{\partial x} - B n_{eq} \frac{\partial n_{eq}}{\partial x} + \frac{1}{2} H_e^2 \frac{\partial}{\partial x} \left(\frac{1}{n_{eq}^{\frac{1}{2}}} \frac{\partial^2 (n_{eq}^{\frac{1}{2}})}{\partial x^2} \right), \tag{5}$$

where, $B = \frac{V_{Fe}^2 \alpha m_e}{c_s^2 r^2 m_i} = \frac{V_{Fe}^2 Q_d}{c_d^2 r^2}$, $H_e^2 = \frac{\hbar \omega_{Pd}}{Z_d k T_i Q_d}$,
where $Q_d = \frac{m_e}{m_d}$.

$$n_e = \delta_e [1 + (q-1)\phi]^{\frac{q+1}{2(q-1)}}, \tag{6}$$

$$n_p = \delta_p [1 - \sigma_F (q-1)\phi]^{\frac{q+1}{2(q-1)}}, \tag{7}$$

where $\delta_e = \frac{1}{1-p}$, $\delta_p = \frac{p}{1-p}$.

Here, H_e is the quantum diffraction term (which is proportional to the ratio of plasma energy to fermi energy), V_{Fe} is the fermi speed, p is the unperturbed positron-to-electron density ratio, σ_F is the electron-to-positron temperature ratio, and parameter q is the real number greater than -1 and represents the strength of the nonextensive ion.

The extensivity limits q < 1, q > 1, and q →1 represents the cases of superthermality, subthermality, and Maxwell-Boltzmann distribution function, respectively. It is possible to expand the normalised nonextensive electron and positron densities of Eqs. (6) and (7), respectively, as

$$n_e = \frac{1}{1-p} \left[1 + \frac{q+1}{2}\phi + \frac{(q+1)(3-q)}{8}\phi^2 + \cdots \right]$$

$$n_p = \frac{p}{1-p} \left[1 - \frac{q+1}{2}\sigma_F \phi + \frac{(q+1)(3-q)}{8}\sigma_F^2 \phi^2 - \cdots \right]$$

The continuity and momentum equations of the plasma's acoustic mode are the fundamental governing equations. The following Poisson equation for the charge imbalances should be added to these equations.

$$\frac{\partial^2 \phi}{\partial x^2} = n_{eq} + n_e - n_i - n_p + Z_d n_d \tag{8}$$

Here, suffixes *i, p, e, eq* and *d* stand for positive ion, nonextensive positron, nonextensive electron, quantum electron and dust respectively.

3. KdV EQUATION AND ITS SOLUTION
We use the stretched variables,

$$\xi = \varepsilon^{\frac{1}{2}}(x - Vt) \text{ and } \tau = \varepsilon^{\frac{3}{2}}t, \tag{9}$$

(where V is the phase velocity) along with the expansions of the flow variables in terms of the smallness parameter ε as $n_i = n_{i0} + \varepsilon n_{i1} + \varepsilon^2 n_{i2} + \varepsilon^3 n_{i3} + \ldots$, $n_p = 1 + \varepsilon n_{p1} + \varepsilon^2 n_{p2} + \varepsilon^3 n_{p3} + \ldots$, $n_e = 1 + \varepsilon n_{e1} + \varepsilon^2 n_{e2} + \varepsilon^3 n_{e3} + \ldots$, $n_{eq} = n_{eq0} + \varepsilon n_{eq1} + \varepsilon^2 n_{eq2} + \varepsilon^3 n_{eq3} + \ldots$, $n_d = n_{d0} + \varepsilon n_{d1} + \varepsilon^2 n_{d2} + \varepsilon^3 n_{d3} + \ldots$, $v_i = v_{i0} + \varepsilon v_{i1} + \varepsilon^2 v_{i2} + \varepsilon^3 v_{i3} + \ldots$, $v_d = v_{d0} + \varepsilon v_{d1} + \varepsilon^2 v_{d2} + \varepsilon^3 v_{d3} + \ldots$, $\phi = \varepsilon \phi_1 + \varepsilon^2 \phi_2 + \varepsilon^3 \phi_3 + \ldots$, to derive the KdV equation from the set of equations (1) to (8).

Using the transformation (9) and the expansions of $n_i, n_p, n_e, n_d, n_{eq}, v_i$ and v_d in equations (1) to (8) and equating the coefficient of the first lowest-order of ε we get,

$$n_{d1} = -\frac{n_{d0}}{(v_{d0}-V)^2}\phi_1, \quad v_{d1} = \frac{1}{v_{d0}-V}\phi_1, \quad n_{eq1} = -\frac{1}{Bn_{eq0}}\phi_1, \quad n_{e1} = \mu_e \frac{(1+q)}{2}\phi_1,$$

$$n_{i1} = \frac{n_{i0}}{(V-v_{i0})^2}\phi_1, \quad v_{i1} = \frac{1}{V-v_{i0}}\phi_1, \quad n_{p1} = -\mu_p \sigma_F \frac{(1+q)}{2}\phi_1,$$

where v_{i0} and v_{d0} are initial streaming velocities of positive ions and dust grains respectively.

Using the expansions of $n_{i1}, n_{p1}, n_{e1}, n_{eq1}$ and n_{d1} in $n_{e1} + n_{eq1} + Z_d n_{d1} - n_{p1} - n_{i1} = 0$, the expression of phase velocity V is found as,

$$-\frac{n_{i0}}{(V-v_{i0})^2} + \mu_e \frac{(1+q)}{2} + \mu_p \sigma_F \frac{(1+q)}{2} - \frac{1}{Bn_{eq0}} - \frac{Z_d n_{d0}}{(v_{d0}-V)^2} = 0$$

Eliminating v_{i2} and v_{d2} from the equations obtained by equating the coefficient of second higher order terms of ε we get the KdV equation as,

$$\frac{\partial \phi_1}{\partial \tau} + P\,\phi_1 \frac{\partial \phi_1}{\partial \xi} + Q \frac{\partial^3 \phi_1}{\partial \xi^3} = 0, \tag{10}$$

where,

$$P = \frac{\left[\frac{2n_{i0}}{(V-v_{i0})^4} - \frac{(q+1)(3-q)(\mu_e - \mu_p \sigma_F{}^2)}{4} + \frac{n_{i0}}{(V-v_{i0})^4} - \frac{3Z_d n_{d0}}{(v_{d0}-V)^4} + \frac{B}{B^3 n_{eq0}{}^3}\right]}{\left[\frac{2n_{i0}v}{(V-v_{i0})^3} - \frac{2Vn_{d0}Z_d}{(v_{d0}-V)^3}\right]}$$

$$Q = \frac{\left[1 - \frac{H_e{}^2}{4B^2 n_{eq0}{}^3}\right]}{\left[\frac{2n_{i0}V}{(V-v_{i0})^3} - \frac{2Vn_{d0}Z_d}{(v_{d0}-V)^3}\right]}$$

We introduce the variable $\eta = \xi - U\tau$, where U is the velocity of the wave in the linear η space, to find a stationary solution of the KdV equation (10). Equation (10) can be integrated using the boundary conditions $\phi_1 = \frac{\partial \phi_1}{\partial \eta} = \frac{\partial^2 \phi_1}{\partial \eta^2} = 0$ as $|\eta| \to \infty$, to give

$$\phi_1 = \phi_0 \text{sech}^2(\eta/\Delta) \tag{11}$$

where $\phi_0 = (3U/P)$ is the amplitude and $\Delta = (4Q/U)^{1/2}$ is the width of the soliton respectively.

4. RESULTS AND DISCUSSIONS

We have obtained KdV equation from the set of governing equations [1-7] and the Poisson equation [8]. Since the existence and characteristics of solitary waves are explained by the KdV equation, we have computationally investigated the existence and characteristics of our multicomponent plasma model for a variety of parameters. In this manuscript we have considered some standard ranges for plasma parameters. The value of B= 18000000, which is because of high fermi speed (V_{Fe}). Analysing the variation of soliton amplitude with respect to q (Figure 1), we observe the presence of compressive solitons for some fixed parameters $H_e=5$, B=18000000, U=0.6, $n_{eq0}=1$, $n_{i0}=0.8$, $v_{i0}=1.3$, $\delta_e=0.38$, $\delta_p=0.21$, $\sigma_F=0.088$, $Z_d=3$, $n_{d0}=0.7$, $V_{d0}=1.0$. As q increases from 0 to 0.8, the solitary wave amplitude increases gradually. On describing the variation of soliton amplitude with respect to q while keeping the remaining parameters fixed and changing the value δ_e, we can observe the presence of comparatively higher amplitude KdV compressive solitons for higher values of δ_e. Also, analysing the variation of soliton amplitude with respect to V_{i0} (Figure 2), we observe that as V_{i0} increases the amplitude of rarefactive soliton decreases gradually. Keeping the remaining parameters fixed as $H_e=5$, B=18000000, U=0.01, $n_{eq0}=0.8$, $n_{i0}=1.3$, $\delta_e=0.26$, $n_{i0}=1.3$, q=0.216, $\delta_e=0.26$, $\mu_p=0.26$, $\sigma_F=0.01$, $Z_d=2$, $n_{d0}=1$, $V_{d0}=0.8$ and analysing the variation of rarefactive soliton amplitude for comparative higher values of q, we observe that as q increases from 0.026 to 0.216, the amplitude of rarefactive soliton decreases.

Analysing the variation of soliton amplitude with respect to σ_F (Figure 3) we observe the presence of compressive solitons for some fixed parameters $H_e=4$, B=18000000, U=0.1, $n_{eq0}=0.8$, $n_{i0}=1$, $v_{i0}=1$, $\delta_e=0.16$, $\delta_p=0.8$, q=0.021, $Z_d=1$, $n_{d0}=0.8$. As σ_F increases from 0 to 0.5 the solitary wave amplitude decreases gradually. On describing the variation of soliton amplitude with respect to σ_F while keeping the remaining parameters fixed and changing V_{d0}, we can observe the presence of comparatively higher amplitude KdV compressive solitons for higher value of V_{d0}. Also, analysing the
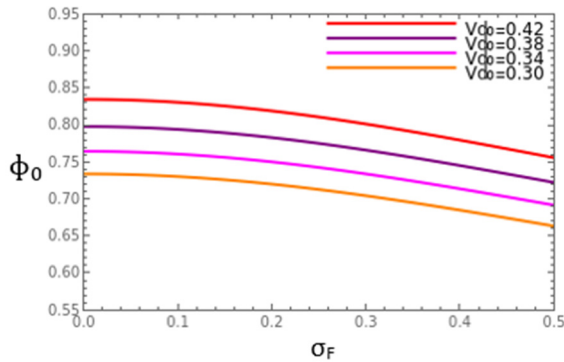
variation of soliton amplitude with respect to V_{d0} (Figure 4), we observe that as V_{d0} increases the rarefactive soliton amplitude decreases gradually. Keeping the remaining parameters fixed as $H_e=4$, $B=18000000$, $U=0.01$, $n_{eq0}=1$, $n_{i0}=1$, $V_{i0}=0.8$, $\delta_e=0.26$, $\delta_p=1$, $Z_d=8$, $n_{d0}=0.1$, $\sigma_F=0.028$ and analysing the variation of rarefactive soliton amplitude for different values of q, we observe that as q increases from 0.156 to 0.456, the amplitude of rarefactive soliton decreases.
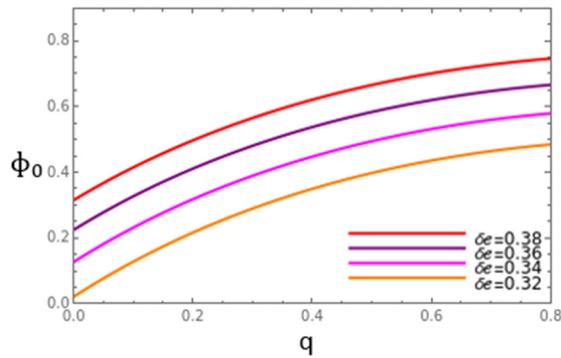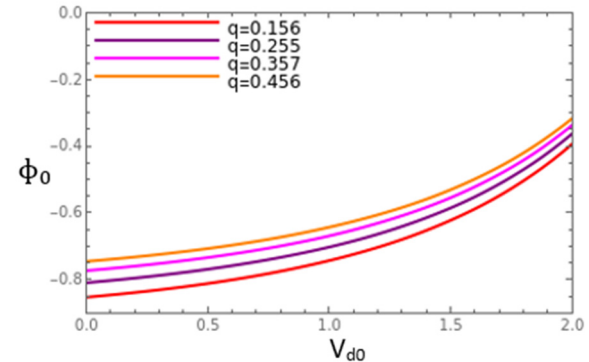

Figure 1. Variation of amplitude with respect to q for different δ_e and fixed $H_e=5$, $B=18000000$, $U=0.6$, $n_{eq0}=1$, $n_{i0}=0.8$, $v_{i0}=1.3$, $\delta_p=0.21$, $\sigma_F=0.088$, $Z_d=3$, $n_{d0}=0.7$, $V_{d0}=1.0$
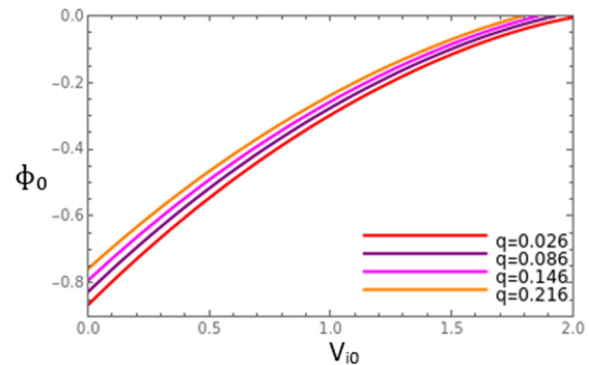
Figure 2. Variation of amplitude with respect to V_{i0} for different q and fixed $H_e=5$, $B=18000000$, $U=0.01$, $n_{eq0}=0.8$, $n_{i0}=1.3$, $\delta_e=0.26$, $\delta_p=0.26$, $\sigma_F=0.01$, $Z_d=2$, $n_{d0}=1$, $V_{d0}=0.8$


Figure 3. Variation of amplitude with respect to σ_F for different V_{d0} and fixed $H_e=4$, $B=18000000$, $U=0.1$, $n_{eq0}=0.8$, $n_{i0}=1$, $v_{i0}=1$, $\delta_e=0.16$, $\delta_p=0.8$, $q=0.021$, $Z_d=1$, $n_{d0}=0.8$


Figure 4. Variation of amplitude with respect to V_{d0} for different q and fixed $H_e=4$, $B=18000000$, $U=0.01$, $n_{eq0}=1$, $n_{i0}=1$, $V_{i0}=0.8$, $\delta_e=0.26$, $\delta_p=1$, $Z_d=8$, $n_{d0}=0.1$, $\sigma_F=0.028$

Analysing the deviation of nonlinear term (P) with respect to q (Figure 5) we observe that nonlinearity decreases as q increases. Checking the effect of nonlinear term with respect to q for fixed $H_e=5$, $B=18000000$, $U=1.3$, $n_{eq0}=1.3$, $n_{i0}=1.8$, $\delta_e=0.32$, $V_{d0}=1$, $\delta_p=0.21$, $Z_d=3$, $n_{d0}=1$, $\sigma_F=0.01$ and changing values of V_{i0}, we observe that for V_{i0} from 1.27 to 1.42 the nonlinearity appears comparatively higher. Also, observing the deviation of nonlinear term with respect to V_{i0} (Figure 6), we see that as V_{i0} increases from 0 to 2 the nonlinearity decreases gradually for $H_e=5$, $B=18000000$, $U=1$, $n_{eq0}=1$, $n_{i0}=2.1$, $\delta_e=0.16$, $V_{d0}=0.8$, $\delta_p=0.26$, $q=0.021$, $n_{d0}=1$, $\sigma_F=0.013$. Checking the variation of Nonlinear term with respect to V_{i0} we observe that the nonlinearity is comparatively lower for greater values of Z_d.
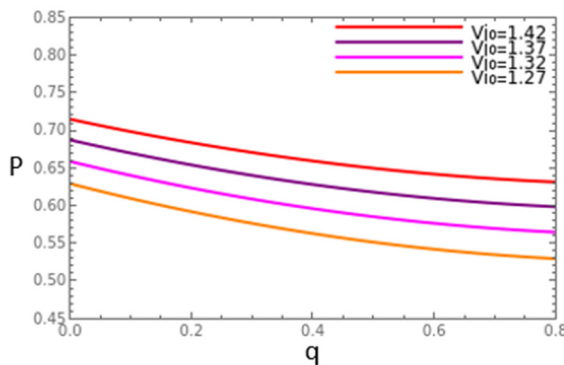
Figure 5. Variation of nonlinearity with respect to q for different v_{i0} and fixed $H_e=5$, $B=18000000$, $U=1.3$, $n_{eq0}=1.3$, $n_{i0}=1.8$, $\delta_e=0.32$, $V_{d0}=1$, $\delta_p=0.21$, $Z_d=3$, $n_{d0}=1$, $\sigma_F=0.01$
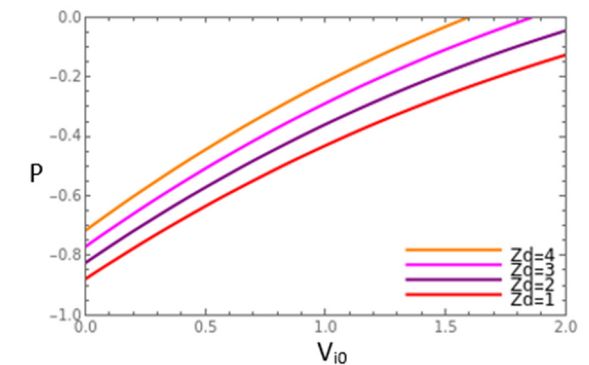
Figure 6. Variation of nonlinearity with respect to V_{i0} for different Z_d and fixed $H_e=5$, $B=18000000$, $U=1$, $n_{eq0}=1$, $n_{i0}=2.1$, $\delta_e=0.16$, $V_{d0}=0.8$, $\delta_p=0.26$, $q=0.021$, $n_{d0}=1$, $\sigma_F=0.013$

As the dispersion term (Q) describes the broadening of solitary wave profile so analysing dispersion with respect to V_{i0} (Figure 7) we observe that Q decreases as V_{i0} increases for $B=18000000$, $n_{eq0}=0.52$, $n_{i0}=2.1$, $Z_d=3$, $n_{d0}=1$, $H_e=4$.

Keeping the remaining parameters fixed, as we observe the variation of Q with respect to V_{i0} we observe that dispersion gets comparatively higher as V_{d0} increases. Also, observing the variation of dispersion with respect to V_{d0} (Figure 8), we observe that dispersion increases as V_{d0} increases. For fixed B=18000000, n_{eq0}=0.52, n_{i0}=2.6, n_{d0}=1.3, H_e=3, V_{i0}=0.32 and different Z_d in the comparison of dispersion with respect to V_{d0}, we observe that dispersion increases as Z_d increases.
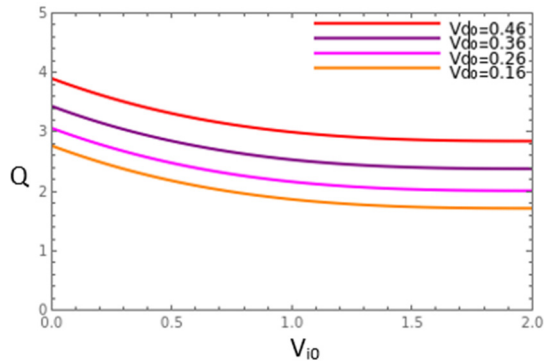

Figure 7. Variation of dispersion with respect to V_{i0} for different v_{d0} and fixed B=18000000, n_{eq0}=0.52, n_{i0}=2.1, Z_d=3, n_{d0}=1, H_e=4
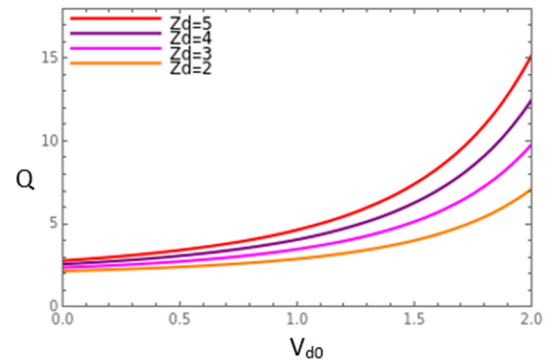
**Figure 8.** Variation of dispersion with respect to V_{d0} for different Z_d and fixed B=18000000, n_{eq0}=0.52, n_{i0}=2.6, n_{d0}=1.3, H_e=3, V_{i0}=0.32

Further, we have observed variation of solitary wave potential φ_1 versus η for four different values of V_{i0} as shown in Figure 9 and for four different values of q as shown in Figure 10. We have found that the wave potential of compressive solitons (Figure 9) is higher for higher values of V_{i0} and that of rarefactive solitons (Figure 10) is lower for higher values of q .
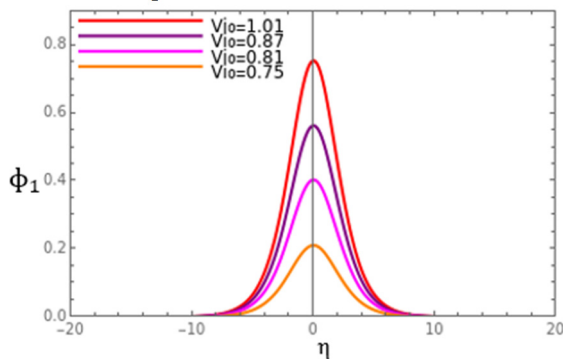
Figure 9. Variation of ϕ_1 with respect to η for different V_{i0} and fixed H_e=5, B=18000000, U=2.4, n_{eq0}=1, n_{i0}=1.7, q=0.015, δ_e=0.26, δ_p=0.32,σ_F=0.01,Z_d=1,n_{d0}=1.6,V_{d0}=1.3
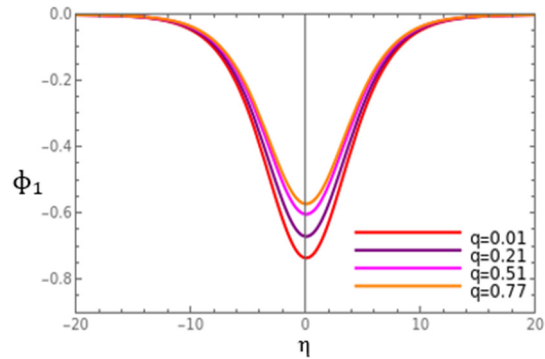
Figure 10. Variation of ϕ_1 with respect to η for different q and fixed H_e=5, B=18000000, U=0.52, n_{eq0}=1, n_{i0}=1.7, δ_e=0.16, δ_p=0.26,σ_F=0.008,Z_d=1,n_{d0}=1.6,V_{i0}=0.5,V_{d0}=1

5. CONCLUSIONS

We have found that both compressive and rarefactive solitons are present in our plasma model that includes positive ions, negatively charged dust, inertialess electrons with quantum effect and nonextensively distributed electrons and positrons. Both the compressive and rarefactive solitons are found to exist in a definite range of parameters such as, $0.21 \leq \delta_p \leq 1$, $0.16 \leq \delta_e \leq 0.38$, $1 \leq Z_d \leq 8$ and for q < 1, which represents the case of superthermality. Also, both the compressive and rarefactive solitons are found to exist for unperturbed density of inertialess electrons with quantum effect $n_{eq0} \leq 1.3$, quantum diffraction term $H_e \leq 5$ (for heavy dust mass $H_e \approx 10$) and B=18000000. Our investigation can be useful for the researcher investigating on plasma in astrophysical environments.

ORCID

 Satyendra Nath Barman, https://orcid.org/0000-0003-1136-8364; **Kingkar Talukdar,** https://orcid.org/0009-0007-5419-134X

REFERENCES

[1]   M.L. Burns, *Positron-Electron Pairs in Astrophysics*, (American Institute of Physics, Melville NY, 1983).

[2]   F.D. Steffen, and M.H. Thoma, "Hard thermal photon production in relativistic heavy ion collisions," Phys. Lett. B, **510**, 98-106 (2001). https://doi.org/10.1016/S0370-2693(01)00525-1

[3]   C. Tsallis, "Possible Generalization of Boltzmann-Gibbs Statistics," Stat. J. Phys. **52**, 479-487 (1988). https://doi.org/10.1007/BF01016429

[4]   N.S. Saini, and Shalini, "Ion acoustic solitons in a nonextensive plasma with multi-temperature electrons," Astrophys. Space Sci. **346**, 155-163 (2013). https://doi.org/10.1007/s10509-013-1431-4

[5]   H. Shahmansouri, and H. Alinejad, "Arbitrary amplitude dust ion acoustic solitary waves in a magnetized suprathermal dusty plasma," Phys. Plasmas, **19**, 123701 (2012). https://doi.org/10.1063/1.4769850

[6]   P.K. Shukla, and L. Stenflo, "Stimulated scattering of electromagnetic waves in dusty plasmas," Astrophys. Space Sci. **190**, 23-32 (1992). https://doi.org/10.1007/BF00644563

[7]   N.N. Rao, P.K. Shukla, and M.Y. Yu, "Dust-acoustic waves in dusty plasmas," Planet. Space Sci. **38**, 543-546 (1990). https://doi.org/10.1016/0032-0633(90)90147-I

[8]   A.A. Mamun, "Arbitrary Amplitude Dust-acoustic Solitary Structures in a three-component Dusty Plasma," Astrophys. Space Sci. **268**, 443-454 (1999). https://doi.org/10.1023/A:1002031022895

[9]   P.K. Shukla, and V.P. Silin, "Dust ion-acoustic wave," Phys. Scr. **45**, 508 (1992). https://doi.org/10.1088/0031-8949/45/5/015

[10] F. Barkan, N. D'Angelo, and R.L. Merlino, "Experiments on ion-acoustic waves in dusty plasmas," Planet. Space Sci. **44**, 239-242 (1996). https://doi.org/10.1016/0032-0633(95)00109-3

[11] A. Homann, A. Melzer, S. Peters and A. Piel, "Determination of the dust screening length by laser-excited lattice waves," Phys. Rev. E, **56**, 7138 (1997). https://doi.org/10.1103/PhysRevE.56.7138

[12] S. Das, "Weak Relativistic Effect in the Formation of Ion-Acoustic Solitary Waves in Dusty Plasma," IEEE Transactions on Plasma Science, **50**, 2225-2229 (2022). https://doi.org/10.1109/TPS.2022.3181149

[13] S.L. Shapiro, and S.L. Teukolsky, *Black Holes, White Dwarfs and Neutron Stars: The Physics of Compact Objects*, (John Wiley and Sons, New York, 1983). http://dx.doi.org/10.1002/9783527617661

[14] P.A. Markowich, C.A. Ringhofer, and C. Schmeiser, *Semiconductor Equations*, (Springer-Verlag Wien 1990). https://doi.org/10.1007/978-3-7091-6961-2

[15] P.K. Shukla, and B. Eliasson, "Nonlinear Interactions between Electromagnetic Waves and Electron Plasma Oscillations in Quantum Plasmas," Phys. Rev. Lett. **99**, 096401 (2007). https://doi.org/10.1103/PhysRevLett.99.096401

[16] F. Haas, L.G. Garcia, J. Goedert, and J. Manfredi, "Quantum ion-acoustic waves," Phys. Plasmas, **10**, 3858-3866 (2003). https://doi.org/10.1063/1.1609446

[17] M. Tribeche, S. Ghebache, K. Aoutou, and T. H. Zerguini, "Arbitrary amplitude quantum dust ion-acoustic solitary waves," Phys. Plasmas 15, 033702 (2008). https://doi.org/10.1063/1.2899325

[18] G. Chabrier, F. Douchin, and A.Y. Potekhin, "Dense astrophysical plasmas," Journal of Physics: Condensed Matter, **14**, 9133 (2002). https://doi.org/10.1088/0953-8984/14/40/307

[19] S.S. Masood, "QED plasma in the early universe," Arabian Journal of Mathematics, **8**, 183-192 (2019). https://doi.org/10.1007/s40065-018-0232-6

[20] M.R. Hassan, S. Biswas, K. Habib, and S. Sultana, "Dust–ion-acoustic waves in a κ-nonthermal magnetized collisional dusty plasma with opposite polarity dust," Results in Physics, **33**, 105106 (2022). https://doi.org/10.1016/j.rinp.2021.105106

[21] S.N. Barman, and K. Talukdar, "Nonlinear Ion-Acoustic Solitary Waves in A Weakly Relativistic Electronpositron-Ion Plasma with Relativistic Electron and Positron Beams," East European Journal of Physics, (4), 79-85 (2024). https://doi.org/10.26565/2312-4334-2024-4-07

[22] K. Kumar, P. Bandyopadhyay, S. Singh, G. Arora and A. Sen, "Reflection of a dust acoustic solitary wave in a dusty plasma," Phys. Plasmas, **28**, 103701 (2021). https://doi.org/10.1063/5.0060747

[23] A. Paul, N. Paul, K.K. Mondal, and P. Chatterjee, "Influences of External Excitations on Solitary Waves in Nonthermal Dusty Plasma," Plasma Physics Reports, **48**, 1013-1022 (2022). https://doi.org/10.1134/S1063780X22100063

[24] B. Madhukalya, R. Das, K. Hosseini, E. Hincal, M.S. Osman and A.M. Wazwaz, "Nonlinear analysis of ion-acoustic solitary waves in an unmagnetized highly relativistic quantum plasma," Heat Transfer, **53**(8), 4036-4051 (2024). https://doi.org/10.1002/htj.23125

ІОННО-АКУСТИЧНІ ОДИНОЧНІ ХВИЛІ В НЕМАГНІТИЗОВАНІЙ ПИЛОВІЙ ПЛАЗМІ З БЕЗІНЕРЦІЙНИМИ ЕЛЕКТРОНАМИ З КВАНТОВИМИ ЕФЕКТАМИ

Сатьендра Натх Барман[a], Кінгкар Талукдар[b]
[a]Б. Буруа коледж, Гаухаті 781007, Ассам, Індія
[b]Департамент математики, Університет Гаухаті, Гувахаті 781014, Ассам, Індія

Це дослідження ілюструє наявність і характеристики стискаючих і розріджених солітонів у ненамагніченій плазмі, яка включає позитивні іони, негативно заряджений пил, безінерційні електрони з квантовим ефектом і нерозподілені електрони та позитрони. Для цієї ненамагніченої пилоподібної плазми з позитивними іонами, негативно зарядженим пилом, безінерційними електронами з квантовим ефектом і нерозповсюдженими електронами та позитронами було виведено рівняння Кортевега-де Фріза (KdV), і таким чином досліджено існування та поведінку стисливого та розрідженого солітону. Основою для аналізу є рівняння руху рідини, що керують одновимірною плазмою. Використання різних реляційних форм параметра сили (ε) для розтягування просторових і часових змінних призводить до різних нелінійностей. При обговоренні впливу на амплітуду, нелінійність і дисперсію солітонів розглядалися різні параметри плазми.

Ключові слова: *солітон; q-нееекстенсивний розподіл; редуктивний метод збурень; рівняння KdV*

COMPARISON OF CORE AND NO-CORE SHELL MODELS IN EXCITATION OF NEGATIVE PARITY STATES OF $^{19}_9F$

Berun N. Ghafoor^{a,c*}, Aziz H. Fatah$^{b\#}$, Ari K. Ahmed^{a§}

^{a}University of Sulaimani, College of Education, Physics department, Iraq
^{b}University of Sulaimani, College of Science, Physics department, Iraq
^{c}Research and Development Center, University of Sulaimani, Iraq
Corresponding Author e-mail: berun.ghafoor@univsul.edu.iq; $^\#$aziz.fatah@univsul.edu.iq; §ari.ahmed@univsul.edu.iq

The present study investigates the nuclear structure of low-lying negative parity states in $^{19}_9F$ using a combination of the shell model and Hartree-Fock (HF) approaches. A comprehensive analysis of nuclear properties—including energy spectra, electron scattering form factors, transition strengths, binding energies, and charge radii—was performed within four model spaces: the $sdpf$-model space, the zbm-model space, the psd-model space, and the extended $spsdpf$ no-core shell model space. Various effective interactions were applied within each model space to assess their impact on nuclear behavior. The HF method, utilizing multiple Skyrme parameterizations, along with harmonic oscillator and Woods-Saxon potentials, was employed to compute single-particle radial wave functions essential for matrix element calculations. The results demonstrate that Skyrme-based HF calculations, when integrated with shell model techniques, effectively capture fundamental nuclear properties. A systematic comparison with experimental data reveals that transitioning from core-restricted model spaces to a fully no-core framework significantly improves the reproduction of electron scattering form factors, particularly in both longitudinal (C1, C3) and transverse (E1, M2) components. Notably, specific states exhibit optimal agreement at different core levels: the $3/2^-_1$ and $5/2^-_1$ states are best reproduced in the no-core shell model, while the $7/2^-_1$ state achieves high accuracy within the zbm and psd model spaces. Overall, this research underscores the critical influence of model space selection and interaction choice in theoretical nuclear studies. The progressive refinement from core-based to no-core calculations highlights the role of many-body correlations in nuclear excitations and provides deeper insight into the intrinsic structure of $^{19}_9F$, contributing to advancements in nuclear structure theory and reaction dynamics.

Keywords: *Nuclear Structure; Model Spaces; Core-to-no-Core; Skyrme-HF; Fluorine-19*
PACS: 21.60.Cs, 21.60.Jz, 25.30.Bf, 21.10.-k, 27.20.+n

1. INTRODUCTION

Electron scattering, which involves the interaction of electrons with the nucleus via electromagnetic forces, is an important tool for studying nuclear structure, providing vital experimental data for testing theoretical models [1]. Its efficiency stems from the well-established electromagnetic interaction, which is properly characterized by quantum electrodynamics, as well as the interaction's relative weakness.

In this work, elastic and inelastic scattering form factors were estimated using the shell model and Hartree-Fock theory to produce single-particle states. The Hartree-Fock technique, a variational approach, generates the wave function of many-body quantum systems by modeling fermions as Slater determinants and bosons as product wave functions, assuring accurate statistical behavior during particle exchange [2].

The extension from core to no-core calculations is an important and effective method for reproducing accurate theoretical results in the present study. This technique focuses on increasing the number of valence particles to investigate the static and dynamic structure of $^{19}_9F$. Brown et al. (1985) [3] analyzed high-resolution electron scattering data for $^{19}_9F$, using the sd-model space for positive-parity states and the zbm-model space for both positive- and negative-parity. Their analysis of form factors and transition matrix elements demonstrated the utility of configuration mixing, although the interaction parameters available at the time limited the ability to fully capture complex nuclear dynamics.

Sakuda (1992) [4] analyzed the form factors of $^{19}_9F$ using a cluster model that combined the $(t + {}^{16}_8O)$ and $(\alpha + {}^{15}_7N)$ configurations. The framework appropriately compatible with experimental data for the magnetic form factor of the $\frac{1}{2}^+$ ground state, relying on significant cluster parts to imitate its three maxima. However, it demonstrated little agreement during the longitudinal form factors of the $\frac{5}{2}^-, \frac{7}{2}^-$, and $\frac{9}{2}^-$ states. The difference highlighted the need for future theoretical advances.

Elastic and inelastic electron scattering of $^{19}_9F$ was utilized [5] to investigate transitions from $1/2^+$ to $(1/2^+, 3/2^+, 5/2^+, 7/2^+, and\ 9/2^+)$. For all transitions considered in the study, the isospin value was $1/2$. The researchers employed the OXBASH package program code to generate the one-body density matrix (OBDM) with a large basis truncation of $(0 + 2)\hbar\omega$ for the harmonic oscillator potential in the $spsdpf$-model space. Subsequently, all form factors were computed using specific codes written in FORTRAN. A large basis was consistently applied throughout the study.

In the context of studying the influence of shell model interactions on weakly interacting massive particles (WIMPs), R. Abdel Khaleq et al. [6] utilized the sd-model space, incorporating USD and USDB interactions. This methodology

enabled the calculation of energy levels and reduced transition probabilities for $^{19}_9F$, with single-particle states $1d_{5/2}, 2s_{1/2}$ and $1d_{3/2}$ considered for both protons and neutrons.

In 2016, Radhi et al. [7] investigated inelastic electron scattering inside $^{19}_9F$ using shell model calculations for both positive and negative parity states. Their research of positive parity states used the sd-model space with USDA interaction and focused on a selection of energy levels.

Elastic and inelastic scattering, energy levels, and reduced transition probabilities for specific positive and negative parity states were investigated using the nuclear shell model [7]. The sd-model space was employed for positive parity states, while the $spsdpf$ model space, truncated with $(0 + 2)\hbar\omega$, was applied for negative parity states. Although their work represents a significant contribution, certain limitations remain, particularly in the treatment of the $M3$ and $E4$ components. This highlights the necessity of extending the model spaces to achieve higher precision in future studies.

The present investigation evaluates the energy spectra, reduced transition probabilities, magnetic dipole moments, nuclear root-mean-square radii, binding energy, and both longitudinal and transverse inelastic electron scattering form factors for the negative parity states of $^{19}_9F$ nucleus. The analysis utilizes four distinct model spaces to systematically examine the influence of progressively extending the core configuration, culminating in a no-core framework, on the calculated nuclear properties and scattering observables. All types of model space Hamiltonians have been utilized to generate realistic wave functions for the negative-parity states of ^{19}F, including the $1/2^-$ at 0.1098MeV, $3/2^-_1$ at 1.459 MeV, $5/2^-_1$ at 1.3465MeV, and $7/2^-_1$ at 3.9987MeV.

The first approach is for $sd - pf$ shell called $sdpf$-model space, incorporating the active $1d_{5/2}, 2s_{1/2}$ and $1d_{3/2}$ orbitals above an inert $^{16}_8O$ core, treated as closed in the $(1s)^4(1p)^{12}$ configuration. The next model space, designated as Zuker–Buck–McGrory (zbm-model space), includes the active $1p_{1/2}, 1d_{5/2}$, and $2s_{1/2}$ orbitals positioned above an inert $^{12}_6C$ core. To accurately represent the complicated nuclear dynamics inside this approach, zbm-model space interactions, such as Zuker–Buck–McGrory-Interaction (ZBMI) [8] and Zuker-MCGRORY-WILDENTHAL (ZWM) [9], were used to create exact wave functions for the respective states.

The $p - sd$ orbits employ $psdpn$-model space [10] includes active shells $1p_{1/2}, 1p_{3/2}, 1d_{3/2}, 1d_{5/2},$ and $2s_{1/2}$ above the inert ^4_2He nucleus core, where the $(1s)^4$ configuration remains closed. This model space features center-of-mass motion and $p - sd$ orbits employ psd-model space interactions, such as PSDMK and PSDMWK, to connect the p- and sd-model spaces. The PSDMK interaction [11] comes from the pw-interaction inside the sd-model space. It contains the active $1d_{5/2}, 2s_{1/2},$ and $1d_{3/2}$ orbitals atop an inert $^{16}_8O$ core. Furthermore, the p-model space, with the Cohen-Kurath- POT ($CKPOT$) interaction [12], involves the $1p_{1/2}$, and $1p_{3/2}$ orbitals above the inert ^4_2He core. The last model space was used in present study known as $spsdpf$ includes active orbitals $1s_{1/2}, 1p_{3/2}, 1p_{1/2}, 1d_{5/2}, , 1d_{3/2}, 2s_{1/2}, 1f_{7/2}, 1f_{5/2}, 2p_{3/2},$ and $2p_{1/2}$, covering four major shells: $1s, 1p, 2s - 1d, and 1f - 2p$ with specific truncations. Considering no combination of $n\hbar\omega$ and $(0 + 2)\hbar\omega$ configurations, the model's interactions, created by Warburton and Brown [13], are based on a least-squares fit to 216 energy levels in the $A = 10-22$ area. With two body matrix element (TBME) and single particle energies (SPE) fitted for the p-shell and then expanded to include the $1s$ and $2p1f$ shells, the Warburton–Becker (WBT and WBP) interactions were used. The Warburton–Becker–Milliner–Brown (WBMB) interaction was used to represent cross-shell interactions [14].

The Skyrme Hartree–Fock (SHF) method, grounded in mean-field (MF) theory, has been utilized to compute single-particle matrix elements for excited nuclear states with various parameterizations. This approach minimizes the energy of a single Slater determinant derived from two-body interactions, offering an efficient solution through an analytic energy density functional for spherical nuclei [2, 15]. The SHF framework determines self-consistent potentials, single-particle densities, and minimal energy states, while also accommodating deformed or generalized bases for broader applications. Initially implemented by Vautherin and Brink, the Skyrme interaction has demonstrated significant success in nuclear MF calculations. Its parameterization, incorporating s- and p-wave expansions of effective nucleon–nucleon forces alongside density-dependent terms, captures critical nuclear physics, including shell-model truncations to closed-shell configurations and three-body effects [15]. As a phenomenological model, the parameters are refined against experimental data to ensure precision and reliability in predictive modeling [2].

2. THEORY AND METHODOLOGY

The reduced spin matrix element of electron–nucleus scattering between the initial and final nuclear states, $\langle J_i||\hat{T}^\eta_{J,t_z}(q)||J_f\rangle$, in the shell model framework is expressed as the sum of the one-body density matrix elements (OBDM) multiplied by the corresponding single-particle matrix elements of the transition operator, or

$$\langle J_i||\hat{T}^\eta_{J,t_z}(q)||J_f\rangle = \sum_{j_i,j_f} OBDM_{J,t_z}(j_i, j_f) \langle j_i||\hat{T}^\eta_{J,t_z}(q)||j_f\rangle. \tag{1}$$

Here J_i and J_f label initial and final nuclear states respectively and j_i and j_f label single-particle states for the shell model space. The symbol $\hat{T}^\eta$ is nuclear spins anyone of $\hat{T}^{Coulmb}$, $\hat{T}^{electric}$, or $\hat{T}^{magnetic}$ and $t_z = 1/2$ for a proton and $t_z = -1/2$ for a neutron

The electron scattering form factor has a longitudinal $F_L(q)$ and a transverse component, $F_T(q)$ and can be written in terms of reduced matrix elements of the electromagnetic transition operators of electron scattering, including the finite-size and center of mass correction form factors [1, 16]

$$|F_\eta^J(q)|^2 = \frac{4\pi}{Z^2(2J_i+1)} |\sum_{t_z} e(t_z)\langle J_f||\hat{T}_{J,t_z}^\eta(q)||J_i\rangle|^2 \times |F_{cm}(q)|^2|F_{fs}(q)|^2. \tag{2}$$

Here $F_\eta = F_{C,E,M}$ that is represents each of Coulomb, transverse electric and magnetic form factors. Since $Z\alpha \ll 1$, the electron scattering process can be accurately described using the plane-wave first-order Born approximation. In this approximation, the interaction is treated perturbatively, and the transition matrix elements are evaluated using the unperturbed nuclear states. Accordingly, the form factors presented in this work are computed within this approximation framework, which is valid for the kinematic conditions considered in this study [17, 18], with using Wigner-Eckart theorem [17] the total longitudinal (L)and transverse (T)form factors are given by

$$|F_L(q)|^2 = \frac{1}{2J_i+1}\sum_{J\geq 0} |\langle J_f||\hat{T}_{J,t_z}^{Coulomb}(q)||J_i\rangle|^2, \tag{3}$$

$$|F_T(q)|^2 = \frac{1}{2J_i+1}\sum_{J\geq 1}\{|\langle J_f||\hat{T}_{J,t_z}^{electric}(q)||J_i\rangle|^2 + |\langle J_f||\hat{T}_{J,t_z}^{magnetic}(q)||J_i\rangle|^2\}, \tag{4}$$

The total form factor can be expressed from the sum of its components [1]

$$|F(q,\theta)|^2 = (1-\omega^2/q^2)|F_L(q)|^2 + \left[\frac{1}{2}(1-\omega^2/q^2) + tan^2\frac{\theta}{2}\right]|F_L(q)|^2, \tag{5}$$

where θ is the electron scattering angle.

The Skyrme potential is employed as the central potential, characterized by its role as a mean-field potential. This potential approximates the collective effect of all nucleons within the nucleus, simulating the interactions among them while representing the realistic forces between nucleon pairs and triplets. Mathematically, the Skyrme interaction, V_{Skyrme}, is expressed as a combination of two-body and three-body components [2].

$$\hat{V}_{Skyrme} = \sum_{i<j} V_{ij}^{(2)} + \sum_{i<j<k} V_{ijk}^{(3)}. \tag{6}$$

The two-body part interaction also contains the mean central, spin-orbit, and the tensor parts. In momentum space it can be written as [18, 19]

$$\hat{V}_{Skyrme}(\boldsymbol{r}_1, \boldsymbol{r}_2) = \hat{V}^m + \hat{V}^{L.S} + \hat{V}^t. \tag{7}$$

Where

$$\hat{V}^m = t_0(1+x_0\hat{P}_\sigma)\delta_{12} + \frac{t_1}{2}(1+x_1\hat{P}_\sigma)(\hat{\boldsymbol{k}}_1^2+\hat{\boldsymbol{k}}_2^2)\delta_{12} + t_2(1+x_2\hat{P}_\sigma)\hat{\boldsymbol{k}}_2.\hat{\boldsymbol{k}}_1\delta_{12} + \frac{t_3}{6}(1+x_3\hat{P}_\sigma)\rho^\alpha(\boldsymbol{r})\delta_{12}, \tag{8}$$

$$\hat{V}^{L.S} = it_4 + (\hat{\sigma}_1 + \hat{\sigma}_2).\hat{\boldsymbol{k}}_2 \times \hat{\boldsymbol{k}}_1\delta_{12}, \tag{9}$$

$$\hat{V}^t = \frac{t_e}{2}\{[3(\hat{\sigma}_1.\hat{\boldsymbol{k}}_2)(\hat{\sigma}_2.\hat{\boldsymbol{k}}_2) - (\hat{\sigma}_1.\hat{\sigma}_2)\hat{\boldsymbol{k}}_2^2]\delta_{12} + [3(\hat{\sigma}_1.\hat{\boldsymbol{k}}_1)(\hat{\sigma}_2.\hat{\boldsymbol{k}}_1) - (\hat{\sigma}_1.\hat{\sigma}_2)\hat{\boldsymbol{k}}_1^2]\delta_{12}\} + t_s[3(\hat{\sigma}_1.\hat{\boldsymbol{k}}_2)(\hat{\sigma}_2.\hat{\boldsymbol{k}}_1) -$$
$$(\hat{\sigma}_1.\hat{\sigma}_2)\hat{\boldsymbol{k}}_2.\hat{\boldsymbol{k}}_1^2]\delta_{12}, \tag{10}$$

δ_{12} is the Dirac delta function, $\delta_{12} = \delta(\boldsymbol{r}_1 - \boldsymbol{r}_2)$, $\hat{\sigma}_1$ and $\hat{\sigma}_2$ are the vector of Pauli spin matrices for the first and second nucleon respectively, and three body part can be written as

$$V_{Skyrme}^{(3)} = t_3\delta_{12}\delta_{13}. \tag{11}$$

The $\hat{\boldsymbol{k}}_1$ and $\hat{\boldsymbol{k}}_2$ operators are the relative momentums, wave vectors, of the first and second nucleon which operate on the wave functions to the right $|\psi\rangle$ and to the left $\langle\psi|$ respectively and having the form

$$\hat{\boldsymbol{k}}_1 = \frac{1}{2i}(\vec{\nabla}_1 - \vec{\nabla}_2), \quad \hat{\boldsymbol{k}}_2 = -\frac{1}{2i}(\overleftarrow{\nabla}_1 - \overleftarrow{\nabla}_2). \tag{12}$$

The reduced transition probability [1], representing the probability of a nuclear transition between states, is mathematically expressed as:

$$B(\eta J) = \frac{Z^2}{4\pi}\left[\frac{(2J+1)!!}{k^J}\right]^2 |F_J^\eta(k)|^2. \tag{13}$$

Here $k = \frac{E_x}{\hbar c}$

3. RESULT AND DISCUSSION

The study of nuclear electromagnetic form factors provides critical insights into the structural and dynamic properties of atomic nuclei. This work systematically examined the longitudinal and transverse form factors of $^{19}_9F$ for negative parity states through electron scattering, employing advanced shell-model techniques. Various model spaces

were utilized to highlight the effects of core extensions and model-space expansions. The $sdpf$-model space with $^{16}_{8}O$ as the core and SDPFK interaction focused on proton-neutron correlations, while the zbm-model space with a $^{12}_{6}C$ core explored configuration mixing in the p-shell via $ZBMI$ interaction. The psd-model space, based on a $^{4}_{2}He$ core, and the $spsdpf$ model space, treating all 19 nucleons as fully interacting, captured the nucleus's complete structure. Theoretical results were compared with experimental data to improve the influence of model-space truncation and interaction choices. One-body density matrix (OBDM) components, computed by using NuShellX@MSU [20], enabled calculation of MJ and EJ operators. Radial wave functions for single-particle matrix elements were generated using Skyrme-Hartree-Fock potentials ($SkXcsb, SkXta, SkXtb, and SLy4$), the Wood-Saxon potential, and a harmonic oscillator potential ($b = 1.833 fm$) [3], facilitating a comprehensive model comparison. Utilizing the SLy4 parameterization, the computed root mean square (rms) charge radius was determined to be $2.876 fm$, aligning well with the experimental measurement of $2.8976 fm$ [21]. Additionally, the binding energy calculation yielded 146.3719 MeV, exhibiting strong consistency with the experimental value of 147.803 MeV [22]. Furthermore, the nuclear magnetic dipole moment for the $5/2^{-}_{1}$ state was evaluated at $0.613 nm$, which closely approximates the experimental determination of $0.67(11) nm$ [23-25].

Discussions of the results is organized systematically to provide a comprehensive understanding of the findings. The present analysis encompasses several key aspects: inelastic electron scattering form factors, energy level transitions and associated probabilities. These results are presented sequentially, following an order based on increasing angular momentum, offering a coherent narrative of the nuclear structure and dynamics under investigation.

3.1. The form factors

The current study utilized the $sdpf$-model space with the SDPFK two-body effective interaction [26], the zbm-model space with the ZBMI effective interaction [8], the psd-model space using the PSDMK effective interaction [11], and the $spsdpf$-model space with the WBT interaction to reproduce both longitudinal and transverse form factors. This approach was designed to highlight the effects of extending the core and to enable a comparative analysis between the different model spaces.

Based on the selection rules governing total angular momentum and parity conservation, the permissible multipole components for pure coulomb and transverse form factors are $C1$ and $E1$ respectively. The elastic Coulomb $C1$ form factors for the ground state of the $^{19}_{9}F$ nucleus $1/2^{-}$ were computed using wave functions from the $sdpf, zbm, psd$, and $spsdpf$ model spaces, along with parameterizations from $Skxcsb, Skxta, Skxtb, Sly4$, Wood-Saxon (WS), and harmonic oscillator (HO) potentials. The results, depicted in Fig. (1), are compared against experimental data from Ref. [1].
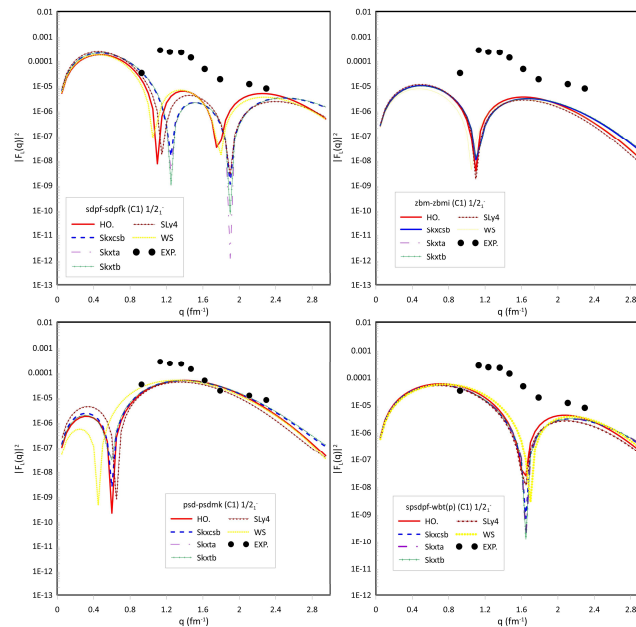

Figure 1. Theoretical longitudinal form factor $C1$ for $1/2^{-}_{1}$ compared with experimental data [3, 27]

The $sdpf$ model space, with $^{16}_{8}O$ as the core, effectively reproduces the C1 form factor at momentum transfer values of $q = 0.92 fm^{-1}$ and $q = (2.00 - 2.26) fm^{-1}$. However, in the intermediate range $q = (1.00 - 2.00) fm^{-1}$, while the qualitative agreement with experimental data remains reasonable, the quantitative agreement is notably poor due to the restricted participation of nucleons in the interaction. Conversely, employing the zbm model space with $^{12}_{6}C$ as the core results in a poor reproduction of the C1 form factor. This model exhibits a slight shift relative to the experimental data for $q = (0.90 - 2.00) fm^{-1}$. Nevertheless, at $q > 2.00 fm^{-1}$, it achieves good agreement, particularly when using the $Skxcsb$ Skyrme potential. On the other hand, the psd model space, with $^{4}_{2}He$ as the core, successfully reproduces the C1 form factor both qualitatively and quantitatively across all types of potentials. Notably, at $q = 0.90 fm^{-1}$, Wood-Saxon potential has a

significant influence in optimizing the reproduction of the form factor. Furthermore, within the range $q = (2.00 - 2.50) fm^{-1}$, the Skyrme interactions ($Skxcsb$ and $Skxtb$) play a crucial role in enhancing the accuracy of the form factor reproduction. Finally, employing the $spsdpf$ model space within a no-core shell model framework for C1 form factor calculations demonstrates that both potential types yield comparable results. The no-core shell model not only ensures a quantitatively accurate reproduction but also achieves the best agreement at both initial and final scattering points.

The calculated E1 form factors associated with the negative-parity state of $(1/2^-, 0.1098 \, MeV)$ are presented in Fig. 2. The reproduction of the E1 form factor within the $sdpf$ model space using the SDPFK interaction exhibits overall poor agreement with experimental data. However, at specific momentum transfer values, such as $q = 0.78 \, fm^{-1}$ and within the range $q = 1.00 - 1.20 \, fm^{-1}$ reasonable agreement is observed, with the best reproduction occurring in the interval $q = (2.00 - 2.50) \, fm^{-1}$. For $q = (1.40 - 1.60) \, fm^{-1}$, the Harmonic Oscillator (HO) and Wood-Saxon (WS) potentials demonstrate a qualitatively satisfactory reproduction of the E1 form factor, while the SLy4 Skyrme interaction extends this agreement up to $q = 1.80 \, fm^{-1}$. Expanding the core from $^{16}_{8}O$ to $^{12}_{6}C$ effectively resolves many discrepancies in reproducing the E1 form factor. By utilizing the zbm model space and ZBMI interaction for seven nucleons outside the core, the E1 form factors are successfully reproduced in good agreement with experimental data across all potential types examined in this study, except for the initial drop in the momentum transfer region.
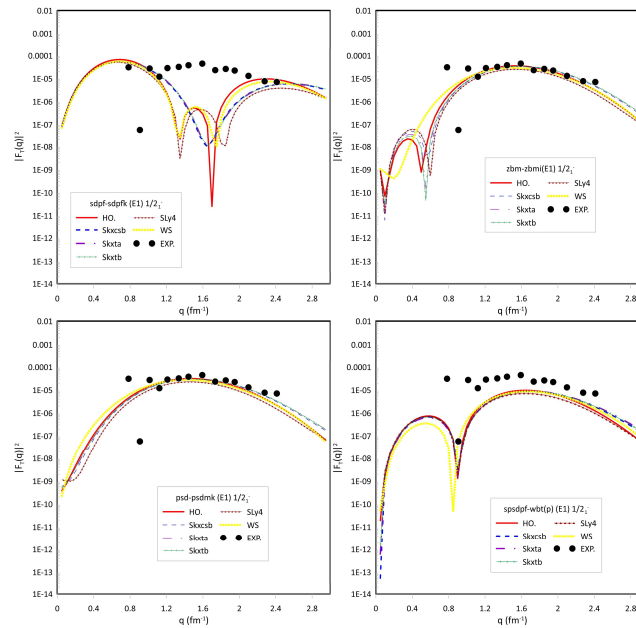

Figure 2. Theoretical transverse form factor $E1$ for $1/2^-_1$ compared with experimental data [3, 27]

Expanding the core to $^4_2 He$ within the psd model space, incorporating fifteen interacting nucleons, yields an optimal reproduction of the E1 form factor, achieving both qualitative and quantitative agreement across the entire momentum transfer region. The only exception is the initial drop in the momentum transfer, which occurs within the scattering region. However, this discrepancy is effectively resolved through no-core shell model calculations. Furthermore, employing the no-core shell model with the $spsdpf$ model space, where all nucleons actively participate in the interaction, helps refine fluctuations in the scattering process. This highlights the significant impact of extending from a core-based framework to a no-core approach in enhancing the accuracy of form factor reproduction.

The C1 form factor for the negative-parity state $3/2^-_1$ (1.459 MeV) is depicted in Fig. (3). Within the $sdpf$ model space, which considers three interacting nucleons, the C1 form factor for this state exhibits three distinct scattering peaks, resulting in an overall quantitatively good agreement with experimental data. However, the first drop in the form factor occurs experimentally around $q = 1.76 \, fm^{-1}$, whereas all potential types within this model space predict the decline at lower momentum transfer values. To address this fluctuation across all potential types, a second systematic peak rapidly emerges, aligning with the experimental momentum transfer points, particularly for the Harmonic Oscillator (HO) potential. The minor fluctuation preceding this peak also leads to a delayed reproduction of the second experimentally observed rising peak in theoretical calculations. Nevertheless, this state represents an extreme case, as previous theoretical studies by Brown et al. [3] and Donne et al. [28] exhibit significant deviations from experimental data.

Conversely, the zbm model space, with $^{12}_{6}C$ as the core, qualitatively reproduces the C1 form factor while maintaining the overall scattering shape. However, it exhibits systematic shifts, suggesting that the theoretical scattering process begins prematurely than observed experimentally. This discrepancy may be mitigated through minor parameter adjustments within the model space. In contrast, the psd model space, with $^4_2 He$ as the core, successfully reproduces the C1 form factor up to the first drop in momentum transfer but fails to capture the second rising peak. Ultimately, the C1 form factor for the $3/2^-_1$ state achieves the highest qualitative agreement with experimental data [3] and exhibits good quantitative agreement when calculated using the $spsdpf$ model space within no-core shell model framework. Notably,

while R.A. Radhi et al. [7] previously reported that the C1 form factor for this state could not be reproduced using the no-core shell model, the present study demonstrates that no-core approach successfully achieves a strong agreement with experimental data.
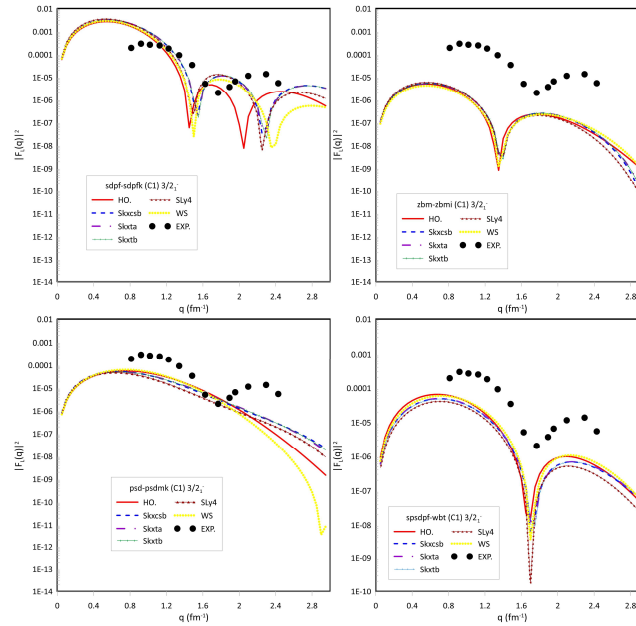
Figure 3. Theoretical longitudinal form factor $C1$ for $3/2_1^-$ compared with experimental data [3, 28]

The total form factor, incorporating both E1 and M2 contributions for the $3/2_1^-$ state, is illustrated in Fig. (4). The $sdpf$ model space achieves the best agreement within the momentum transfer range of $q = (1.40 - 1.60)\ fm^{-1}$, particularly when employing Harmonic Oscillator (HO), Wood-Saxon (WS), and SLy4 potential parameterizations.
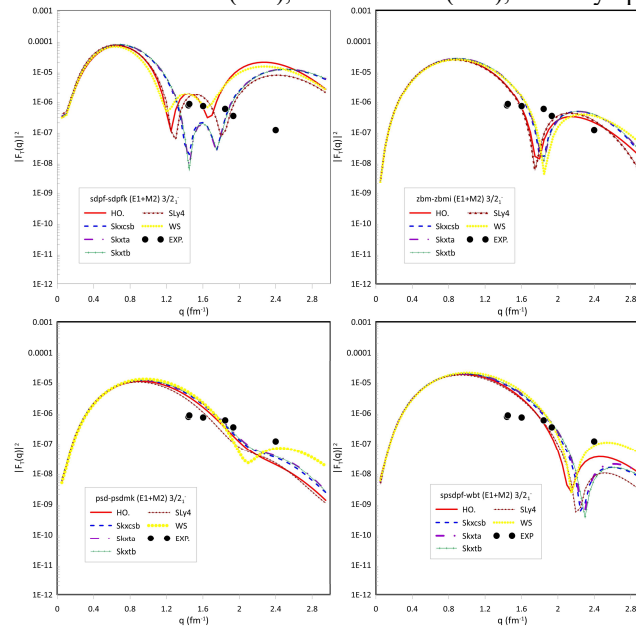
Figure 4. Theoretical Transverse form factors $E1, and\ M2$ for $3/2_1^-$, $1.459\ MeV$ compared with experimental data [3, 28].

Additionally, for $q = (1.70 - 2.00)\ fm^{-1}$, Skyrme potentials—especially SkXcsb, SkXtab, and SkXtb—exhibit strong agreement with experimental data. However, at the end of scattering point near $q = 2.40\ fm^{-1}$, the $sdpf$ model space fails to accurately reproduce the form factor. In contrast, the zbm model space provides a quantitatively consistent reproduction of the total transverse form factor for this state, except at the peak near $q = 2.40\ fm^{-1}$. Both the psd model space (with $_2^4He$ as the core) and the $spsdpf$ no-core shell model successfully cover the entire momentum transfer range throughout the scattering process. Notably, they achieve the best agreement at the final experimental curvature point, $q = 2.40\ fm^{-1}$, particularly when using WS potential.

The C3 form factor for the $5/2_1^-$- state is depicted in Fig. 5. The $sdpf$ model space initially demonstrates a qualitatively good agreement in reproducing the form factor; however, near $q = 2.00\ fm^{-1}$, it exhibits fluctuations and rapidly declines.

Figure 5. Theoretical longitudinal form factor $C3$ for $5/2_1^-$ compared with experimental data [3, 28].

In contrast, the zbm model space, incorporating seven interacting nucleons with the ZBMI interaction, successfully covers the entire momentum transfer range and accurately reproduces the C3 form factor both qualitatively and quantitatively across all potential parameterizations. Similarly, the psd model space, with $_2^4He$ as the core and the PSDMK interaction for fifteen nucleons, achieves the best agreement, particularly when using the Harmonic Oscillator (HO) potential and SLy4 Skyrme parameterization. Furthermore, the $spsdpf$ model space, employing WBT interaction within no-core shell model framework, reproduces the C3 form factor in good agreement, albeit with minor fluctuations around $q = 2.30 \ fm^{-1}$.

The total transverse form factor for the $5/2_1^-$ state with (1.3456 MeV), which represents the combined contributions of M2 and E3, is illustrated in Fig. 6.

Figure 6. Theoretical transverse form factor $E3, and \ M2$ for $5/2_1^-$, $1.3456 \ MeV$ compared with experimental data [3, 28].

The $sdpf$ model space, incorporating only three interacting nucleons with $_8^{16}O$ as the core, demonstrates some capability in reproducing the form factor. However, it exhibits two significant fluctuations, characterized by rapid declines near $q = (0.80 - 1.20) \ fm^{-1}$ and $q = (1.80 - 2.20) \ fm^{-1}$, with variations depending on the potential type. In contrast, the zbm, psd, and $spsdpf$ model spaces achieve optimal agreement with experimental data, both qualitatively and quantitatively, effectively reproducing the form factor across the entire momentum transfer range.

The C3 form factor for the $7/2_1^-$ state is presented in Fig. 7. The $sdpf$ model space demonstrates a poor ability to reproduce the form factor, likely due to the limited number of nucleons involved in the interaction. This constraint causes

the theoretical scattering process to occur slightly earlier than the experimental results. Expanding the core to $^{12}_{6}C$ within the *zbm* model space and incorporating four additional nucleons significantly improves the agreement with experimental data, particularly in the end phase of the scattering process around $q = (2.00 - 2.40) \, fm^{-1}$, especially when employing Skyrme parameterizations. Similarly, the *psd* model space with a $^{4}_{2}He$ core produces a form factor that closely resembles the *zbm* model space results. This similarity arises from the structural equivalence of the $^{12}_{6}C$ core to three clustered $^{4}_{2}He$ nuclei in the context of this single-particle excitation state.
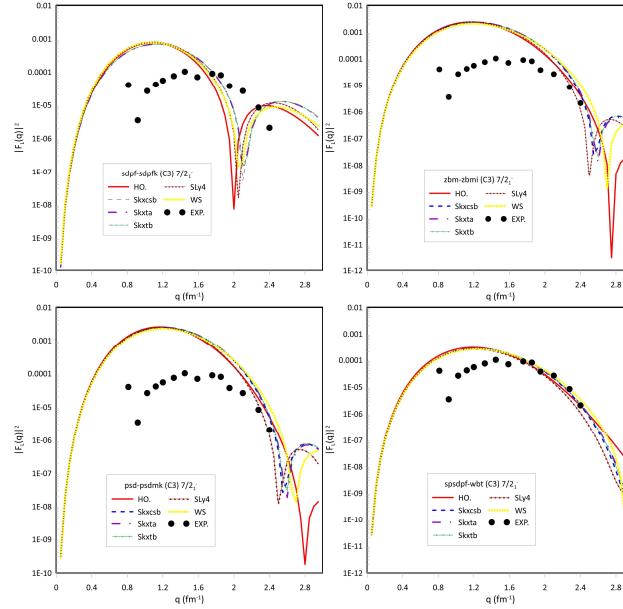
Figure 7. Theoretical longitudinal form factor $C3$ for $7/2^-_1$ compared with experimental data [3, 27].

The observed resemblance of the C3 form factor when using $^{12}_{6}C$ and $^{4}_{2}He$ as core nuclei indicates that the primary contribution originates from valence nucleons within the *sd*-shell, rather than from core excitations. Factors such as transition density, wavefunction overlap, and the minimal role of core excitation contribute to the nearly identical results across both model spaces. Furthermore, the *spsdpf* model space, representing no-core shell model calculation, successfully reproduces the C3 form factor both qualitatively and quantitatively. This highlights the significance of transitioning from core-based to no-core calculations in achieving improved theoretical-experimental consistency.

The total transverse form factor for the $7/2^-_1$ state at 3.9987 MeV, comprising E3 and M4 contributions depicted in Fig. 8. The *sdpf* model space successfully captures the qualitative features of the form factor within the momentum transfer range $q = (0.80 - 1.60) \, fm^{-1}$, though it fails to achieve quantitative agreement in this region. However, for $q = (1.60 - 2.10) \, fm^{-1}$, the model exhibits a strong correspondence with experimental data.
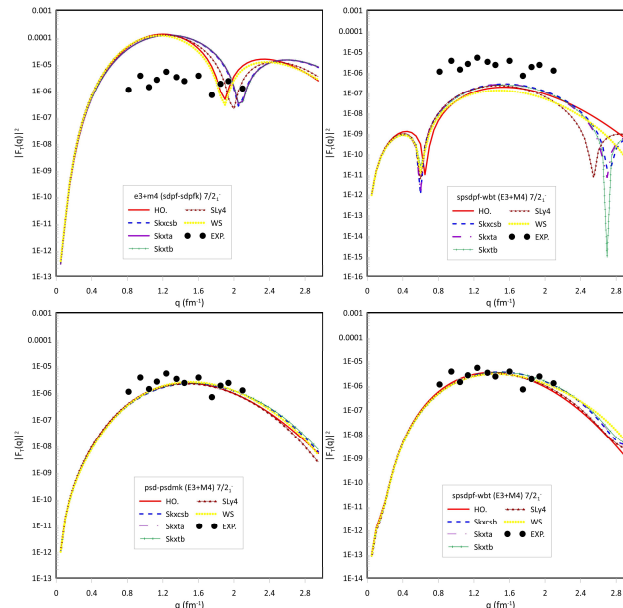
Figure 8. Theoretical transverse form factors $E3$, *and* $M4$ for $7/2^-_1$, $3.9987 \, MeV$ compared with experimental data [3, 28]

Conversely, the *zbm* model space effectively reproduces the total transverse form factor across the entire momentum transfer range, maintaining a high degree of qualitative accuracy. Nonetheless, it falls short in precisely matching the quantitative values of the experimental results, with a systematic discrepancy.

In contrast, both the *psd* model space with ^4_2He core and the *spsdpf* model space (no-core shell model) demonstrate superior performance, successfully reproducing the form factor with high accuracy in both qualitative and quantitative aspects. This highlights the enhanced predictive capability of models incorporating extended nucleon interactions, particularly in no-core shell model calculations.

3.2. Energy levels

The negative parity energy levels of $^{19}_9F$ reveal a profound dependence on the choice of model space and interaction, reflecting the intricate many-body dynamics governing nuclear structure and illustrated in Fig. 9. The *sdpf* model space with the SDPFK interaction with $^{16}_8O$ core provides an initial approximation but struggles to fully capture experimental trends due to its limited treatment of nucleon correlations. Extending the core to $^{12}_6C$ (*zbm* model space, ZBMI interaction) significantly refines the predictions, particularly for the $J^\pi = 9/2^-_1$ state, where the additional valence nucleons improve agreement with experimental data. The *psd* model space with PSDMK interaction with ^4_2He core introduces a different perspective by treating $^{12}_6C$ as three ^4_2He clusters, resulting in comparable C3 form factors and energy levels to the ZBM approach. However, the most striking improvement emerges in the no-core shell model (*spsdpf* model space), where WBT and WBP interactions systematically reproduce the experimental spectrum with remarkable precision. This transition from a static core approximation to a fully correlated nucleonic treatment, highlights the essential role of many-body correlations, particularly in capturing the finer details of higher negative parity states.

The no-core shell model correctly reproduces both qualitative trends and quantitative values along with energy levels of $J^\pi = 1/2^-_1, 3/2^-_1, 5/2^-_1$ and $7/2^-_1$. The additional use of no-core treatment improves the description of the $9/2^-_1$ state above the *zbm* model space although core extensions work adequately but full-core correlation remains essential for precision results. The accuracy of interaction potential selecting along with model space truncation needs improvement because precision degrades in high-energy excitations. Nuclear structure modeling evolves toward fundamental insights about nuclear forces because researchers pick between core-based predictions and fully no-core approaches. This advancement is pivotal in refining our understanding of light nuclei and their role in broader nuclear astrophysics and reaction dynamics.
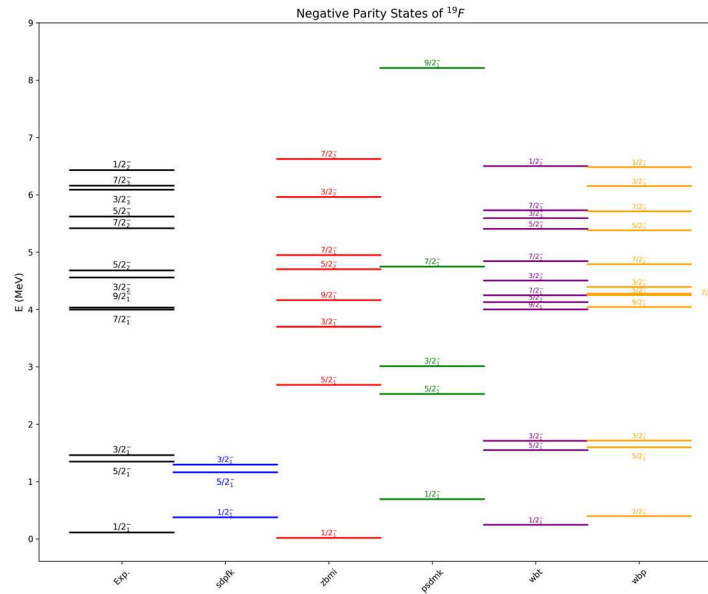
Figure 9. Energy levels of the negative parity states of the $^{19}_9F$ nucleus, compared with experimental data obtained from Ref. [22, 29]

3.3. Reduced transition probabilities

In the present study, the calculations of reduced transition probabilities $B(\eta J)$, are carried out using distinct model space interactions. To determine the electric quadrupole $B(E1)$ and magnetic dipole $B(M2)$ transitions among low-lying nuclear states, standard effective charges of $\delta e_p = 0.5$ and $\delta e_n = 0.5$ were applied. One-body density matrices (OBDM) were constructed for the respective model spaces based on their specific interactions. The above technique emphasizes how important it is to use interaction-specific parameters and well-chosen default values when expressing electromagnetic characteristics in nuclear structures.

The reduced transition probabilities $B(J \rightarrow J')$ which compare theoretical predictions from different model spaces and interactions against experimental data for negative parity states of $^{19}_9F$ are presented in Table 1. The probability to observe electromagnetic transition between nuclear states is quantified by reduced transition probabilities. The available

experimental values function as reference points to evaluate the predictive ability of multiple nuclear models. Experimental values of the $1/2^+ \rightarrow 1/2^-$ transition yield $0.00055(6)$ e^2fm^2 as its E1 transition probability, while the $sdpf$ model (SDPFK interaction) computes a value of 0.01190. The transition strength found in zbm (0.005804) and psd (0.003561) is lower than experimental data whereas the WBT and WBP interactions within the $spsdpf$ model yield strongly reduced values indicating decreased probability in the no-core shell model framework.

The E1 transition for $1/2^+ \rightarrow 3/2^-$ demonstrates that the no-core shell model ($spsdpf$) achieves the closest agreement with experimental data compared to other model spaces. Following the no-core approach, the ^4_2He core-based (psd) model also provides a reasonably accurate prediction, further highlighting the impact of extending the model space in refining transition probabilities. Additionally, the M2 transition for $1/2^+ \rightarrow 3/2^-$ shows significant deviation between models, with $sdpf$ predicting 7.117, whereas other models yield much smaller values, indicating the sensitivity of M2 transitions to the underlying interaction.

The $1/2^+ \rightarrow 5/2^-$ transitions, particularly for M2 and E3 multipoles, exhibit notable differences among model spaces. The zbm model space (with ZBMI interaction) predicts 255.6 e^2fm^2 for the E3 transition, considerably larger than the $sdpf$ (8.174) and no-core shell model predictions (339 for WBP and 328 for WBT), suggesting an enhanced transition strength with increasing model space complexity. The M4 transition shows significant variations across model spaces, with the $sdpf$ model predicting 438.2, while no-core calculations yield considerably lower values, indicating potential limitations in model truncation or interaction parameterization.

Overall, the Table 1, illustrates the progressive refinement of transition probabilities as model spaces extend from core-based approximations to fully correlated no-core shell model calculations. zbm and $sdpf$ models provide reasonable approximations for low-energy transitions, While the $spsdpf$ model (no-core shell model) demonstrates improved accuracy in capturing multipole transitions, particularly for higher-order electromagnetic transitions (E3, M4, and E5). These results reinforce the importance of model space expansion and interaction refinements in achieving a more comprehensive understanding of nuclear excitation dynamics.

Table 1. Reduced transition probabilities of negative parity states of $^{19}_9F$ compared with experimental [22, 29].

$J_i^\pi \rightarrow J_f^\pi$		$B(\eta J)$ e^2fm^{2J}					
	wL	$Exp.$	$sdpf - sdpfk$	$zbm - zbmi$	$psd - psdmk$	$spsdpf - wbp$	$spsdpf - wbt$
$1/2^+ \rightarrow 1/2^-$	E1	0.00055(6)	0.1190	0.005804	0.003561	0.001919	0.002630
$1/2^+ \rightarrow 3/2^-$	E1	0.0009(2)	0.3007	0.000075284	0.0002681	0.0004784	0.0004972
$1/2^+ \rightarrow 3/2^-$	M2	-	7.117	3.746	0.08010	0.6984	0.5690
$1/2^+ \rightarrow 5/2^-$	M2	-	3.036	0.6826	0.04236	0.08628	0.1853
$1/2^+ \rightarrow 5/2^-$	E3	-	8.174	255.6	259.9	339	327.6
$1/2^+ \rightarrow 7/2^-$	E3	-	145.1	595.1	622.2	64.4	109.6
$1/2^+ \rightarrow 7/2^-$	M4	-	5151	-	7876	4733	5697
$1/2^+ \rightarrow 9/2^-$	M4	-	438.2	-	6.503	14.77	14.62
$1/2^+ \rightarrow 9/2^-$	E5	-	341.8	-	-	302.4	235.9

4. CONCLUSION

The current study explores negative parity states of $^{19}_9F$, showing how transitioning from core-based to no-core shell models improves nuclear structure predictions. The findings highlight those different nuclear properties are optimally reproduced at varying core levels, emphasizing the role of valence nucleons and many-body correlations. For electromagnetic form factors, $sdpf$ model space ($^{16}_8O$ core) provides an initial approximation, but extending to $^{12}_6C$ (zbm model space) significantly improves the C1 and C3 form factors. Further extension to ^4_2He (psd model space) successfully reproduces the E1 and total transverse form factors across the momentum transfer range. The no-core shell model ($spsdpf$) achieves the most accurate results, particularly in resolving initial momentum fluctuations and ensuring consistency in both low- and high-momentum transfer regions. The energy level analysis confirms that core extensions refine predictions, particularly for the $9/2^-$ state. However, the no-core shell model consistently provides the best agreement across all negative-parity states, highlighting the necessity of fully correlated nucleon interactions to capture higher-energy excitations with degree of precision. Reduced transition probability calculations further reinforce the impact of model space selection. While $sdpf$ and zbm models provide reasonable B(E1) and B(M2) values for low-lying transitions, the no-core shell model achieves superior accuracy for higher-order transitions such as E3 and M4. Notably, the ^4_2He-core model space effectively predicts the $1/2^+ \rightarrow 3/2^-$ E1 transition, illustrating that intermediate core choices can yield accurate results for specific states. Overall, this study demonstrates that systematically transitioning from core-based to no-core models optimizes the reproduction of nuclear properties. These findings support nuclear research centers and have direct implications for nuclear astrophysics and reaction dynamics.

ORCID

Berun N. Ghafoor, https://orcid.org/0000-0003-0450-3919

REFERENCES

[1] R. Hofstadter, "Electron scattering and nuclear structure," Reviews of Modern Physics, **28**(3), 214 (1956). https://doi.org/10.1103/RevModPhys.28.21

[2] D. Vautherin, and D.M.T. Brink, "Hartree-Fock calculations with Skyrme's interaction. I. Spherical nuclei," Physical Review C, **5**(3), 626 (1972). https://doi.org/10.1103/PhysRevC.5.626

[3] B.A. Brown, *et al*., "Shell-model analysis of high-resolution data for elastic and inelastic electron scattering on F^{19}," Physical Review C, 32(4), 1127 (1985). https://doi.org/10.1103/PhysRevC.32.1127

[4] T. Sakuda, "Cluster Model Study of Electron Scattering on 19F," Progress of Theoretical Physics, **87**(5), 1159-1169 (1992). https://doi.org/10.1143/ptp.87.5.1159

[5] R.A. Radhi, A.A. Abdullah, and A.H. Raheem, "Calculations of elastic and inelastic electron scattering on ^{19}F using large-basis no core-shell model wave functions," Nuclear Physics A, **798**(1-2), 16-28 (2008). https://doi.org/10.1016/j.nuclphysa.2007.10.010

[6] R.A. Khaleq, *et al*., "Impact of shell model interactions on nuclear responses to WIMP elastic scattering," Physical Review D, **109**(7), 075036 (2024). https://doi.org/10.1103/PhysRevD.109.075036

[7] R.A. Radhi, A.A. Alzubadi, and E.M. Rashed, "Shell model calculations of inelastic electron scattering for positive and negative parity states in ^{19}F," Nuclear Physics A, **947**, 12-25 (2016). https://doi.org/10.1016/j.nuclphysa.2015.12.002

[8] A.P. Zuker, B. Buck, and J.B. McGrory, "Structure of O^{16}," Physical Review Letters, **21**(1), 39 (1968). https://doi.org/10.1103/PhysRevLett.21.39

[9] J.B. McGrory, and B.H. Wildenthal, "Shell-model calculations for A=18, 19, and 20 nuclei with core excitation included explicity," Physical Review C, **7**(3), 974 (1973). https://doi.org/10.1103/PhysRevC.7.974

[10] Y. Utsuno, and S. Chiba, "Multiparticle-multihole states around O 16 and correlation-energy effect on the shell gap," Physical Review C – Nuclear Physics, **83**(2), 021301(R) (2011). https://doi.org/10.1103/PhysRevC.83.021301

[11] B.M. Preedom, and B.H. Wildenthal, "Shell-Model Calculations for Na^{22} and Ne^{22}," Physical Review C, **6**(5), 1633 (1972). https://doi.org/10.1103/PhysRevC.6.1633

[12] S. Cohen, and D. Kurath, "Effective interactions for the 1p shell," Nuclear Physics, **73**(1), 1-24 (1965). https://doi.org/10.1016/0029-5582(65)90148-3

[13] E.K. Warburton, and B.A. Brown, "Effective interactions for the 0p1s0d nuclear shell-model space," Physical Review C, **46**(3), 923 (1992). https://doi.org/10.1103/PhysRevC.46.923

[14] E.K. Warburton, J.A. Becker, and B.A. Brown, "Mass systematics for A= 29–44 nuclei: The deformed A∼ 32 region," Physical Review C, **41**(3), 1147 (1990). https://doi.org/10.1103/PhysRevC.41.1147

[15] B.A. Brown, "Synthesis of mean-field and shell-model configuration-mixing methods," Riken Review, (26), 53-57 (2000).

[16] J.P. Elliott, and T.H.R. Skyrme, "Centre-of-mass effects in the nuclear shell-model," Proceedings of the Royal Society of London Series A. Mathematical and Physical Sciences, **232**(1191), 561-566 (1955). https://doi.org/10.1098/rspa.1955.0239

[17] H. Euteneuer, *et al*., "Elastic electron scattering from the multipole moment distributions of Mg^{25}," Physical Review C, **16**(5), 1703 (1977). https://doi.org/10.1103/PhysRevC.16.1703

[18] T.W. Donnelly, and J.D. Walecka, "Electron scattering and nuclear structure," Annu. Rev. Nucl. Sci. **25**, 329-405 (1975). https://doi.org/10.1146/annurev.ns.25.120175.001553

[19] D. Vautherin, "Hartree-Fock calculations with Skyrme's interaction. II. Axially deformed nuclei," Physical Review C, **7**(1), 296 (1973). https://doi.org/10.1103/PhysRevC.7.296

[20] B.A. Brown, and W.D.M. Rae, "The shell-model code NuShellX@ MSU," Nuclear Data Sheets, **120**, 115-118 (2014). https://doi.org/10.1016/j.nds.2014.07.022

[21] I. Angeli, and K.P. Marinova, "Table of experimental nuclear ground state charge radii: An update," Atomic Data and Nuclear Data Tables, **99**(1), 69-95 (2013). https://doi.org/10.1016/j.adt.2011.12.006

[22] National Nuclear Data Center (NNDC), Brookhaven National Laboratory, Upton, NY 11973-5000, http://www.nndc.bnl.gov/

[23] N.J. Stone, "Table of nuclear magnetic dipole and electric quadrupole moments," Atomic Data and Nuclear Data Tables, **90**(1), 75-176 (2005). https://doi.org/10.1016/j.adt.2005.04.001

[24] N.J. Stone, Table of recommended nuclear magnetic dipole moments. No. INDC (NDS)--0794. International Atomic Energy Agency, 2019.

[25] N.J. Stone, Table of Recommended Nuclear Magnetic Dipole Moments: Part II, Short-Lived States. No. INDC (NDS)--0816. International Atomic Energy Agency, 2020.

[26] K. Kazunari, *et al*., "Shell-model study for neutron-rich sd-shell nuclei," Physical Review C – Nuclear Physics, **83**(1), 014320 (2011). https://doi.org/10.1103/PhysRevC.83.014320

[27] A.J.H. Donné, *et al*., "Elastic magnetic electron scattering from ^{19}F," Nuclear Physics A, **455**(3), 453-476 (1986). https://doi.org/10.1016/0375-9474(86)90317-9

[28] A.J.H. Donné, *et al*., "Transverse electroexcitation of positive-and negative-parity states in ^{19}F," Nuclear Physics A, **469**(3), 518-530 (1987). https://doi.org/10.1016/0375-9474(87)90037-6

[29] D.R. Tilley, *et al*., "Energy levels of light nuclei A= 18–19," Nuclear Physics A, **595**(1), 1-170 (1995). https://doi.org/10.1016/0375-9474(95)00338-1

ПОРІВНЯННЯ МОДЕЛЕЙ З ОСНОВНИМ ТА БЕЗОСНОВНИМ ОБОЛОНКАМИ ПРИ ЗБУДЖЕННІ СТАНІВ ВІД'ЄМНОЇ ПАРНОСТІ $_9^{19}$F
Берун Н. Гафур[a,c], Азіз Х. Фатах[b], Арі К. Ахмед[a]
[a]Університет в Сулеймані, Коледж освіти, Фізичний факультет, Ірак
[b]Університет в Сулеймані, Коледж наук, Фізичний факультет, Ірак
[c]Науково-дослідний центр, університет в Сулеймані, Ірак

У цьому дослідженні досліджується ядерна структура низько розташованих станів негативної парності в $^{19}_9$F з використанням комбінації оболонкової моделі та методу Хартрі-Фока (HF). Комплексний аналіз ядерних властивостей, включаючи енергетичні спектри, форм-фактори розсіювання електронів, сили переходів, енергії зв'язку та радіуси зарядів, було проведено

в чотирьох модельних просторах: *sdpf*-модельному просторі, *zbm*-моделі, *psd*-моделі та розширеному *spsdpf*-модельному просторі без оболонки. У кожному модельному просторі було застосовано різні ефективні взаємодії для оцінки їхнього впливу на поведінку ядра. Метод HF, що використовує кілька параметризацій Скірма, разом з гармонічним осцилятором та потенціалами Вудса-Саксона, був застосований для обчислення радіальних хвильових функцій одночастинок, необхідних для розрахунків матричних елементів. Результати показують, що розрахунки HF на основі Скірма, при інтеграції з методами моделі оболонки, ефективно фіксують фундаментальні властивості ядра. Систематичне порівняння з експериментальними даними показує, що перехід від модельних просторів з обмеженим ядром до повністю без'ядерної структури значно покращує відтворення форм-факторів розсіювання електронів, особливо в поздовжніх (C1, C3) та поперечних (E1, M2) компонентах. Примітно, що специфічні стани демонструють оптимальну узгодженість на різних рівнях ядра: стани $3/2_1^-$ та $5/2_1^-$ найкраще відтворюються в без ядерній моделі оболонки, тоді як стан $7/2_1^-$ досягає високої точності в модельних просторах zbm та psd. Загалом, це дослідження підкреслює критичний вплив вибору модельного простору та вибору взаємодії в теоретичних ядерних дослідженнях. Поступове уточнення розрахунків від розрахунків на основі ядра до розрахунків без ядра підкреслює роль багаточастинкових кореляцій у ядерних збудженнях та забезпечує глибше розуміння внутрішньої структури $^{19}_9F$, сприяючи розвитку теорії структури ядра та динаміки реакцій.

Ключові слова: *структура ядра; модельні простори; core to no-core; Skyrme-HF; фтор-19*

THE INFLUENCE OF FRACTIONAL DERIVATIVES ON THERMODYNAMIC PROPERTIES BY STUDYING THE CPSEHP INTERACTION

M. Abu-Shady*, Sh. Y. Ezz-Alarab

Faculty of Science, Department of Mathematics and Computer Science, Menoufia University, Shebin Elkom 32511, Egypt
*Corresponding Author e-mail: dr.abushady@gmail.com

The parametric Nikiforov-Uvarov (N-U) method is employed in conjunction with a generalized fractional derivative (GFD) to investigate the energy eigenvalues and the total normalized wave function associated with the Coulomb plus screened exponential hyperbolic potential (CPSEHP) in terms of Jacobi polynomials. This potential exhibit maximum effectiveness at lower values of the screening parameter. To explore the thermal and superstatistical characteristics, the derived energy eigenvalues are directly incorporated into the partition function (Z) and subsequently used to determine other thermodynamic quantities, including vibrational mean energy (U), specific heat capacity (C), entropy (S), and free energy (F). Comparisons with previous studies are conducted. The classical case is recovered from the fractional case by setting $\alpha = \beta = 1$, consistent with prior work. Our results demonstrate that the fractional parameter plays a crucial role in governing the thermal and superstatistical properties within the framework of this model.

Keywords: *Schrödinger equation; Parametric Nikiforov-Uvarov method; Thermodynamic properties; Superstatics; Generalized fractional derivative*

PACS: 21.60.Cs, 03.65.Ge, 02.30.Gp, 24.10.Ht

1. INTRODUCTION

Over the last few decades, fractional calculus (FC) has attracted significant attention in a variety of scientific and engineering areas [1]. FC's prominence in several scientific and technical disciplines can be due to its benefits over numerical approaches, such as exact solutions and partial differential equations. Fractional differential equations are solved employing symmetry methods and perturbation analysis. In Ref. [2], the radial Schrödinger equation (SE) is solved analytically. Utilizing the conformable fractional variation of the Nikiforov-Uvarov (CF-NU) technique, the resulting dependent temperature potential in 3D and higher dimensions is used to determine the energy eigenvalues, correlated wave functions, and heavy quarkonium masses, such as charmonium and bottomonium, in a hot QCD medium. In Ref. [3], the conformable fractional derivative (CFD) method was used to investigate the fractional SE of a particle exhibiting position-dependent mass inside an infinite potential well.

Considering any dependent thermal potential, trigonometric Rosen-Morse potential [4], hot-magnetized interactions potential [5], and generalized Cornell potential [6], the distinctive features for heavy quarkonium were examined using the N-dimensional radial SE within the framework of the CFD. Hammed et al. [7] used the CF-NU technique to generate triaxial nuclei solutions for the CF Bohr Hamiltonian using the Kratzer potential. Based on the Fermi-Pasta-Ulam model, the authors investigated the time-dependent fraction fluctuation and the modified Gardner-type formula [8]. Abu-Shady and Kaabar proposed the generalized fractional derivative (GFD), which has more features than the earlier definitions [9]. Solving SE is a significant difficulty in quantum mechanics and particle physics for analyzing physical systems [10, 11, 12]. The fractional N-dimensional radial Schrödinger equation (SE) with the Deng–Fan potential (DFP) is investigated by the generalized fractional Nikiforov–Uvarov (NU) method [13].

Furthermore, as shown in Refs. [14, 15, 16], employing the NU technique allows for the exact solution of the SE and detailed system definition. This strategy outperforms previous methods, including those used in Ref. [17]. The Cornell potential and the expanded Cornell potential have already been used as in Refs. [24-28], applying wide methodologies including the NU method [22, 26, 29, 30]. Pekeris pattern prediction (PTA) [31, 32], the power series methodology (PST) [31], the asymptotic iteration procedure (AIM) [34], and the analysis of the exact iteration approach (AEIM) [33].

The thermodynamic features of quantum structures are crucial in quantum physics and the physical sciences. Analyzing characteristics such as entropy, specific heat capacity, mean energy, and free energy necessitates the partition function, which is dependent on temperature [17, 34, 35].

Numerous academics have recently become interested in using a range of quantum potential models to investigate the thermodynamic characteristics of systems. For instance, Edet et al. [36] investigated the thermal characteristics of the Deng-Fan Eckart potential model using the Poisson summation approach. Ikot et al. evaluated the thermodynamic properties of diatomic molecules with general molecular potential [37]. Onate [38] discovered the vibrational partition function, mean energy, vibrational specific heat capacity, and mean free energy in bound state formulations of the SE with the second Psychol-Teller-like potential. Within that paper, a hyperbolic variant of the Psychol-Teller-like potential was expressed. Numerous academics are interested in the practical use of the energy eigenvalue of the SE to study the partition function, thermodynamic properties, and superstatistics. Lately, Okon et al. [39] applied the NU technique to study the

thermodynamic characteristics and boundary phase formulations of two diatomic systems (carbon (II) oxide and scandium fluoride) using the Mobius square and screened Kratzer potential. Their findings agreed with those of semi-classical WKB and others. They used a close-form formulation of the energy eigenvalue to extract the partition function and other thermodynamic properties. Additionally, Oyewumi et al. [40] investigated the rotational-vibrational energy eigenvalues for diatomic systems employing the Pekeris-type approximated performance to centrifugal term and approximation solutions to the SE using the shifting Deng-Fan potential model within the asymptotic iteration framework. Furthermore, Boumali and Hassanabadi [41] investigated the thermal characteristics of a two-dimensional Dirac oscillator in the presence of an external magnetic field and discovered relativistic spin $\frac{1}{2}$ fermions influenced by Dirac oscillator coupling and a constant magnetic field in both computational and noncommutative spaces. In addition, properties of hadrons are investigated using the quark model as in Refs. [43, 44].

The main aim of the current work is to study the effect of the fractional parameter on superstatistics and thermal properties using the generalized fractional parametric NU method which, results in Ref. [47] being a special case of the present model at $\alpha = \beta = 1$.

The paper is organized as follows: In Section 1, the contributions of earlier works are presented. In Section 2, the generalized fractional derivative is introduced. In Section 3, the radial Schrodinger equation with parametric generalized differential NU method is introduced. In Sections 4 and 5, thermodynamic properties and superstatistics formulation are presented. In Sec. 6, results and discussion are explained. In Section 7, a conclusion is written.

2. THE GENERALIZED FRACTIONAL DERIVATIVE

The present study suggests the generalized fractional derivative (GFD): it is an alternative formula for a fractional derivative. Compared to other traditional Caputo and Riemann-Liouville fractional derivative definitions, the generalized fractional derivative has been proposed to offer greater benefits, such that the derivative of two functions, See Ref. [9] for a new approach to easily computing fractional differential formulas. For a function $Z: (0, \infty) \to R$, the generalized fractional derivative of order $0 < \alpha \le 1$ of $Z(t)$ at $t > 0$ is defined as

$$D^{GFD}Z(t) = \lim_{\varepsilon \to 0} \frac{Z\left(t + \frac{\Gamma(\beta)}{\Gamma(\beta-\alpha+1)}\varepsilon t^{1-\alpha}\right) - Z(t)}{\varepsilon}; \beta > -1, \beta \in R^+. \tag{1}$$

The generalized fractional derivative has the following characteristics:

$$D^{\alpha}[Z(t)] = k_1 t^{1-\alpha}\dot{Z}(t) \tag{2}$$

$$D^{\alpha}[D^{\alpha}Z(t)] = k_1^2\left[(1-\alpha)t^{1-2\alpha}\dot{Z}_{nl}(t) + t^{2-2\alpha}Z''(t)\right], \tag{3}$$

where:

$$k_1 = \frac{\Gamma[\beta]}{\Gamma[\beta-\alpha+1]}, \text{ with } 0 < \alpha \le 1, 0 < \beta \le 1, \tag{4}$$

$$D^{\alpha}D^{\beta}t^m = D^{\alpha+\beta}t^m \text{ for function derivative of } Z(t) = t^m, m \in R^+, \tag{5}$$

$$D^{GFD}(XY) = XD^{GFD}(Y) + YD^{GFD}(X) \text{ where } X, Y \text{ be } \alpha - \text{ differentiable function,} \tag{6}$$

$$D^{GFD}\left(\frac{X}{Y}\right) = \frac{YD^{GFD}(X) - XD^{GFD}(Y)}{Y^2} \text{ where } X, Y \text{ be } \alpha \text{ - differentiable function,} \tag{7}$$

$$D^{\alpha}I_{\alpha}Z(t) = Z(t) \text{ for } \ge 0 \text{ and } Z \text{ is any function within the domain that is continuous.} \tag{8}$$

2.1. The generalized fractional derivative with NU method

The parametric generalized fractional Nikiforov-Uvarov (NU) approach is introduced, making use of generalized fractional derivative. In the fractional structure as in Ref. [45], the second-order parametric generalized differential calculus is precisely computed.

$$D^{\alpha}[D^{\alpha}\psi(s)] + \frac{\bar{\tau}(s)}{\sigma(s)}D^{\alpha}\psi(s) + \frac{\bar{\sigma}(s)}{\sigma^2}\psi(s) = 0, \tag{9}$$

where $\bar{\sigma}(s), \sigma(s)$ and $\bar{\tau}(s)$ are polynomials of 2α-th, 2α-th and α-th degree.

$$\pi(s) = \frac{D^{\alpha}\sigma(s) - \bar{\tau}(s)}{2} \pm \sqrt{\left(\frac{D^{\alpha}\sigma(s) - \bar{\tau}(s)}{2}\right)^2 - \bar{\sigma}(s) + K_x\sigma(s)}, \tag{10}$$

and,

$$\lambda = K_x + D^{\alpha}\pi(s), \tag{11}$$

$\pi(s)$ is α-th degree polynomial, λ is constant. It is feasible to identify the quantities of K_x in the squareroot of Eq. (10), and therefore the formula within the square root is quadratic of expression. K_x is substituted for in Eq. (10), and we define.

$$\tau(s) = \bar{\tau}(s) + 2\pi(s). \tag{12}$$

Given that $\rho(s) > 0$ and $\sigma(s) > 0$, the derivative of τ is supposed to be negative in Ref. [46]. If λ in Eq. (11) be

$$\lambda = \lambda_n = -nD^\alpha\tau - \frac{n(n-1)}{2}D^\alpha[D^\alpha\sigma(s)]. \tag{13}$$

The solution of Eq. (3) is a combination of two independent components, and the hypergeometric type of equation has a distinctive solution with degree α.

$$\psi(s) = \phi(s)y(s), \tag{14}$$

wherein,

$$y_n(s) = \frac{B_n}{\rho(s)}(D^\alpha)^n(\sigma(s)^n\rho_n(s)), \tag{15}$$

$$D^\alpha[\sigma(s)\rho(s)] = \tau(s)\sigma(s), \tag{16}$$

$$\frac{D^\alpha\phi(s)}{\phi(s)} = \frac{\pi(s)}{\sigma(s)}. \tag{17}$$

2.2. Parametric Second Order Generalized Differential Equation

The fractional Schrödinger formula is expressed in a general form as in Ref. [42] that follows.

$$D^\alpha[D^\alpha\psi(s)] + \frac{\bar{\tau}(s)}{\sigma(s)}D^\alpha\psi(s) + \frac{\bar{\sigma}}{(\sigma(s))^2}\psi(s) = 0 \tag{18}$$

where:

$$\bar{\tau}(s) = \alpha_1 - \alpha_2 s^\alpha, \tag{19}$$

$$\sigma(s) = s^\alpha(1 - \alpha_3 s^\alpha), \tag{20}$$

$$\bar{\sigma}(s) = -\xi_1 s^{2\alpha} + \xi_2 s^\alpha - \xi_3 \tag{21}$$

Substituting Eqs. (19), (20), and (21) into Eq. (10), we obtain.

$$\pi = \alpha_4 + \alpha_5 s^\alpha \pm \sqrt{(\alpha_6 - K_x\alpha_3)s^{2\alpha} + (\alpha_7 + K_x)s^\alpha + \alpha_8} \tag{22}$$

where:

$$\alpha_4 = \frac{1}{2}(k_1\alpha - \alpha_1), \tag{23}$$

$$\alpha_5 = \frac{1}{2}(\alpha_2 - 2\alpha_3 k_1\alpha), \tag{24}$$

$$\alpha_6 = \alpha_5^2 + \xi_1, \tag{25}$$

$$\alpha_7 = 2\alpha_4\alpha_5 - \xi_2, \tag{26}$$

$$\alpha_8 = \alpha_4^2 + \xi_3, \tag{27}$$

According to the NU technique, the square of a polynomial must be the function under square root in Eq. (22), which implies.

$$K_x = -(\alpha_7 + 2\alpha_3\alpha_8) \pm 2\sqrt{\alpha_8\alpha_9}, \tag{28}$$

where:

$$\alpha_9 = \alpha_3\alpha_7 + \alpha_3^2\alpha_8 + \alpha_6. \tag{29}$$

In case K_x is negative then has the form

$$K_x = -(\alpha_7 + 2\alpha_3\alpha_8) - 2\sqrt{\alpha_8\alpha_9}. \tag{30}$$

So that π becomes.

$$\pi = \alpha_4 + \alpha_5 s^\alpha - [(\sqrt{\alpha_9} + \alpha_3\sqrt{\alpha_8})s^\alpha - \sqrt{\alpha_8}] \tag{31}$$

By using Eqs. (12), (22), and (31) then, we obtain.

$$\tau = \alpha_1 + 2\alpha_4 - (\alpha_2 - 2\alpha_5)s^\alpha - [(\sqrt{\alpha_9} + \alpha_3\sqrt{\alpha_8})s^\alpha - \sqrt{\alpha_8}] \tag{32}$$

From Eqs. (2), and (32), we get.

$$D^\alpha\tau = k_1[-\alpha(\alpha_2 - 2\alpha_5) - 2\alpha(\sqrt{\alpha_9} + \alpha_3\sqrt{\alpha_8})] = k_1[-2\alpha^2\alpha_3 - 2\alpha(\sqrt{\alpha_9} + \alpha_3\sqrt{\alpha_8})] < 0 \tag{33}$$

We construct the energy spectrum equation from Eqs. (11), and (13)

$$k_1\alpha\alpha_2 - (2n+1)k_1\alpha\alpha_5 + (2n+1)k_1\alpha\left(\sqrt{\alpha_9} + \alpha_3\sqrt{\alpha_8}\right) + n(n-1)k_1^2\alpha^2\alpha_3 + \alpha_7 + 2\alpha_3\alpha_8 + 2\sqrt{\alpha_8\alpha_9} = 0. \tag{34}$$

We obtain the standard formula of the energy eigenvalue as in Ref. [47], If $\alpha = \beta = 1$ then $k_1 = 1$,

$$n\alpha_2 - (2n+1)\alpha_5 + (2n+1)\left(\sqrt{\alpha_9} + \alpha_3\sqrt{\alpha_8}\right) + n(n-1)\alpha_3 + \alpha_7 + 2\alpha_3\alpha_8 + 2\sqrt{\alpha_8\alpha_9} = 0 \tag{35}$$

by using Eq. (16), we get

$$\rho(s) = s^{\frac{\alpha_{10}-\alpha}{k_1}}(1 - \alpha_3 s^\alpha)^{\frac{\alpha_{11}}{\alpha_1\alpha_3} - \frac{\alpha_{10}}{\alpha k_1} - \frac{1}{k_1}}. \tag{36}$$

From Eq. (15), we obtain.

$$y_n = P_n^{\left(\frac{\alpha_{10}-\alpha}{k_1}, \frac{\alpha_{11}}{\alpha k_1\alpha_3} - \frac{\alpha_{10}}{\alpha k_1} - \frac{1}{k_1}\right)}(1 - 2\alpha_3 s^\alpha) \tag{37}$$

where, L_n being the Laguerre polynomials, α_{10} and α_{11} becomes.

$$\alpha_{10} = \alpha_1 + 2\alpha_4 + 2\sqrt{\alpha_8}$$

$$\alpha_{11} = \alpha_2 - 2\alpha_5 + 2\left(\sqrt{\alpha_9} + \alpha_3\sqrt{\alpha_8}\right) \tag{38}$$

The fractional wave function is given by Eq. (14),

$$\psi(s) = s^{\frac{\alpha_{12}}{k_1}}(1 - \alpha_3 s^\alpha)^{\frac{-\alpha_{13}}{\alpha k_1\alpha_3} - \frac{\alpha_{12}}{\alpha k_1}} P_n^{\left(\frac{\alpha_{10}-\alpha}{k_1}, \frac{\alpha_{11}}{\alpha k_1\alpha_3} - \frac{\alpha_{10}}{\alpha k_1} - \frac{1}{k_1}\right)}(1 - 2\alpha_3 s^\alpha) \tag{39}$$

where, $P_n^{(\gamma,\delta)}$ are Jacobi polynomials and

$$\alpha_{12} = \alpha_4 + \sqrt{\alpha_8}$$

$$\alpha_{13} = \alpha_5 - \left(\sqrt{\alpha_9} + \alpha_3\sqrt{\alpha_8}\right) \tag{40}$$

Some problems, in case $\alpha_3 = 0$.

$$\lim_{\alpha_3 \to 0} P_n^{\left(\frac{\alpha_{10}-\alpha}{k_1}, \frac{\alpha_{11}}{\alpha k_1\alpha_3} - \frac{\alpha_{10}}{\alpha k_1} - \frac{1}{k_1}\right)}(1 - \alpha_3 s^\alpha) = L_n^{\frac{\alpha_{10}-\alpha}{k_1}}\left(\frac{\alpha_{11}}{\alpha k_1}s^\alpha\right) \tag{41}$$

$$\lim_{\alpha_3 \to 0}(1 - \alpha_3 s^\alpha)^{\frac{-\alpha_{13}}{\alpha k_1\alpha_3} - \frac{\alpha_{12}}{\alpha k_1}} = e^{\frac{\alpha_{13}}{\alpha k_1}s^\alpha} \tag{42}$$

Then Eq. (39), becomes.

$$\psi(s) = s^{\frac{\alpha_{12}}{k_1}} e^{\frac{\alpha_{13}}{\alpha k_1}s^\alpha} L_n^{\frac{\alpha_{10}-\alpha}{k_1}}\left(\frac{\alpha_{11}}{\alpha k_1}s^\alpha\right) \tag{43}$$

where, L_n being the Laguerre polynomials, and K_x becomes.

$$K_x = -(\alpha_7 + 2\alpha_3\alpha_8) + 2\sqrt{\alpha_8\alpha_9} \tag{44}$$

then, the wave function is,

$$\psi(s) = s^{\frac{\alpha_{12^*}}{k_1}}(1 - \alpha_3 s^\alpha)^{\frac{-\alpha_{13^*}}{\alpha_1\alpha_3} - \frac{\alpha_{12^*}}{\alpha k_1}} P_n^{\left(\frac{\alpha_{10^*}-\alpha}{k_1}, \frac{\alpha_{11^*}}{\alpha k_1\alpha_3} - \frac{\alpha_{10^*}}{\alpha k_1} - \frac{1}{k_1}\right)} \times (1 - 2\alpha_3 s^\alpha), \tag{45}$$

The fractional energy eigenvalue formula is given:

$$nk_1\alpha\alpha_2 - 2nk_1\alpha\alpha_5 + (2n+1)k_1\alpha\left(\sqrt{\alpha_9} - \alpha_3\sqrt{\alpha_8}\right) + n(n-1)k_1^2\alpha^2\alpha_3 + \alpha_7 + 2\alpha_3\alpha_8 - 2\sqrt{\alpha_8\alpha_9} + k_1\alpha\alpha_5 = 0 \tag{46}$$

where:

$$\alpha_{10^*} = \alpha_1 + 2\alpha_4 - 2\sqrt{\alpha_8}, \tag{47}$$

$$\alpha_{11^*} = \alpha_2 - 2\alpha_5 + 2\left(\sqrt{\alpha_9} - \alpha_3\sqrt{\alpha_8}\right), \tag{48}$$

$$\alpha_{12^*} = \alpha_4 - \sqrt{\alpha_8}, \tag{49}$$

$$\alpha_{13}^* = \alpha_5 - \left(\sqrt{\alpha_9} - \alpha_3\sqrt{\alpha_8}\right). \tag{50}$$

3. THE RADIAL SCHRODINGER EQUATION WITH PARAMETRIC GENERALIZED DIFFERENTIAL NU METHOD

The suggested Coulomb plus screened hyperbolic exponential potential (CPSHEP) [47] is presented so as.

$$V(r) = -\frac{v_1}{r} + \left(\frac{B}{r} - \frac{v_2 \cosh \alpha_x}{r^2}\right) e^{-\alpha_x r} \tag{51}$$

where α_x is the adjustable screening parameter, B is a real constant parameter, and v_1 and v_2 are the potential depths. This is the centrifugal term's Pekeris-like approximation:

$$\frac{1}{r^2} = \frac{\alpha_x^2}{(1-e^{-\alpha_x r})^2} \Rightarrow \frac{1}{r} = \frac{\alpha_x}{(1-e^{-\alpha_x r})}. \tag{52}$$

by substituting Eq. (52) to Eq. (51), then we obtain the approximation form of the mentioned potential as follows.

$$V(r) = -\frac{v_1 \alpha_x}{(1-e^{-\alpha_x r})} + \left(\frac{B\alpha_x}{(1-e^{-\alpha_x r})} - \frac{v_2 \alpha_x^2 \cosh \alpha_x}{(1-e^{-\alpha_x r})^2}\right) e^{-\alpha_x r} \tag{53}$$

The radial Schrödinger equation with the centrifugal term is given as follows.

$$\frac{d^2 R(r)}{dr^2} + \frac{2\mu}{\hbar^2} \cdot \left\{E - V(r) - \frac{\hbar^2 \, l(l+1)}{2\mu \, r^2}\right\} R(r) = 0 \tag{54}$$

The exact solution to Eq. (54) can only be obtained through an analytical solution when the angular orbital quantum number $l = 0$. Nevertheless, Eq. (54) can only be solved for $l > 0$ by applying the centrifugal term estimates in Eq. (52). Eq. (51) can be substituted into Eq. (54) to yield.

$$\frac{d^2 R(r)}{dr^2} + \frac{2\mu}{\hbar^2} \cdot \left\{E + \frac{v_1}{r} - \frac{B \, e^{-\alpha_x r}}{r} + \frac{v_2 \, e^{-\alpha_x r} \cosh \alpha_x}{r^2} - \frac{\hbar^2 \, l(l+1)}{2\mu \, r^2}\right\} R(r) = 0 \tag{55}$$

Eq. (52) can be substituted into Eq. (55) to obtain the following equation:

$$\frac{d^2 R(r)}{dr^2} + \frac{2\mu}{\hbar^2} \cdot \left\{E + \frac{v_1 \alpha_x}{(1-e^{-\alpha_x r})} - \frac{B \alpha_x \, e^{-\alpha_x r}}{(1-e^{-\alpha_x r})} + \frac{v_2 \alpha_x^2 \, e^{-\alpha_x r} \cosh \alpha_x}{(1-e^{-\alpha_x r})^2} - \frac{\hbar^2 \alpha_x^2 \, l(l+1)}{2\mu \, (1-e^{-\alpha_x r})^2}\right\} R(r) = 0 \tag{56}$$

With a little mathematical simplification and a definition of s$= e^{-\alpha_x r}$, Eq. (56) will be expressed as follows.

$$\frac{d^2 R(s)}{ds^2} + \frac{(1-s)}{s(1-s)} \frac{dR}{ds} + \frac{1}{s^2(1-s)^2} \cdot \left\{\begin{array}{c} -(\varepsilon^2 - \chi_1)s^2 \\ +(2\varepsilon^2 - \delta^2 - \chi_1 + \chi_2)s \\ -(\varepsilon^2 - \delta^2 + l(l+1)) \end{array}\right\} R(s) = 0 \tag{57}$$

where,

$$\varepsilon^2 = -\frac{2\mu E_{nl}}{\hbar^2 \alpha_x^2}, \delta^2 = \frac{2\mu v_1}{\hbar^2 \alpha_x}, \chi_1 = \frac{2\mu B}{\hbar^2 \alpha_x}, \chi_2 = \frac{2\mu v_2 \cosh \alpha_x}{\hbar^2}, s = e^{-\alpha_x r}. \tag{58}$$

Consequently, we obtain the generalized fractional radial constituent of the Schrödinger equation [49] as follows.

$$D^\alpha[D^\alpha R(s)] + \frac{1-s^\alpha}{s^\alpha(1-s^\alpha)} D^\alpha R(s) + \frac{-\xi_1 s^{2\alpha} + \xi_2 s^\alpha - \xi_3}{\left(s^\alpha(1-s^\alpha)\right)^2} R(s) = 0 \tag{59}$$

Comparing Eq. (57) to Eq. (59), the following polynomials were obtained:

$$\xi_1 = (\varepsilon^2 - \chi_1), \xi_2 = (2\varepsilon^2 - \delta^2 - \chi_1 + \chi_2), \xi_3 = \varepsilon^2 - \delta^2 + l(l+1) \tag{60}$$

Using Eqs. (10), (12), from Eq. (19) to Eq. (40), other parametric constants are obtained as follows:

$$\alpha_1 = \alpha_2 = \alpha_3 = 1, \alpha_4 = \frac{1}{2}(k_1 \alpha - 1). \tag{61}$$

$$\alpha_5 = \frac{1}{2}(1 - 2k_1 \alpha), \alpha_6 = \frac{1}{4}(1 - 2k_1 \alpha)^2 - \frac{2\mu E_{nl}}{\hbar^2 \alpha_x^2} - \frac{2\mu B}{\hbar^2 \alpha_x}. \tag{62}$$

$$\alpha_7 = \frac{1}{2}(k_1 \alpha - 1)(1 - 2k_1 \alpha) - 2 - \frac{2\mu E_{nl}}{\hbar^2 \alpha_x^2} + \frac{2\mu v_1}{\hbar^2 \alpha_x} + \frac{2\mu B}{\hbar^2 \alpha_x} - \frac{2\mu v_2 \cosh \alpha_x}{\hbar^2}. \tag{63}$$

$$\alpha_8 = \frac{1}{4}(k_1 \alpha - 1)^2 - \frac{2\mu E_{nl}}{\hbar^2 \alpha_x^2} - \frac{2\mu v_1}{\hbar^2 \alpha_x}, \alpha_9 = \frac{1}{4}k_1^2 \alpha^2 - \frac{2\mu v_2 \cosh \alpha_x}{\hbar^2} + l(l+1). \tag{64}$$

$$\alpha_{10} = k_1 \alpha + 2\sqrt{\frac{1}{4}(k_1 \alpha - 1)^2 - \frac{2\mu E_{nl}}{\hbar^2 \alpha_x^2} - \frac{2\mu v_1}{\hbar^2 \alpha_x} + l(l+1)}. \tag{65}$$

$$\alpha_{11} = 2k_1 \alpha + 2\sqrt{\frac{1}{4}k_1^2 \alpha^2 - \frac{2\mu v_2 \cosh \alpha_x}{\hbar^2} + l(l+1)} + \sqrt{\frac{1}{4}(k_1 \alpha - 1)^2 - \frac{2\mu E_{nl}}{\hbar^2 \alpha_x^2} - \frac{2\mu v_1}{\hbar^2 \alpha_x} + l(l+1)}. \tag{67}$$

$$\alpha_{12} = \frac{1}{2}(k_1 \alpha - 1) + \sqrt{\frac{1}{4}(k_1 \alpha - 1)^2 - \frac{2\mu E_{nl}}{\hbar^2 \alpha_x^2} - \frac{2\mu v_1}{\hbar^2 \alpha_x} + l(l+1)} \tag{68}$$

$$\alpha_{13} = \frac{1}{2}(1 - 2k_1 \alpha) - \frac{1}{2}\sqrt{k_1^2 \alpha^2 - \frac{2\mu v_2 \cosh \alpha_x}{\hbar^2} - l(l+1)} + \sqrt{\frac{1}{4}(k_1 \alpha - 1)^2 - \frac{2\mu E_{nl}}{\hbar^2 \alpha_x^2} - \frac{2\mu v_1}{\hbar^2 \alpha_x} + l(l+1)} \tag{69}$$

The energy eigenvalue in the fractional form for the present potential can be determined by Eqs. (34), (60), and from Eq. (19) to Eq. (40) with considerable algebraic simplification as follows.

$$E_{nl} = \frac{\hbar^2 \alpha_x^2 l(l+1)}{2\mu} - v_1 \alpha_x + \frac{\hbar^2 \alpha_x^2 (k_1 \alpha - 1)^2}{8\mu} + \frac{\hbar^2 \alpha_x^2}{2\mu} * \left\{ \frac{F_1 + F_2 + F_3}{k_1 \alpha * (2n+1) + \sqrt{K_1^2 \alpha^2 + 4l(l+1) - (8v_2 \mu \cosh \alpha_x / \hbar^2)}} \right\}^2 \tag{70}$$

we can get the classical case from Eq. (70) at $\alpha = \beta = 1$, then $k_1 = 1$ [47], as the following equation.

$$E_{nl} = \frac{\hbar^2 \alpha_x^2 l(l+1)}{2\mu} - v_1 \alpha_x + \frac{\hbar^2 \alpha_x^2}{2\mu} * \left\{ \frac{F_4 + F_5 + F_6}{(2n+1) + \sqrt{1 + 4l(l+1) - \left(\frac{8v_2 \mu \cosh \alpha_x}{\hbar^2}\right)}} \right\}^2 \tag{71}$$

where:

$$F_1 = k_1^2 \alpha^2 (n^2 + n + (1/2)). \tag{72}$$

$$F_2 = k_1 \alpha * (n + (1/2))\sqrt{k_1^2 \alpha^2 + 4l(l+1) - (8v_2 \mu \cosh \alpha_x / \hbar^2)}. \tag{73}$$

$$F_3 = (2\mu B/\hbar^2 \alpha_x) - \left(\frac{2\mu v_1}{\hbar^2 \alpha_x}\right) - \left(\frac{2v_2 \mu \cosh \alpha_x}{\hbar^2}\right) + 2l(l+1). \tag{74}$$

$$F_4 = (n^2 + n + (1/2)). \tag{75}$$

$$F_5 = \left(n + \left(\frac{1}{2}\right)\right)\sqrt{1 + 4l(l+1) - \left(\frac{8v_2 \mu \cosh \alpha_x}{\hbar^2}\right)}. \tag{76}$$

$$F_6 = (2\mu B/\hbar^2 \alpha_x) - \left(\frac{2\mu v_1}{\hbar^2 \alpha_x}\right) - \left(\frac{2v_2 \mu \cosh \alpha_x}{\hbar^2}\right) + 2l(l+1). \tag{77}$$

The generalized fractional of the total wave function using Eqs. [38-40], is given as

$$\Psi_{nl}(s) = N_{nl} s^{(F_7)} * (1 - s^\alpha)^{(F_8 + F_9)} * P_n^{\left(F_{10}, F_{11} + F_{12} - \frac{1}{k_1}\right)} * (1 - 2s^\alpha). \tag{78}$$

$$F_7 = \frac{\frac{1}{2}(k_1 \alpha - 1) + \sqrt{\frac{1}{4}(k_1 \alpha - 1)^2 - \frac{2\mu E_{nl}}{\hbar^2 \alpha_x^2} - \frac{2\mu v_1}{\hbar^2 \alpha_x} + l(l+1)}}{k_1}. \tag{79}$$

$$F_8 = -\left(\frac{1}{2}(1 - 2k_1 \alpha) - \frac{1}{2}\sqrt{k_1^2 \alpha^2 - \frac{2\mu v_2 \cosh \alpha_x}{\hbar^2} - l(l+1)} + \frac{\sqrt{\frac{1}{4}(k_1 \alpha - 1)^2 - \frac{2\mu E_{nl}}{\hbar^2 \alpha_x^2} - \frac{2\mu v_1}{\hbar^2 \alpha_x} + l(l+1)}}{\alpha k_1}\right) \tag{80}$$

$$F_9 = -\frac{\frac{1}{2}(k_1 \alpha - 1) + \sqrt{\frac{1}{4}(k_1 \alpha - 1)^2 - \frac{2\mu E_{nl}}{\hbar^2 \alpha_x^2} - \frac{2\mu v_1}{\hbar^2 \alpha_x} + l(l+1)}}{\alpha k_1} \tag{81}$$

$$F_{10} = \frac{k_1 \alpha + 2\sqrt{\frac{1}{4}(k_1 \alpha - 1)^2 - \frac{2\mu E_{nl}}{\hbar^2 \alpha_x^2} - \frac{2\mu v_1}{\hbar^2 \alpha_x} + l(l+1)} - \alpha}{k_1} \tag{82}$$

$$F_{11} = 2k_1 \alpha + 2\sqrt{\frac{1}{4}k_1^2 \alpha^2 - \frac{2\mu v_2 \cosh \alpha_x}{\hbar^2} + l(l+1)} + \sqrt{\frac{1}{4}(k_1 \alpha - 1)^2 - \frac{2\mu E_{nl}}{\hbar^2 \alpha_x^2} - \frac{2\mu v_1}{\hbar^2 \alpha_x} + l(l+1)}. \tag{83}$$

$$F_{12} = -\frac{k_1 \alpha + 2\sqrt{\frac{1}{4}(k_1 \alpha - 1)^2 - \frac{2\mu E_{nl}}{\hbar^2 \alpha_x^2} - \frac{2\mu v_1}{\hbar^2 \alpha_x} + l(l+1)}}{\alpha k_1}. \tag{84}$$

The special case of the total un-normalized wave function at $\alpha = \beta = 1$ then $k_1 = 1$, as in agreement with [47] as following.

$$\Psi_{nl}(s) = N_{nl} s^{\sqrt{(\varepsilon^2 - \delta^2 + l(l+1))}} (1s)^{-\frac{1}{2} - 2\sqrt{(\varepsilon^2 - \delta^2 + l(l+1))} - \frac{1}{2}\sqrt{1 + 4l(l+1) - 4\chi_2}} P_n^{\left[\left(2\sqrt{(\varepsilon^2 - \delta^2 + l(l+1))}\right) \cdot \left(\sqrt{(1 + 4l(l+1) - 4\chi_2)}\right)\right]} (1 - 2s) \tag{85}$$

4. THERMODYNAMIC PROPERTIES

In this section, we describe the potential model's thermodynamic properties. The partition function offered can be used to determine the thermodynamic characteristics of quantum systems as follows.

$$Z(\beta_1) = \sum_{n=0}^{\lambda} e^{-\beta_1 E_n}, \tag{86}$$

where λ is an upper constraint on the vibrational quantum number determined by the numerical solution of $dE_n/dn = 0$, expressed as $\lambda = \frac{1}{k_1\alpha}\left(-\delta + \sqrt{\delta(k_1\alpha - \delta) + Q_3}\right), \beta_1 = 1/KT$, where K and T are the Boltzmann constant and absolute temperature, correspondingly. The integral in Eq. (87) may substitute the place of the summation in the classical limit.

$$Z(\beta_1) = \int_0^{\lambda} e^{-\beta_1 E_n} dn \tag{87}$$

The energy eigenvalue equation as in Eq. (70) can be expressed in a concise form as follows to yield the partition functions.

$$E_{nl} = Q_1 + Q_2 * \left\{\frac{(k_1\alpha n + \delta)}{2} + \frac{\delta(k_1\alpha - \delta) + Q_3}{2(k_1\alpha n + \delta)}\right\}^2, \tag{88}$$

where:

$$Q_1 = \frac{\hbar^2\alpha_x^2 l(l+1)}{2\mu} - v_1\alpha + \frac{\hbar^2\alpha_x^2(k_1\alpha-1)^2}{8\mu}, Q_2 = \frac{\hbar^2\alpha_x^2}{2\mu},$$
$$Q_3 = \left(\frac{2\mu B}{\hbar^2\alpha_x}\right) - \left(\frac{2\mu v_1}{\hbar^2\alpha_x}\right) - \left(\frac{2v_2\mu\cosh\alpha_x}{\hbar^2}\right) + 2l(l+1),$$

$$\delta = \frac{1}{2}k_1\alpha + \sqrt{\frac{1}{4}k_1^2\alpha^2 - \frac{2v_2\mu\cosh\alpha_x}{\hbar^2} + l(l+1)}. \tag{89}$$

The following form can be used to represent Eq. (88) as follows.

$$E_{nl} = \left(Q_1 + \frac{Q_2(\delta(k_1\alpha-\delta)+Q_3)}{2}\right) + \left(\frac{Q_2\rho^2}{4} + \frac{Q_2(\delta(k_1\alpha-\delta)+Q_3)^2}{4\rho^2}\right). \tag{90}$$

where:

$$\rho = k_1\alpha n + \delta \tag{91}$$

(i) Partition function is obtained by inserting Eq. (90) to Eq. (87) and noting modifications to the integration boundaries utilizing Eq. (91)

$$Z(\beta_1) = e^{-\beta_1\left(Q_1 + \frac{Q_2(\delta(k_1\alpha-\delta)+Q_3)}{2}\right)} \int_{\delta}^{k_1\alpha\lambda+\delta} e^{\beta_1\left(\frac{Q_2\rho^2}{4} + \frac{Q_2(\delta(k_1\alpha-\delta)+Q_3)^2}{4\rho^2}\right)} d\rho. \tag{92}$$

The partition function of Eq. (92) is obtained as

$$Z(\beta_1) = \frac{(\sqrt{\pi}e^{-\frac{1}{2}\beta_1\left(NQ_2+NN_0^2+2Q_1\right)}(\text{erf}(\sqrt{\beta_1}\Lambda_1)+\text{erf}(\sqrt{\beta_1}\Lambda_3))-e^{\beta_1 NN_0^2\,\text{erf}(\sqrt{\beta_1}\Lambda_2)+e^{\beta_1 NN_0^2}\text{erf}(\sqrt{\beta_1}\Lambda_4)})}{2\sqrt{\beta_1}N_0}. \tag{93}$$

(ii) Vibrational free energy is given as follows.

$$F(\beta_1) = -\frac{1}{\beta_1}\ln Z(\beta_1). \tag{94}$$

$$F(\beta_1) = -\frac{\log\left(\frac{\sqrt{\pi}e^{-\frac{1}{2}\beta_1\left(NQ_2+NN_0^2+2Q_1\right)}(\text{erf}(\sqrt{\beta_1}\Lambda_1)+\text{erf}(\sqrt{\beta_1}\Lambda_3))-e^{\beta_1 NN_0^2\text{erf}(\sqrt{\beta_1}\Lambda_2)+e^{\beta_1 NN_0^2}\text{erf}(\sqrt{\beta_1}\Lambda_4)}}{2\sqrt{\beta_1}N_0}\right)}{\beta_1} \tag{95}$$

(iii) Vibrational mean energy is given as follows.

$$U(\beta_1) = -\frac{d}{d\beta_1}\ln Z(\beta_1), \tag{96}$$

$$U(\beta_1) = \frac{1}{2}\left(\frac{1}{\beta_1} - \Omega + NQ_2 + NN_0^2 + 2Q_1\right), \tag{97}$$

$$\Omega = \frac{2(F_{13}-F_{14})}{\sqrt{\pi}\sqrt{\beta_1}\left(\text{erf}\left(\sqrt{\beta_1}\Lambda_1\right)+\text{erf}\left(\sqrt{\beta_1}\Lambda_3\right)-e^{\beta_1 NN_0^2}\text{erf}\left(\sqrt{\beta_1}\Lambda_2\right)+e^{\beta_1 NN_0^2}\text{erf}\left(\sqrt{\beta_1}\Lambda_4\right)\right)}, \tag{98}$$

$$F_{13} = \Lambda_1 e^{-\beta_1\Lambda_1^2} + \Lambda_3 e^{-\beta_1\Lambda_3^2} + \sqrt{\pi}\sqrt{\beta_1}NN_0^2\left(-e^{\beta_1 NN_0^2}\right)\left(\text{erf}\left(\sqrt{\beta_1}\Lambda_2\right) - \text{erf}\left(\sqrt{\beta_1}\Lambda_4\right)\right), \tag{99}$$

$$F_{14} = -\Lambda_2 e^{\beta_1\left(NN_0^2-\Lambda_2^2\right)} + \Lambda_4 e^{\beta_1\left(NN_0^2-\Lambda_4^2\right)}. \tag{100}$$

(iv) Vibrational entropy is given as follows.

$$S(\beta_1) = K\ln Z(\beta_1) + K\beta_1\frac{d}{d\beta_1}\ln Z(\beta_1), \tag{101}$$

$$S(\beta_1) = K\left(\frac{\sqrt{\beta_1}(F_{15}+F_{16})}{F_{17}} + \log(F_{18}) + \frac{1}{2}\beta_1(NQ_2 + NN_0^2 + 2Q_1) + \frac{1}{2}\right), \tag{102}$$

$$F_{15} = -\Lambda_1 e^{-\beta_1\Lambda_1^2} - \Lambda_3 e^{-\beta_1\Lambda_3^2} + \sqrt{\pi}\sqrt{\beta_1}NN_0^2 e^{\beta_1 NN_0^2}\left(\text{erf}\left(\sqrt{\beta_1}\Lambda_2\right) - \text{erf}\left(\sqrt{\beta_1}\Lambda_4\right)\right)), \tag{103}$$

$$F_{16} = \Lambda_2 e^{\beta_1(NN_0^2 - \Lambda_2^2)} - \Lambda_4 e^{\beta_1(NN_0^2 - \Lambda_4^2)}, \tag{104}$$

$$F_{17} = \pi\left(\text{erf}(\sqrt{\beta_1}\Lambda_1) + \text{erf}(\sqrt{\beta_1}\Lambda_3) - e^{\beta_1 NN_0^2}\text{erf}(\sqrt{\beta_1}\Lambda_2) + e^{\beta_1 NN_0^2}\text{erf}\left(\sqrt{\beta_1}\Lambda_4\right)\right), \tag{105}$$

$$F_{18} = \frac{\sqrt{\pi}e^{-\frac{1}{2}\beta_1(NQ_2+NN_0^2+2Q_1)}\left(\begin{array}{c}\text{erf}(\sqrt{\beta_1}\Lambda_1)+\text{erf}(\sqrt{\beta_1}\Lambda_3)\\ -e^{\beta_1 NN_0^2}\text{erf}(\sqrt{\beta_1}\Lambda_2)+e^{\beta_1 NN_0^2}\text{erf}(\sqrt{\beta_1}\Lambda_4)\end{array}\right)}{2\sqrt{\beta_1}N_0}. \tag{106}$$

(v) Vibrational specific heat capacity is given as follows.

$$C(\beta_1) = -K\beta_1^2 \frac{dU(\beta_1)}{d\beta_1}. \tag{107}$$

$$C(\beta_1) = \frac{1}{2}K\left(\frac{2\beta_1^{3/2}(F_{19}+F_{20})}{F_{21}} - \frac{\sqrt{\beta_1}(F_{22})}{F_{21}} - \frac{2e^{-2\beta_1(\Lambda_1^2+\Lambda_2^2+\Lambda_3^2+\Lambda_4^2)}\beta_1(F_{23})^2}{\pi(F_{21})^2} + 1\right). \tag{108}$$

$$F_{19} = -e^{NN_0^2\beta_1}N^2\left(\text{erf}(\sqrt{\beta_1}\Lambda_2) - \text{erf}(\sqrt{\beta_1}\Lambda_4)\right)\sqrt{\pi}\sqrt{\beta_1}N_0^4 +$$
$$\frac{1}{2}e^{NN_0^2\beta_1}N\left(\frac{(\text{erf}(\sqrt{\beta_1}\Lambda_4)-\text{erf}(\sqrt{\beta_1}\Lambda_2))\sqrt{\pi}}{\sqrt{\beta_1}} - 4e^{-\beta_1\Lambda_2^2}\Lambda_2 + 4e^{-\beta_1\Lambda_4^2}\Lambda_4\right)N_0^2 - e^{-\beta_1\Lambda_1^2}\Lambda_1^3 \tag{109}$$

$$F_{20} = e^{\beta_1(NN_0^2-\Lambda_2^2)}\Lambda_2^3 - e^{-\beta_1\Lambda_3^2}\Lambda_3^3 - e^{\beta_1(NN_0^2-\Lambda_4^2)}\Lambda_4^3. \tag{110}$$

$$F_{21} = \sqrt{\pi}\left(\text{erf}\left(\sqrt{\beta_1}\Lambda_1\right) - e^{NN_0^2\beta_1}\text{erf}\left(\sqrt{\beta_1}\Lambda_2\right) + \text{erf}\left(\sqrt{\beta_1}\Lambda_3\right) + e^{NN_0^2\beta_1}\text{erf}\left(\sqrt{\beta_1}\Lambda_4\right)\right) \tag{111}$$

$$F_{22} = -e^{NN_0^2\beta_1}N\left(\text{erf}\left(\sqrt{\beta_1}\Lambda_2\right) - \text{erf}\left(\sqrt{\beta_1}\Lambda_4\right)\right)\sqrt{\pi}\sqrt{\beta_1}N_0^2 + e^{-\beta_1\Lambda_1^2}\Lambda_1 -$$
$$e^{\beta_1(NN_0^2-\Lambda_2^2)}\Lambda_2 + e^{-\beta_1\Lambda_3^2}\Lambda_3 + e^{\beta_1(NN_0^2-\Lambda_4^2)}\Lambda_4. \tag{112}$$

$$F_{23} = -e^{\beta_1(NN_0^2+\Lambda_1^2+\Lambda_2^2+\Lambda_3^2+\Lambda_4^2)}N\left(\text{erf}\left(\sqrt{\beta_1}\Lambda_2\right) - \text{erf}\left(\sqrt{\beta_1}\Lambda_4\right)\right)\sqrt{\pi}\sqrt{\beta_1}N_0^2 +$$
$$e^{\beta_1(\Lambda_2^2+\Lambda_3^2+\Lambda_4^2)}\Lambda_1 - e^{\beta_1(NN_0^2+\Lambda_1^2+\Lambda_3^2+\Lambda_4^2)}\Lambda_2 + e^{\beta_1(\Lambda_1^2+\Lambda_2^2+\Lambda_4^2)}\Lambda_3 + e^{\beta_1(NN_0^2+\Lambda_1^2+\Lambda_2^2+\Lambda_3^2)}\Lambda_4. \tag{113}$$

where:

$$N = Q_2(\delta(\alpha k_1 - \delta) + Q_3)^2, N_0 = \sqrt{-Q_2}, \Lambda_1 = \frac{N_0(N-\delta^2)}{2\delta}. \tag{114}$$

$$\Lambda_2 = \frac{N_0(\delta^2+N)}{2\delta}, \Lambda_3 = \frac{N_0((\delta+\alpha k_1\lambda)^2-N)}{2(\delta+\alpha k_1\lambda)}, \Lambda_4 = \frac{N_0((\delta+\alpha k_1\lambda)^2+N)}{2(\delta+\alpha k_1\lambda)} \tag{115}$$

5. SUPERSTATISTICS FORMULATION

Superstatistics represents a statistical concept that applies to dynamic nonequilibrium systems and statistically intense variable (β_1) variation [49]. Chemical potential and energy fluctuation, which are primarily described in terms of the effectual Boltzmann variable, are included in this extensive parameter that experiences spatiotemporal volatility [50]. Apparently, Edet et al. [51], present the actual Boltzmann factor as follow.

$$B(E) = \int_0^\infty e^{-\beta_1' E}f(\beta_1', \beta_1)d\beta_1'. \tag{116}$$

where $f(\beta_1', \beta_1) = \delta(\beta_1 - \beta_1')$ is the Dirac delta function.

The generalized Boltzmann constant is given as the following when stated in terms of the deformation parameter q:

$$B(E) = e^{-\beta_1 E}\left(1 + \frac{q}{2}\beta_1^2 E^2\right). \tag{117}$$

The partition function for superstatistics formalism is then provided as

$$Z_s = \int_0^\infty B(E)dn. \tag{118}$$

The modified Boltzmann constant equation is presented as when Eq. (90) is substituted into Eq. (117).

$$B(E) = \left[\frac{q}{2}\beta_1^2\left(\left(Q_1 + \frac{Q_2(\delta(k_1\alpha-\delta)+Q_3)}{2}\right) + \left(\frac{Q_2\rho^2}{4}\right) + \frac{Q_2(\delta(k_1\alpha-\delta)+Q_3)^2}{4\rho^2}\right)^2\right] * e^{-\beta_1\left[\left(Q_1+\frac{Q_2(\delta(k_1\alpha-\delta)+Q_3)}{2}\right)+\left(\frac{Q_2\rho^2}{4}+\frac{Q_2(\delta(k_1\alpha-\delta)+Q_3)^2}{4\rho^2}\right)\right]}. \quad (119)$$

Using Eq. (118), the superstatistics partition function equation is given as.

$$Z_s(\beta_1) = e^{\beta_1\left(Q_1+\frac{Q_2(\delta(k_1\alpha-\delta)+Q_3)}{2}\right)}\int_0^\infty\left[1 + \frac{q}{2}\beta_1^2\left(\left(Q_1 + \frac{Q_2(\delta(k_1\alpha-\delta)+Q_3)}{2}\right) + \left(\frac{Q_2\rho^2}{4}\right) + \frac{Q_2(\delta(k_1\alpha-\delta)+Q_3)^2}{4\rho^2}\right)^2\right] * e^{\beta_1\left(\frac{Q_2\rho^2}{4}+\frac{Q_2(\delta(k_1\alpha-\delta)+Q_3)^2}{4\rho^2}\right)}d\rho \quad (120)$$

The partition for superstatistics obtained from Eq. (120), is given as.

$$Z_s(\beta_1) = \frac{\sqrt{\pi}\sqrt{\frac{1}{\beta_1}}\beta_1^{3/2}e^{-\frac{1}{2}\beta_1(NQ_2+NN_0^2+2Q_1)}\left(Q_2(\beta_1^2q(NQ_2+2Q_1)+4)-\beta_1qQ_2\left(\sqrt{\frac{1}{\beta_1}}\beta_1^{3/2}NN_0^2+1\right)\right)}{4(\beta_1(-Q_2))^{3/2}}. \quad (121)$$

where:

$$F_s(\beta_1) = -\frac{\ln(Z_s)}{\beta_1}, \quad (122)$$

$$U_s(\beta_1) = -\frac{\partial\ln(Z_s)}{\partial\beta_1}, \quad (123)$$

$$S_s(\beta_1) = K\ln(Z_s) - \beta_1 K\frac{\partial(\ln(Z_s))}{\partial\beta_1}, \quad (124)$$

$$C_s(\beta_1) = -K\beta_1^2\frac{\partial U_s}{\partial\beta_1}. \quad (125)$$

6. RESULTS AND DISCUSSION

We plotted all figures using the following parameters $\beta_1 = \frac{1}{KT}$, and K is the Boltzmann constant. When the principal quantum number n is around 0 and 1,2, ..., λ, and μ is the reduced mass for quarkonium as $= \frac{m_1*m_2}{m_1+m_2}$. In Fig. 1 (left panel), the suggested coulomb plus screened hyperbolic exponential potential (CPSHEP) and an approximation one is plotted according to two characteristics: the coulomb potential and confinement potential characterize the short and long distances, respectively. The approximate potential is brief, with the actual potential reaching 0.8 fm. We plotted the Pekeris approximation graph compared to the screening parameter α_x as shown in Fig. 1(the right panel), since the approximation fits the anticipated potential.
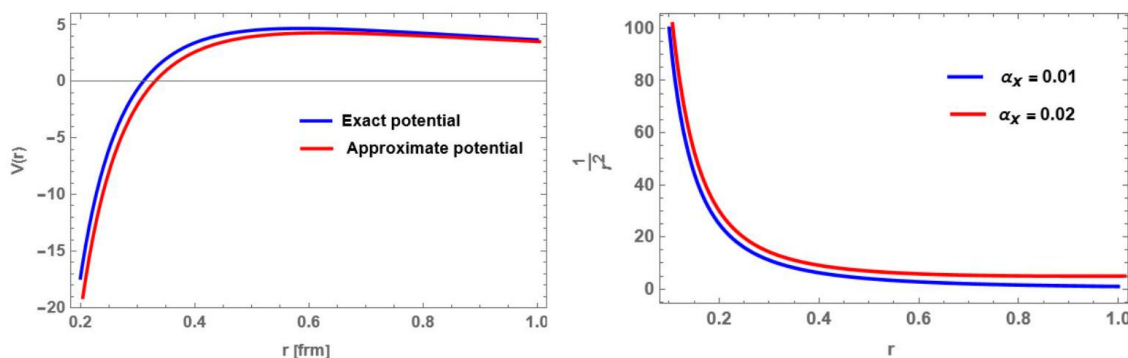
Figure 1. (the left panel), the potential $V(r)$ of the exact potential via approximation potential are drawn as a function of distance (r) at $\alpha_x = 0.2$, (the right panel), the graph of Pekeris approximation for various values of α_x.

In Fig. (2), it shows how the temperature parameter affects the partition function for thermodynamic properties and superstatics. In this case, the partition function grows nonlinearly with β_1 whereas, the partition function in Fig. 2 (the left panel), deviated as increased, it later converged for the superstatistics, as seen in Figure. 2 (The left panel). As can be seen, the partition function (Z) is delicate at the highest values of β_1, the range of β_1 between 4GeV^{-1} and 7GeV^{-1} correlates with T between 0.142 and 0.25GeV. Additionally, it needs to be observed that as fractional parameters α and β are increased, the curve's conduct becomes lower. In Fig. 2 (the right panel) (superstatics), it can also be seen that the partition function converging as acquires higher values of β_1, also by increasing deformation parameter q then curves become higher, deformation parameter q improves the behavior of superstatics. The behavior of $Z_s(\beta_1)$ is compatible with Ref. [52]. In Ref. [53], the ground state is shown as the node with the highest value on the probability density diagram. Temperature and the Z's behavior in relation to the largest possible quantum number(λ). In addition, as the quantum number (λ) increases, Z decreases simultaneously increasing with temperature. According to Ref. [54], all diatomic molecules show a monotonic drop in Z as λ increases. For some typical ranges of quantum number λ, Z achieves a constant value before declining further.

Nevertheless, Z monotonically increases with increasing β. A closed-form representation of the temperature-dependent partition function $Z(\beta)$ was developed. In Ref. [65], the authors plotted the vibrational partition function variation with a different of q values, it can be observed. that when β rises, the partition function gets smaller. Furthermore, when q rises, Z decreases as β increases. Furthermore, as q increases then Z does as well.
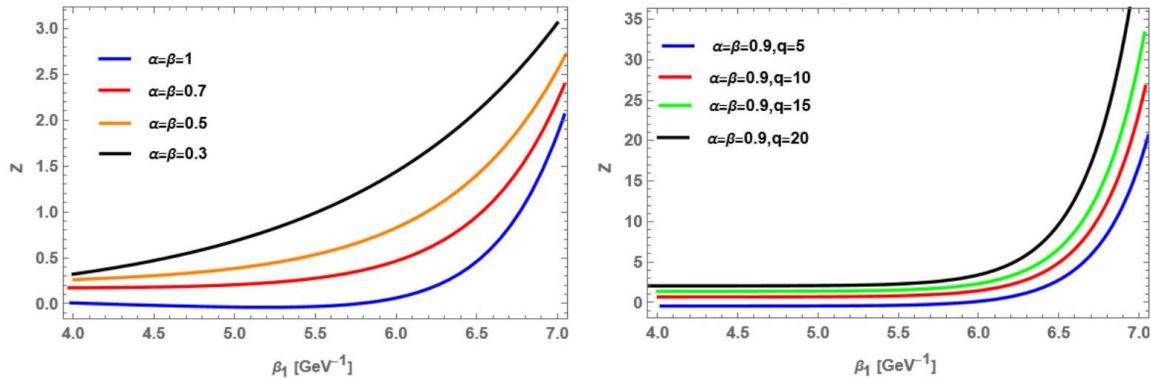

Figure 2. (The left panel), the partition function (Z) is displayed as a function of β_1, for various values of α, and β. (The right panel), the partition function (Z) is displayed as a function of β_1, for various values of deformed parameter q for CPSHEP at $\alpha = \beta = 0.9$

In Fig. 3 (the left panel), the behavior of curves for free energy $F(\beta_1)$ increases monotonically by decreasing temperature (β_1), by increasing α and β curves become higher using Eq. (95). This finding has a good agreement with Ref. [62]. In Fig. 3 (the right panel). For the superstatics, when the system's temperature (β_1) steadily drops, $F_s(\beta_1)$ rises monotonically. A decrease in the deformed parameter (q) always results in a larger free energy using Eq. (122). In Ref. [5], for CuLi and ScF, the free energy curves only decrease gradually with increasing β, but for various values of λ, the free energy curves of HCl and ScF increases and get lower with increasing β. In Ref. [63], when β rises, the free energy falls monotonically.
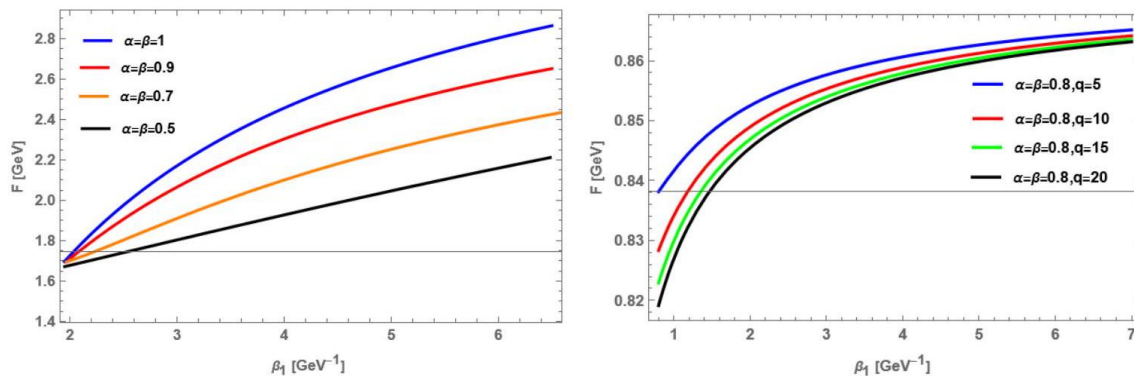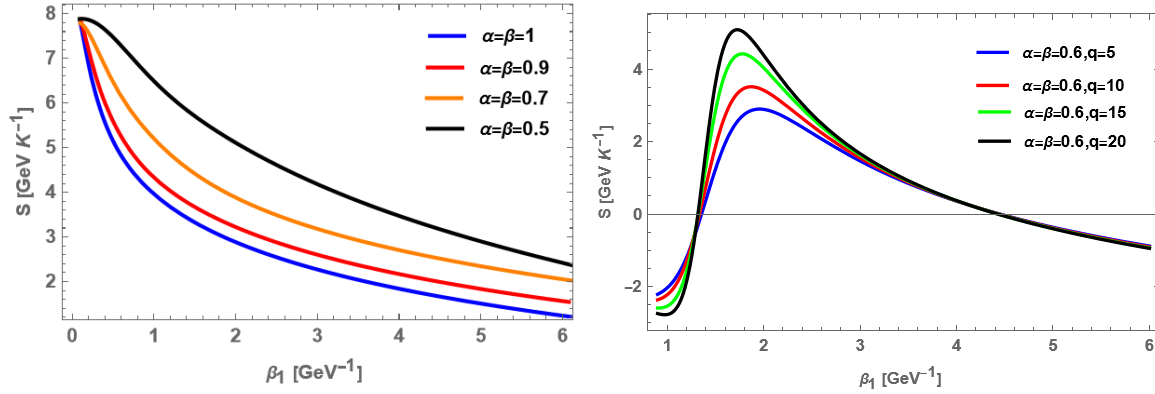

Figure 3. (The left panel), the free energy (F) is displayed for various values of α as a function of β_1, and β. (The right panel), F is displayed as a function of β_1, for various values of deformed parameter q for CPSHEP at $\alpha = \beta = 0.8$.

By increasing the deformation parameter q, the free energy curves rise and converge. As demonstrated in Fig. 4 (The left panel), and Fig. 4 (the right panel), we displayed the vibrational mean energy variation $U(\beta_1)$ versus superstatics and thermodynamic properties, respectively.
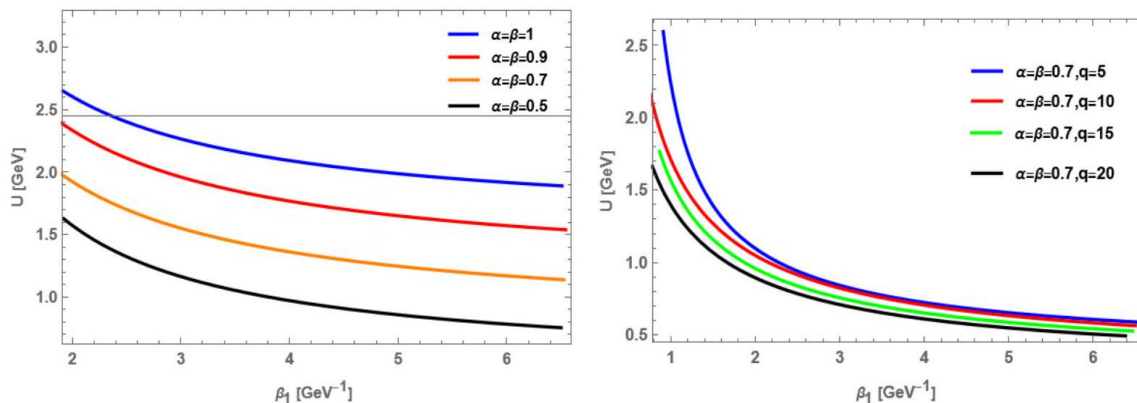

Figure 4. (The left panel), the mean energy (U) is displayed as a function of β_1 for various values of α, and β. (The right panel), the mean energy is displayed as a function of β_1, for various values of deformed parameter q for CPSHEP at $\alpha = \beta = 0.7$.

Fig. 4 (the left panel), illustrates how $F(\beta_1)$ rises with decreasing values for all values of β_1. Additionally, curves rise when the values of the fractional parameters β and α increase using Eq. (97). In Fig. 4 (the right panel), illustrates how the superstatics mean energy $U_s(\beta_1)$ changes when the system's temperature reduces. For different values of the deformed parameter (q), $U_s(\beta_1)$ decreases exponentially at a specific absolute temperature. According to Fig. 4 (the right panel), the variation of curves converges for the superstatics. Additionally, the superstatics in Fig. 4(the right panel), show that $U_s(\beta_1)$ decrease as β_1 grows and curves become lower when q increases by using Eq. (123). This behavior is computable with Ref. [55], with rising β and quantum number λ, $U_s(\beta_1)$ at first rises monotonically and subsequently reduces. Also, in Ref. [56], by increasing β_s then U decreases. When the values of α and β increase then the curves become lower as in Fig. 4 (the right panel), $U_s(\beta_1)$ decreases with increasing β and increases with increasing q as in Ref. [65]. In Fig. 5 (the left panel), we note that entropy $S(\beta_1)$ declines as the system's temperature rises (β_1 dropping), and $S(\beta_1)$ associated with vibrations is diverging.

Figure 5. (The left panel), the entropy (S) is displayed as a function of β_1 for various values of α, and β. (The right panel), S is displayed as a function of β_1, for various values of deformed parameter q for CPSHEP at $\alpha = \beta = 0.6$.

In Fig. 5 (the right panel), the curves become lower when fractional parameters α and increase by using Eq. (102). In Fig. 5(the left panel), the superstatistics entropy $S_s(\beta_1)$ changes directly with temperature and inversely with β_1. This means that for any value of the deformed parameter, the system's disorderliness grows as the system's temperature rises. $S_s(\beta_1)$ converged when q increases then behavior of curves becomes higher, $S_s(\beta_1)$ has a turning point when β_1 equals 2 as shown in Fig. 5 (the left panel) using Eq. (124). This behavior is compatible with Ref. [52] and Ref. [57], which entropy (S) varies in reverse with respect to a range of values β. For light quark, and natural particles, the authors of Ref. [58, 59, 60] showed that S increases with increasing temperature. In Ref. [65], the authors showed that as β increases then the system's entropy decreases, the system's entropy rises when the deformation parameter q grows for a variety of values.
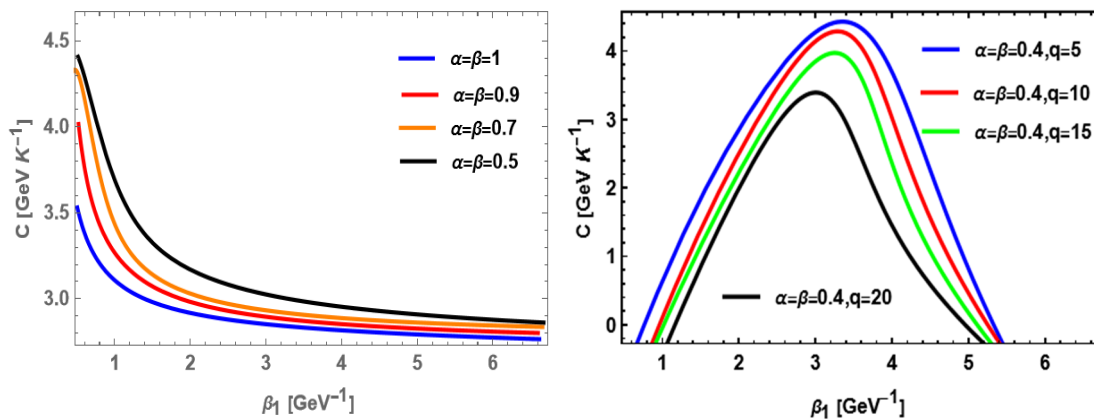
Figure 6. (The left panel), the specific heat (C) is displayed as a function of β_1 for various values of α, and β. (The right panel), C is displayed as a function of β_1, for various values of deformed parameter q for CPSHEP at $\alpha = \beta = 0.4$.

In Fig. 6 (the right panel), we plotted the specific heat by using Eq. (108), here is the heat capacity's behavior $C(\beta_1)$ against β_1 for various values of α and β. We note that $C(\beta_1)$ increases monotonically with decreasing β_1. Also, when α and β decrease the curves get higher. In Fig. 6 (the left panel), for superstatistics, variations in the heat capacity $C_s(\beta_1)$ against β_1 is plotted for various values of the deformation parameter q, it is noticeable that $C_s(\beta_1)$ increases with decreasing β_1. Also, $C_s(\beta_1)$ converges when q increases, then the behavior of curves becomes lower as depicted. $C_s(\beta_1)$ has a turning point when β_1 equals 3 GeV^{-1} using Eq. (125). This action has the same behavior for many works, such as in Ref. [61], for various values of λ, the author displayed specific capacity versus temperature (β), C increases as β

decreases. As in Ref. [65], It is clearly visible that when q grows, the system's specific heat capacity falls while increasing monotonically with (β). It's also significant to observe that normal statistics are returned when $q = 0$. In Ref. [55], the authors depict how specific heat $C(\beta)$ changes in relation to temperature. Specific heat grows monotonically as β rises. and then declines as β and λ rise, whenever every plot reaches convergence. Each plot's convergence provides a measure of the variability in temperatures at which charmonium disintegrates into its component parts as quark charms.

7. CONCLUSION

We eliminated the parametric second-order differential equation with generalized fractional derivative and we applied the NU method. Through the parametric generalized fractional Nikiforov-Uvarov (NU) approach, we arrive at the solution of the SE by employing Coulomb plus screened exponential hyperbolic potential. In addition, getting the special classical solution at $\alpha = \beta = 1$, then $k_1 = 1$ as in Ref. [47]. We estimated and plotted thermodynamic properties in the fractional form and discovered that our results are consistent with prior publications and that the physical behavior of thermodynamic properties. The work was expanded to include thermal characteristics and superstatics, such as partition function $Z(\beta_1)$, free energy $F(\beta_1)$, mean energy $U(\beta_1)$, entropy $S(\beta_1)$, and heat capacity $C(\beta_1)$. Our results revealed that the effect of the generalized fractional derivative on the thermodynamic properties and superstatics is the same. We conclude that fractional parameters play an important role using CPSEHP. Also, fractional parameter has a good effect on the behavior of thermodynamic and superstatistics curves. We also noticed that as free energy grows, internal energy, specific heat, and entropy decrease. Numerous studies, for example [57, 59, 65], do not explore the thermodynamic features and superstatics of heavy quarkonium in the fractional models. We conclude that the fractional parameter has a significant effect on thermodynamic properties.

ORCID

M. Abu-Shady, https://orcid.org/0000-0001-7077-7884

REFERENCES

[1] M. Dalir, and M. Bashour, Appl. Math. Sci. **4**, 1021 (2010).
[2] M. Abu-Shady, Int. J. Mod. Phys. A, **34**(31), 1950201 (2019). https://doi.org/10.1142/S0217751X19502014
[3] N. Jamshir, B. Lari, and H. Hassanabadi, Stat. Mech. Appl. Phys. A, **565**, 125616 (2021). https://doi.org/10.1016/j.physa.2020.125616
[4] M. Abu-Shady, and Sh.Y. Ezz-Alarab, Few-Body. Syst. **62**, 13 (2021). https://doi.org/10.1007/s00601-021-01591-7
[5] M. Abu-Shady, A.I. Ahmadov, H.M. Fath-Allah, and V.H. Badalov, J. Theor. Appl. Phys. 16, 3 (2022). https://doi.org/10.30495/jtap.162225
[6] A. Al-Jamel, Int. J. Mod. Phys. A, **34**, 1950054 (2019). https://doi.org/10.1142/S0217751X19500544
[7] M.M. Hammad, A.S. Yaqut, M.A. Abdel-Khalek, and S.B. Doma, Nuc. Phys. A, **1015**, 122307 (2021). https://doi.org/10.1016/j.nuclphysa.2021.122307
[8] G. Wang, and A.M. Wazwaz, Chaos. Solit. Fract. **155**, 111694 (2022). https://doi.org/10.1016/J.CHAOS.2021.111694
[9] M. Abu-Shady, and M.K.A. Kaabar, Math. Prob. Eng. **2021**, 9444803 (2021). https://doi.org/10.1155/2021/9444803
[10] M. Abu-Shady, and E. M. Khokha, Advances in High Energy Physics. **2018**, 7032041 (2018). https://doi.org/10.1155/2018/7032041
[11] M. Abu-Shady, and H. M. Fath-Allah, Int. J. Mod. Phys. A, **35**, 2050110 (2020). https://doi.org/10.1142/S0217751X20501109
[12] M. Abu-Shady, and A. N. Ikot, Eur, Phys. J. Plus. **135**, 321 (2019). https://doi.org/10.1140/epjp/i2019-12685-y
[13] M. Abu-Shady, E. M. Khokha, T. A. Abdel-Karim, European Physical Journal D, **76**(9), 159 (2022). https://doi.org/10.1140/epjd/s10053-022-00480-w
[14] H. Karayer, D. Demirhan, and F. Büyükkılıç, Comm. Theor. Phys. **66**, 12 (2016). https://doi.org/10.1088/0253-6102/66/1/012
[15] C. Tezcan, and R. Sever, Int. J. Theor. Phys. **48**, 337 (2009). https://doi.org/10.1007/s10773-008-9806-y
[16] A. Berkdemir, C. Berkdemir, and R. Sever, Modern Phys. Lett. A, **21**, 2087 (2006). https://doi.org/10.1142/S0217732306019906
[17] M. C. Zhang, G.H. Sun, SH. Dong, Phys. Lett A, **374**, 704 (2010). https://doi.org/10.1016/j.physleta.2009.11.072
[18] G. Chen, Zeitschrift für Naturforschung A, **59**, 875 (2004). https://doi.org/10.1515/zna-2004-1124
[19] S. M. Al-Jaber, Int. J. Theor. Phys. **47**, 1853 (2008). https://doi.org/10.1007/s10773-007-9630-9
[20] K. J. Oyewumi, F. O. Akinpelu, and A.D. Agboo, Int. J. Theor. Phys. A, **47**, 1039 (2008). https://doi.org/10.1007/s10773-007-9532-x
[21] S. Ikhdair, and R. Sever, J. Mole. Struc. **855**, 13 (2008). https://doi.org/10.1016/j.theochem.2007.12.044
[22] H. Hassanabadi, S. Zarrinkamar, and A.A. Rajabi, Comm. Theor. Phys. **55**, 541 (2011). https://doi.org/10.1088/0253-6102/55/4/01
[23] S. Ikhdair, and R. Sever, Int. J. Modern Phys. C, **19**, 221 (2008). https://doi.org/10.1142/S0129183108012030
[24] R. Kumar, and F. Chand, Commun. Theor. Phys. **59**, 528 (2013). https://doi.org/10.1088/0253-6102/59/5/02
[25] S.M. Kuchin, and N.V. Maksimenko, Univ. J. Phys. Appl. **7**, 295 (2013). https://doi.org/10.13189/ujpa.2013.010310
[26] M. Abu-Shady, H. Mansour, and A.I. Ahmadov, Advances in High Energy Physics, **2019**, 4785615 (2019). https://doi.org/10.1155/2019/4785615
[27] M. Abu-Shady and E. M. Khokha, International Journal of Modern Physics A, **36**(29), 2150195 (2021). https://doi.org/10.1142/S0217751X21501955
[28] M. Abu-Shady, T. A. Abdel-Karim, and E. M. Khokha, Advances in High Energy Physics, **2018**, 356843 (2018). https://doi.org/10.1155/2018/7356843
[29] A.N. Ikot, O.A. Awoga, and A.D. Antia, Chinese Phys. B, **22**, 2 (2013). https://doi.org/10.1088/1674-1056/22/2/020304
[30] D. Agboola, Phys. Scripta. **80**, 065304 (2009). https://doi.org/10.1088/0031-8949/80/06/065304

[31] H. Hassanabadi, B.H. Yazarloo, S. Zarrinkamar, and M. Solaimani, Int. J. Quant. Chem. **112**, 3706 (2012). https://doi.org/10.1002/qua.24064

[32] H. Hassanabadi, E. Maghsoodi, A. N. Ikot, and S. Zarrinkamar, Appl. Math. Comput. **219**, 9388 (2013). https://doi.org/10.1016/j.amc.2013.03.011

[33] Wahyulianti, A. Suparmi, C. Cari, and F. Anwar, J. Phys. Conf. Serie. **795**, 012022 (2017). https://doi.org/10.1088/1742-6596/795/1/012022

[34] S. Flugge, *Practical Quantum Mechanics*, (Springer-Verlag, 1974).

[35] C. A. Onate, I. B. Okon, U.E. Vincent, E.S. Eyube, M.C. Onyeaju, E. Omugbe, and G.O. Egharevba, Sci. Rep. **12**, 15188 (2022). https://doi.org/10.1038/s41598-022-19179-4

[36] C.O. Edet, U.S. Okorie, G. Osobonge, A.N. Ikot, G.J. Rampho, and R. Sever, J. Math. Chem. **58**, 989 (2020). https://doi.org/10.1007/s10910-020-01107-4

[37] A.N. Ikot, E.O. Chukwuocha, M.C. Onyeaju, C.A. Onnle, B.I. Ita, and M.E. Udoh, Pramana – J. Phys. **90**, 22 (2018). https://doi.org/10.1007/s12043-017-1510-0

[38] C.A. Onate, Chinese J. Phys. **54**, 165 (2016). https://doi.org/10.1016/j.cjph.2016.04.001

[39] I.B. Okon, O.O. Popoola, E. Omugbe, A.D. Antia, C.N. Isonguyo, and E.E. Ituen, Comput. Theor. Chem. **1196**, 11132 (2021). https://doi.org/10.1016/j.comptc.2020.113132

[40] K.J. Oyewumi, B.J. Falaye, C.A. Onate, O.J. Oluwadare, and W.A. Yahya, Molec. Phys. **112**, 127 (2014). https://doi.org/10.1080/00268976.2013.804960

[41] A. Boumali, and H. Hassanabadi, Eur. Phys. J. Plus. **128**, 124 (2013). https://doi.org/10.1140/epjp/i2013-13124-y

[42] M. Abu-Shady, and H.M. Fath-Allah, East. Eur. J. Phys. (3), 248 (2023). https://doi.org/10.26565/2312-4334-2023-3-22

[43] M. Rashdan, M. Abu-Shady, and T.S.T. Ali, Int. J. Mod. Phys. E, **15**(1), 143 (2006). https://doi.org/10.1142/S0218301306003965

[44] M. Abu-Shady, Int. J. Mod. Phys. E, **21**, 1250061 (2012). https://doi.org/10.1142/S0218301312500619

[45] M.M. Hammad, *et al.*, Nucl. Phys. A, **1015**, 122307 (2021). https://doi.org/10.1016/j.nuclphysa.2021.122307

[46] A.F. Nikiforov, and V.B. Uvarov, *Special Functions of Mathematical Physics*, (Birkhuser, Basel), (1988).

[47] I. Okon, C. Onate, E. Omugbe, U. Okorie, *et. al.*, Advances in High Energy Physics, **2022**, 5178247 (2022). https://doi.org/10.1155/2022/5178247

[48] C. Beck, "Superstatistics: theory and applications," Continuum. Mech. Thermodyn. **16**, 293 (2004). https://doi.org/10.1007/s00161-003-0145-1

[49] C. Beck, and E.G. Cohen, arXiv:cond-mat/0205097v2 14 Nov 2002.

[50] C.O. Edet, P.O. Amadi, U.S. Okorie, A. Tas, A.N. Ikot, and G. Rampho, Revista Mexicana de Fisica. **66**, 824 (2020). https://doi.org/10.31349/RevMexFis.66.824

[51] I. Okon, C. Onate, E. Omugbe, *et. al.*, Advances in High Energy Physics, **2022**, 178247, (2022). https://doi.org/10.1155/2022/5178247

[52] E.P. Inyang, F. Ayedun, E.A. Ibanga, M.K. Lawal, *et. al.*, Result. Phys. **43**, 106075 (2022). https://doi.org/10.1016/j.rinp.2022.106075

[53] B.I. Okon, O. Popoola, E. Omugbe, D.A. Antia, *et. al.*, Comput. Theor. Chem. **1196**, 113112 (2021).

[54] P.E. Inyang, P.E. Inyang, I.O. Akpan, J.E. Ntibi, and E.S. William, Canad. J. Phys. **99**, 982 (2021). https://doi.org/10.1139/cjp-2020-0578

[55] M. Abu-Shady, and Sh.Y. Ezz-Alarab, India. J. Phys. **97**, 3661 (2023). https://doi.org/10.1007/s12648-023-02695-y

[56] V. Kumar, S.B. Bhardwa, R.M. Singh, and F. Chand, Pramana. J. Phys. **96**, 125 (2022). https://doi.org/10.1007/s12043-022-02377-0

[57] H. Hassanabadi, M. Hosseinpoura, Eur. Phys. J. C, **76**, 553 (2016). https://doi.org/10.1140/epjc/s10052-016-4392-2

[58] H.G. Mansour, and A. Gamal, Advances in High Energy Physics, **7**, 7269657 (2018). https://doi.org/10.1155/2018/7269657

[59] P.E. Inyang, O.E. Obisung, S.E. William, and B.I. Okon, East. Eur. J. Phys. (3), 104 (2022). https://doi.org/10.26565/2312-4334-2022-3-14

[60] K.J. Oyewum, B.J. Falaye, C.A. Onate, O.J. Oluwadare, and W.A. Yahya, Molec. Phys. **112**, 127 (2014). https://doi.org/10.1080/00268976.2013.804960

[61] D. Ebert, R. N. Faustov, V.O. Galkin, Phys. Rev. D, **67**, 014027, (2003). https://doi.org/10.1103/PhysRevD.67.014027

[62] M. Abu-shady, and H.M. Fath-Allah, Advances in High Energy Physics, **2022**, 4539308 (2022). https://doi.org/10.1155/2022/4539308

[63] H. Hassanabadi, and M. Hosseinpour, Eur. Phys. J. C, **76**, 553 (2016). https://doi.org/10.1140/epjc/s10052-016-4392-2

[64] A.N. Ikot, U.S. Okorie, G. Osobonye, P.O. Amadi, C.O. Edet, *et al.*, Heliyon. **6**, e03738 (2020). https://doi.org/10.1016/j.heliyon.2020.e03738

[65] H. Hassanabadi, M. Hosseinpoura, Eur. Phys. J. C, **76**, 553 (2016). https://doi.org/10.1140/epjc/s10052-016-4392-2

ВПЛИВ ДРОБОВИХ ПОХІДНИХ НА ТЕРМОДИНАМІЧНІ ВЛАСТИВОСТІ ШЛЯХОМ ВИВЧЕННЯ ВЗАЄМОДІЇ CPSEHP

М. Абу-Шаді, Ш. Ю. Езз-Алараб

Факультет природничих наук, кафедра математики та інформатики, Університет Менуфія, Шебін Елком 32511, Єгипет

Параметричний метод Нікіфорова-Уварова (N-U) використовується в поєднанні з узагальненою дробовою похідною (GFD) для дослідження власних значень енергії та загальної нормалізованої хвильової функції, пов'язаної з кулоновським плюс екранованим експоненціальним гіперболічним потенціалом (CPSEHP) у термінах поліномів Якобі. Цей потенціал виявляє максимальну ефективність при менших значеннях параметра екранування. Щоб дослідити термічні та суперстатистичні характеристики, отримані власні значення енергії безпосередньо включаються до сумісної суми (Z) і згодом використовуються для визначення інших термодинамічних величин, включаючи середню енергію коливань (U), питому теплоємність (C), ентропію (S) і вільну енергію (F). Проведено порівняння з попередніми дослідженнями. Класичний випадок відновлюється з дробового випадку встановленням α = β = 1 відповідно до попередньої роботи. Наші результати демонструють, що фракційний параметр відіграє вирішальну роль у керуванні тепловими та суперстатистичними властивостями в рамках цієї моделі.

Ключові слова: *рівняння Шредінгера; параметричний метод Нікіфорова-Уварова; термодинамічні властивості; Суперстатика; узагальнена дробова похідна*

CONFORMABLE SCHRÖDINGER EQUATION WITH PSEUDOHARMONIC POTENTIAL AND ITS THERMODYNAMIC PROPERTIES

Derar Altarawneh[a], **Eqab M. Rabei**[b]

ᵃDepartment of Applied Physics, Tafila Technical University, Tafila, 66110, Jordan
ᵇPhysics Department, Faculty of Science, Al al-Bayt University, P.O. Box 130040, Mafraq 25113, Jordan
*Corresponding Author e-mail: derar@ttu.edu.jo

In this work, the Nikiforov-Uvarov (NU) method is used to obtain the exact solution of the conformable radial Schrödinger equation (SE) for the pseudoharmonic potential. We derive both the energy states and the corresponding wave functions, and the results are compared with those in the existing literature for the case of the traditional derivative ($\alpha = 1$). Additionally, the obtained energy states are used to calculate the conformable partition function in the classical limit. Thermodynamic properties, including the conformable Helmholtz free energy, conformable mean energy, conformable entropy, and conformable specific heat capacity, are calculated and analyzed for N_2 and CO molecules.

Keywords: *Nikiforov-Uvarov method; Pseudoharmonic potential; Thermodynamic properties; Conformable partition function*

PACS: 45.10.Hj, 03.65.Ge

1. INTRODUCTION

The exact solution of the Schrödinger wave equation for various potentials has been an attractive area of research for scientists in theoretical physics and related fields over the past several decades [1, 2, 3, 4, 5]. These solutions are important in both relativistic and non-relativistic regimes due to their significant role in statistical physics, solid-state physics, quantum field theory, and molecular physics. Such solutions provide complete information about quantum systems, including thermodynamic properties, mass spectra, and optical characteristics [6, 7, 8]. Several methods for solving Schrödinger wave equations have been reported to date, among which are the Nikiforov-Uvarov method [9, 10, 11], the factorization method [12, 13, 14], the series expansion method [15], and the functional analysis approach [16]. Among them, the NU method, originally developed to solve second-order differential equations of the hypergeometric type, has been widely applied to time-independent quantum problems [17].

Many scientists, including Riemann-Liouville, Caputo, and Riesz, have made significant contributions to the development of definitions for non-integer derivatives and their applications in physics [19, 20, 21, 22].These definitions take various forms, but most of them include operators of fractional derivatives that act as non-local operators. Thus, many of the basic properties of integer derivatives, such as the product and chain rules, do not hold for fractional derivatives. This makes algebraic operations in non-integer calculus challenging, as these foundational principles cannot be directly applied. To address these challenges, a new definition, known as the conformable fractional derivative, has been introduced [18].This definition provides many classical properties of derivatives and is thus more applicable in practical applications; the formal definition of such a derivative is given below in Equation 1.

$$D^\alpha[f(x)] = \lim_{\varepsilon \to 0} \frac{(f(x + \varepsilon x^{1-\alpha}) - f(x))}{\varepsilon}, x > 0 \tag{1}$$

where $0 < \alpha \le 1$, this definition reduces to the classical definition of the first derivative when $\alpha = 1$. More properties of the conformable fractional derivative can be found in [18]. A significant number of studies have been conducted in recent years to extend the definition and express mathematical tools using conformable derivative notation, making it ready for use in applied sciences [23, 24, 25, 26]. In quantum physics, the conformable fractional NU method has been developed and applied to investigate solutions of the conformable SE for various potentials [27, 35]. Conformable mechanics could introduce new ways to engineer and interact with quantum systems, enhancing control, flexibility, and precision while potentially enabling new quantum phenomena and applications across quantum computing, sensing, and communication.

Many studies have explored the implications of the conformable derivative on classical and quantum mechanics. Reference [38] examines some applications of the conformable derivative in physics, including a detailed discussion of the divergence and Green's theorem. Additionally, the basics of Newtonian mechanics in the context of conformable derivatives are covered. While the conformable equation for hydrogen-like systems is discussed by Al-Masaeed et al [36], the analytical solutions are obtained for the angular part in terms of conformable Laguerre functions. Furthermore, the

deformation of special relativity within the framework of conformable derivatives is formulated by Al-Jamel et al [39]. In this work, we will deal with the pseudoharmonic oscillator, which has the form [32]:

$$V(r) = D_e(\frac{r}{r_0} - \frac{r_0}{r})^2 \tag{2}$$

Where, D represents the dissociation energy between two atoms, and r_0 the equilibrium intermolecular separation. The pseudoharmonic oscillator is one of the most important molecular potentials in chemical physics, molecular physics, and related areas, due to its numerous applications in studying diatomic molecules. In fact, the significance of using pseudoharmonic potentials lies in their ability to more accurately describe real physical systems, especially in cases where the simple harmonic approximation breaks down. By incorporating anharmonic corrections, pseudoharmonic potentials provide a better fit for vibrational, thermodynamic, and molecular dynamics calculations, making them an essential tool in the study of complex systems in physics and chemistry. The pseudoharmonic potential is a useful tool for modeling anharmonicity in molecular and atomic systems, but it has limitations in its ability to capture strong anharmonicity, large displacements, or complex multi-body interactions. In cases where these limitations are important, more sophisticated potentials may be needed. The essential advantage of the SE with this potential consists in the fact that it allows one to get the exact solution for every rotational quantum number l [28, 29, 30, 37]. This is in contrast to the other molecular potentials, e.g., Morse potential that can be solved exactly for non-rotating diatomic molecules [31].

This work aims to solve the conformable SE for the pseudoharmonic potential using the Nikiforov-Uvarov method. The goal is to obtain the relevant energy spectrum and wave functions for a general conformable derivative of order α and to compare the findings with the existing literature for the specific case where $\alpha = 1$. Additionally, the present study also aims to derive the expression for the conformable partition function in the classical limit and calculate associated thermodynamic properties, such as the conformable vibrational mean energy, conformable specific heat, conformable free energy, and conformable entropy. Solving the conformable SE expands the applicability of quantum mechanical principles to more general and complex systems, supporting current research that aims to better understand and predict behaviors in diverse areas of physics and quantum computing.

2. CONFORMABLE SCHRÖDINGER EQUATION WITH PSEUDOHARMONIC POTENTIAL

The SE in three dimensions, when expressed in spherical coordinates (r, θ, ϕ) takes the form of a partial differential equation. In spherical coordinates, the time-independent SE for a particle with a potential $V(r, \theta, \phi)$ is given by:

$$\frac{-\hbar^2}{2m}\nabla^2\psi(r, \theta, \phi) + V(r, \theta, \phi)\psi(r, \theta, \phi) = E\psi(r, \theta, \phi) \tag{3}$$

To solve this equation, it is common to assume that the wavefunction can be separated into radial and angular components. In this work, we will focus on the conformable radial SE, as it varies for each system. However, the angular part has been solved in previous studies, as outlined in [36]. The radial SE is given by:

$$\frac{d^2R(r)}{dr^2} + \frac{2}{r}\frac{dR(r)}{dr} + \frac{2\mu}{\hbar^2}(E_{nl} - V(r) - \frac{l(l+1)\hbar^2}{2\mu r^2})R(r) = 0 \tag{4}$$

Where μ is the reduced mass, n and l denote the quantum numbers. Using relation (2) and the change of variable $(r = s^{\frac{1}{2}})$, the SE for the Pseudoharmonic potential takes the form [33]:

$$\frac{d^2R}{ds^2} + \frac{3/2}{s}\frac{dR}{ds} + \frac{1}{s^2}[-\gamma^2 s^2 - \epsilon s - \beta]R(s) \tag{5}$$

where

$$\gamma = \sqrt{\frac{D_e}{r_0}\frac{\mu}{2\hbar^2}} \qquad\qquad \epsilon = [E_{nl} + 2D_e]\frac{\mu}{2\hbar^2} \qquad\qquad \beta = (D_e r_0^2 + \frac{l(l+1)\hbar^2}{2\mu})\frac{\mu}{2\hbar^2} \tag{6}$$

Now, we would like to express the SE for Pseudoharmonic potential in terms of conformable derivative as follows:

$$D^\alpha D^\alpha R(s) + \frac{3/2}{s}D^\alpha R(s) + \frac{1}{s^2}[-\gamma^2 s^2 - \epsilon s - \beta]R(s) \tag{7}$$

Using the properties of conformable fractional derivative [18]

$$D^\alpha R(s) = s^{(1-\alpha)}R(s)$$

$$D^\alpha D^\alpha R(s) = (1-\alpha)s^{(1-2\alpha)}\frac{dR}{ds} + s^{(2-2\alpha)}\frac{d^2R}{ds^2}$$

The conformable SE for pseudoharmonic potential can be written as:

$$R''(s) + \frac{\frac{5}{2} - \alpha}{s} R'(s) + \frac{1}{s^2}[-\gamma^2 s^{2\alpha} - \epsilon s^\alpha - \beta]R(s) \tag{8}$$

Next, we compare the Conformable equation (8) with the basic equation of traditional NU method

$$\psi''(s) + \frac{\tilde{\tau}_f(s)}{\sigma_f(s)}\psi'(s) + \frac{\tilde{\sigma}}{\sigma_f^2}\psi(s) \tag{9}$$

The parameters in Eq (9) can be determined as:

$$\tilde{\tau}_f(s) = \frac{5}{2} - \alpha \qquad\qquad \tilde{\sigma}_f(s) = [-\gamma^2 s^{2\alpha} + \epsilon s^\alpha - \beta] \qquad\qquad \sigma_f(s) = s \tag{10}$$

The function $\pi_f(s)$ and parameter λ which are given by NU read as:

$$\pi_f(s) = \frac{D^\alpha(\sigma_f(s)) - \tilde{\tau}_f(s)}{2} \pm \sqrt{(\frac{D^\alpha(\sigma_f(s)) - -\tilde{\tau}_f(s)}{2})^2 - \tilde{\sigma}_f(s) + k\sigma_f(s)} \qquad \lambda(s) = K(s) + D^\alpha \pi_f(s) \tag{11}$$

Which can be calculated for our problem as:

$$\pi_f(s) = \frac{-3s^{\alpha-1}}{4} + \frac{\alpha}{2} \pm \sqrt{[\frac{-3s^{\alpha-1}}{4} + \frac{\alpha}{2}]^2 - [-\gamma^2 s^{2\alpha} + \epsilon s^\alpha - \beta] + ks^\alpha} \tag{12}$$

To solve the quadratic equation inside the square root in Eq (12), the discriminant must be set to zero. This condition leads to a new quadratic equation, which can then be solved to determine the constant $K(s)$, ensuring the existence of both roots.

$$K_1 = \epsilon + 2\gamma\sqrt{\frac{\alpha^2}{4} - \frac{12\alpha}{16} + \beta + \frac{9}{16}} \qquad\qquad K_2 = \epsilon - 2\gamma\sqrt{\frac{\alpha^2}{4} - \frac{12\alpha}{16} + \beta + \frac{9}{16}} \tag{13}$$

Substituting the two values of K from Eq (13) into Eq (12) yields four possible forms of $\pi_f(s)$:

$$\pi_f(s) = \frac{-3s^{\alpha-1}}{4} + \frac{\alpha}{2} \pm (\gamma s^\alpha + \sqrt{\frac{\alpha^2}{4} - \frac{12\alpha}{16} + \beta + \frac{9}{16}}) \qquad \text{(for } K_1) \tag{14}$$

$$\pi_f(s) = \frac{-3s^{\alpha-1}}{4} + \frac{\alpha}{2} \pm (\gamma s^\alpha - \sqrt{\frac{\alpha^2}{4} - \frac{12\alpha}{16} + \beta + \frac{9}{16}}) \qquad \text{(for } K_2) \tag{15}$$

To ensure the derivative of the polynomial $\tau_f(s)$ is negative, the appropriate form of the polynomial $\pi_f(s)$ must be selected. Therefore, the most suitable expression for $\pi_f(s)$ is:

$$\pi_f(s) = \frac{-3s^{\alpha-1}}{4} + \frac{\alpha}{2} - (\gamma s^\alpha - \sqrt{\frac{\alpha^2}{4} - \frac{12\alpha}{16} + \beta + \frac{9}{16}}) \tag{16}$$

The function $\tau_f(s)$ is defined as:

$$\tau_f(s) = \tilde{\tau}_f(s) + 2\pi_f(s) = \frac{5}{2} - \alpha + 2\pi_f(s) \tag{17}$$

Substituting the value of $\pi_f(s)$ into $\tau_f(s)$ we can write:

$$\tau_f(s) = 1 - 2\left(\gamma s^\alpha - \sqrt{(\frac{\alpha^2}{4} - \frac{12\alpha}{16} + 16\beta + 9)}\right) \tag{18}$$

Based on the values of $K(s)$ and $\pi_f(s)$, the value of $\lambda(s)$ is obtained as:

$$\lambda(s) = K(s) + D^\alpha \pi_f(s) = [\epsilon - 2\gamma\sqrt{\frac{\alpha^2}{4} - \frac{12\alpha}{16} + \beta + \frac{9}{16}} - \gamma\alpha]s^{\alpha-1} \tag{19}$$

Also

$$\lambda_n(s) = -nD^\alpha \tau(s) - \frac{n(n-1)}{2}D^\alpha D^\alpha \sigma_f(s) = n(2\gamma\alpha s^{\alpha-1}) \tag{20}$$

Using the fact that $(\lambda_n(s) = \lambda(s))$, one obtains:

$$n(2\gamma\alpha s^{\alpha-1}) = \epsilon - 2\gamma\sqrt{\frac{\alpha^2}{4} - \frac{12\alpha}{16} + \beta + \frac{9}{16}} - \gamma\alpha \tag{21}$$

Thus, utilizing the value of γ, β and ϵ, the conformable energy state can be expressed as:

$$E_{nl} = [-2D_e + \sqrt{\frac{D_e}{r_0^2}\frac{\mu}{2\hbar^2}}\frac{2\hbar^2}{\mu}[2\alpha n + \alpha + 2\sqrt{\frac{\alpha^2}{4} - \frac{12\alpha}{16} + D_e r_0^2 + \frac{l(l+1)\hbar^2}{2\mu})\frac{\mu}{2\hbar^2} + \frac{9}{16}}]] \tag{22}$$

For the case of $\alpha = 1$, this result shows good agreement with the literature [33], as clearly demonstrated in the Table **??**, which includes numerical results for the energy states with different values of α. The potential parameters are taken from Ref. [34].

Table 1. Energy states (in eV) of pseudoharmonic potential for N_2, CO molecules with different values of n and l at different values of α.

		N_2				CO			
n	l	$\alpha = 0.2$	$\alpha = 0.5$	$\alpha = 0.8$	$\alpha = 1.0$	$\alpha = 0.2$	$\alpha = 0.5$	$\alpha = 0.8$	$\alpha = 1.0$
0	0	0.02228044	0.05489432	0.08755324	0.10935087	0.036735676	0.086041306	0.135670387	0.168936188
1	0	0.06595773	0.16418266	0.26241458	0.32792754	0.104130339	0.254527961	0.405249027	0.505909491
1	1	0.06649613	0.16468298	0.26291495	0.32842786	0.107724515	0.258122693	0.408844177	0.509504835
2	0	0.10971111	0.27347099	0.43727592	0.54650428	0.171525002	0.423014616	0.674827674	0.842882795
2	1	0.11021143	0.27397132	0.43777624	0.54700453	0.175119173	0.426609348	0.678422839	0.846478145
2	2	0.11121203	0.27497192	0.43877686	0.54800515	0.182302607	0.433793912	0.685608218	0.853663932
3	0	0.15342644	0.38275933	0.61213726	0.76508088	0.238919659	0.591501265	0.944406314	1.179856105
3	1	0.15392676	0.38325966	0.61263757	0.76558121	0.242513836	0.595096003	0.948001471	1.183451449
3	2	0.15492736	0.38426026	0.61363824	0.76658182	0.249697274	0.602280561	0.955186871	1.190637242
3	3	0.15642817	0.38576109	0.61513903	0.76808266	0.260460206	0.613045182	0.965952735	1.201403693
4	0	0.19714177	0.49204767	0.78699859	0.98365755	0.306314323	0.759987929	1.213984967	1.516829415
4	1	0.19764209	0.49254799	0.78749891	0.98415787	0.309908493	0.763582652	1.217580117	1.520424759
4	2	0.19864269	0.49354859	0.78849953	0.98515851	0.317091933	0.770767216	1.224765512	1.527610552
4	3	0.20014353	0.49504943	0.79000037	0.98665933	0.327854869	0.781531837	1.235531375	1.538377003
4	4	0.20214446	0.49705039	0.79200133	0.98866031	0.342182739	0.795861935	1.249863133	1.552709535
5	0	0.24135743	0.60183633	0.96236024	1.20273454	0.373708986	0.928474575	1.483563608	1.853802719
5	1	0.24235803	0.60283692	0.96336087	1.20373516	0.377303156	0.932069307	1.487158758	1.857398069
5	2	0.24385885	0.60433776	0.96486179	1.20523678	0.384486597	0.939253871	1.494344158	1.864583856
5	3	0.24585984	0.60633872	0.96686267	1.20723697	0.395249526	0.950018492	1.505110028	1.875350307
5	4	0.24836073	0.60883967	0.96936647	1.20973795	0.409577396	0.964348593	1.519441784	1.889682839
5	5	0.24836073	0.60883967	0.96936364	1.20973795	0.427450912	0.982224896	1.537320127	1.907562153

The energy states were derived from the special case of the SE for the pseudoharmonic potential strongly depend on the fractional parameter α. When α is assumed to be equal to unity, the results agree with classical quantum mechanical results, which validate the approach used in this study. However, as α decreases, energy levels start to differ significantly, indicating the fractional-order dynamics influence the quantum behavior of the system. Physically, such a transition can be interpreted as a restriction to vibrational motion and hence a decrease in the density of available states. Now, let us determine the corresponding wavefunction for the conformable radial equation. The polynomial solution of the hypergeometric-type function (Rodrigues' formula) $y_{nf}(s)$ depends on the determination of the weight function $\rho_f(s)$, as follows:

$$D^\alpha[\sigma_f(s)\rho_f(s)] = \tau_f(s)\rho_f(s) \qquad\qquad y_{nf} = \frac{B_n}{\rho(s)}\frac{d^n}{ds^n}[\sigma_f^n(s)\rho(s)] \tag{23}$$

And

$$\frac{D^\alpha \phi_f(s)}{\phi_f(s)} = \frac{\pi_f(s)}{\sigma_f(s)} \qquad \text{where} \qquad \psi_f(s) = \phi_f(s)y_f(s) \tag{24}$$

By utilizing Eq 24, we obtain:

$$\phi_f(s) = s^{\frac{1}{4}[2\alpha - 3 + 4\sqrt{\frac{\alpha^2}{4} - \frac{12\alpha}{16} + \beta + \frac{9}{16}}]}e^{\frac{-\gamma s^\alpha}{\alpha}} \tag{25}$$

and

$$\rho_f(s) = e^{\frac{-2\gamma s^\alpha}{\alpha}}[s^{\frac{1}{2}(4\alpha^2 - 12\alpha + 16\beta + 9)}] \tag{26}$$

Substituting $\rho_f(s)$ into Eq 23 allows us to obtain the polynomial $y_{nf}(s)$ as follows:

$$y_{nf} = B_n s^{-\sqrt{\alpha^2 - 3\alpha + 64\beta + 36}}e^{\frac{2\gamma s^\alpha}{\alpha}}\frac{d^n}{ds^n}(s^{n - \sqrt{\alpha^2 - 3\alpha + 64\beta + 36}}e^{\frac{-2\gamma s^\alpha}{\alpha}}) \tag{27}$$

Using $\psi_f(s) = \phi_f(s)y_{nf}$, the conformable wavefunction can be written as:

$$\psi_f(s) = N_n s^{\frac{1}{4}[2\alpha - 3 + 4\sqrt{\frac{\alpha^2}{4} - \frac{12\alpha}{16} + \beta + \frac{9}{16}}]}e^{\frac{-\gamma s^\alpha}{\alpha}}.s^{-\sqrt{\alpha^2 - 3\alpha + 64\beta + 36}}e^{\frac{2\gamma s^\alpha}{\alpha}}\frac{d^n}{ds^n}(s^{n - \sqrt{\alpha^2 - 3\alpha + 64\beta + 36}}e^{\frac{-2\gamma s^\alpha}{\alpha}}) \tag{28}$$

For the case of $\alpha = 1$, this result shows exact agreement with the literature [33].

3. CONFORMABLE THERMODYNAMIC PROPERTIES FOR PSEUDOHARMONIC POTENTIAL

To obtain the conformable thermodynamic properties of the Pseudoharmonic Potential, it is important to calculate the vibrational partition function:

$$Z_{vib}(\beta) = \sum_{n=0}^{\lambda} e^{-\beta E_{nl}} \qquad \text{where} \qquad \beta = \frac{1}{K_b T} \tag{29}$$

λ, is the upper-bound vibrational quantum number. At high temperature T (classical limit) the sum can be converted to an integral, and the conformable partition function can be written as:

$$Z_{vib}(\beta) = \int_0^{\lambda} e^{\beta E_{nl}} n^{\alpha-1} dn \tag{30}$$

Using the conformable partition function of equation (30), the other thermodynamic properties such as conformable internal energy U, conformable free energy F, conformable entropy S, and the conformable specific heat capacity C_v can be calculated using the following definitions:

1. **Conformable Internal Energy -** $U(\beta) = -\beta^{1-\alpha} \frac{\partial}{\partial \beta}(\ln Z_{vib}(\beta))$
2. **Conformable Free Energy -** $F(\beta) = -\frac{1}{\beta} \ln Z_{vib}(\beta))$
3. **Conformable Entropy -** $S(\beta) = K_b \ln Z_{vib}(\beta) - K_b \beta \beta^{(1-\alpha)} \frac{\partial}{\partial \beta}(\ln Z_{vib}(\beta))$
4. **Conformable Specific Heat -** $C_v(\beta) = -K_b \beta^2 \beta^{(1-\alpha)} \frac{\partial U(\beta)}{\partial \beta}$

For the case of $\alpha = 1$, these definitions are consistent with the well-known thermodynamic definitions in literature.

4. RESULTS AND DISCUSSION
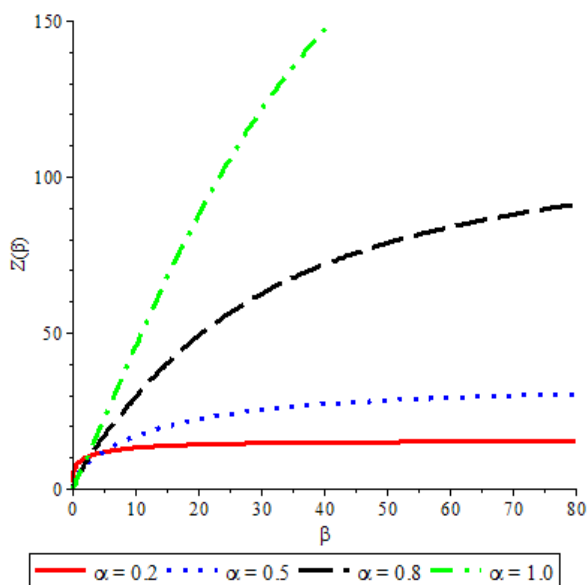
Figure 1. The Conformable Partition function as a function of β for N_2 molecule for different values of α
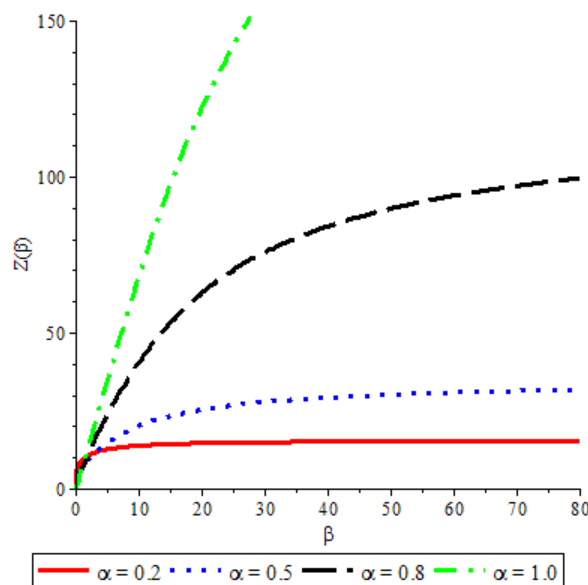

Figure 2. The Conformable Partition function as a function of β for CO molecule for different values of α

The results in Fig. 1 and Fig. 2 represent the behavior of the classical partition function $Z(\beta)$ of the diatomic molecules N_2 and CO, respectively, versus the inverse temperature parameter β, for several values of the fractional parameter α. The calculations of $Z(\beta)$ were performed for four different values of α, namely 0.2, 0.5, 0.8, and 1.0, corresponding to different curves. The fractional parameter α strongly affects the partition function. For $\alpha = 1.0$, which corresponds to the classical case, $Z(\beta)$ shows the largest values for all ranges of β. This is the conventional quantum mechanical behavior of the pseudoharmonic potential. When α is varied from 1.0 down to 0.2, the partition functions are strongly suppressed. This suppression is due to the effects of the conformable fractional derivative which changes the energy spectrum and provides a lower density of available states at higher energies. For both diatomic molecules, lower α values result in lower partition functions because certain higher energy states are not thermally accessible. This is important because it shows how conformable derivatives affect the modeling of systems with constrained vibrational dynamics Fig. 1 and Fig. 2 exhibit a similar qualitative dependence of $Z(\beta)$ on α. However, $Z(\beta)$ for CO is always higher compared to N_2, which reflects the different molecular parameters for these diatomic species such as bond strength,
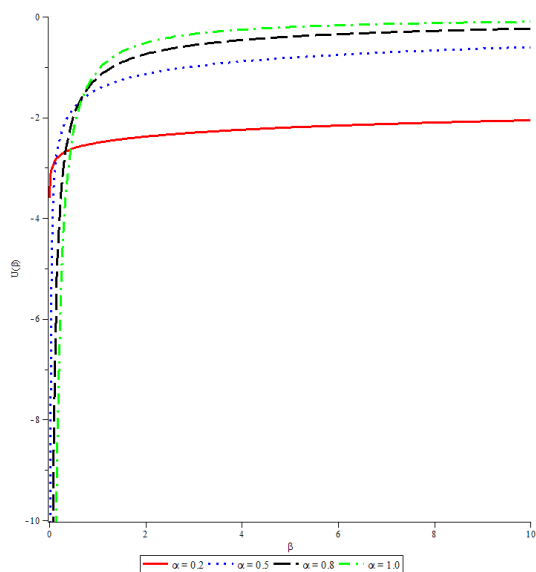
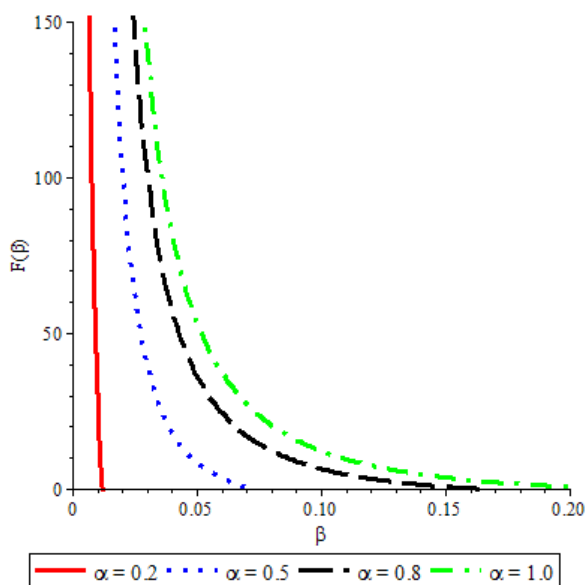**Figure 3.** The Conformable Internal Energy as a function of β for N_2 molecule for different values of α.
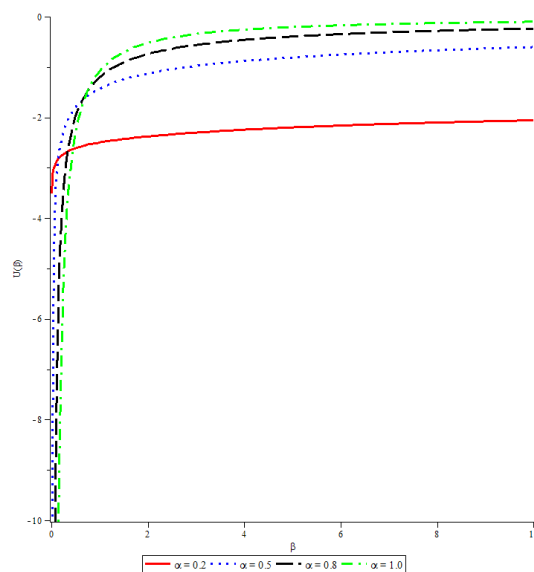

Figure 4. The Conformable Internal Energy as a function of β for CO molecule for different values of α.

reduced mass, and vibrational frequencies. Figures 3 and 4 display the mean vibrational energy $U(\beta)$ versus β for N_2 and CO, respectively. Notice that the energy decreases as β increases and, for all values of α, asymptotically approaches a constant value. For $\alpha = 1.0$, the energy curve starts at the smallest initial value and converges most rapidly, meaning that the system accesses a greater portion of vibrational states than for smaller α values. In contrast, for $\alpha = 0.2$ the energy is higher at the beginning and decays more slowly, reflecting the fact that fractional-order dynamics imposes restrictions on vibrational motion.

Similar trends can also be seen in the mean vibrational energy curves of both molecules; however, CO consistently shows a slightly higher energy value than N_2, especially in the low temperature regime (higher β). These deviations likely result from differences in molecular structure, reduced mass, and vibrational frequencies. Therefore, these results suggest that the influence of the fractional parameter α is modulated by the intrinsic properties of each diatomic molecule. In fact, in systems where vibrational interactions are stronger, more pronounced effects have been observed.


Figure 5. The Conformable Free Energy as a function of β for N_2 molecule for different values of α
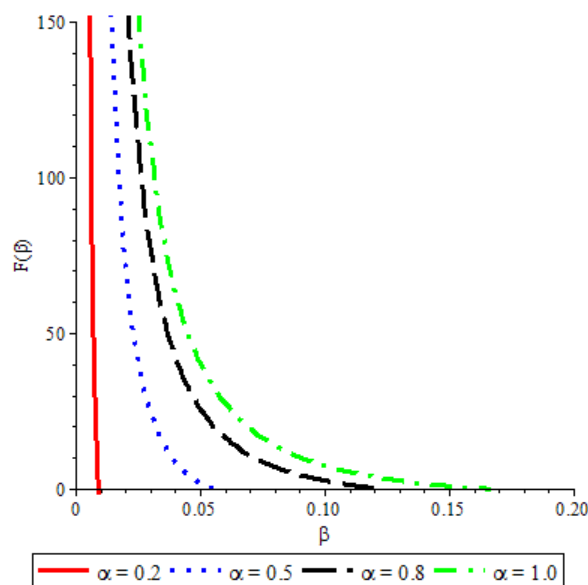

Figure 6. The Conformable Free Energy as a function of β for CO molecule for different values of α

Fig. 5 and Fig. 6 display the dependence of $F(\beta)$ on the β. For $\alpha = 1$, the classical case, $F(\beta)$ decreases rapidly as β increases. This behavior reflects the fact that a higher density of vibrational states is available, resulting in greater

thermal stability. As α is lowered, the free energy becomes considerably higher at every given β, this suggesting a lesser ability of the system to minimize its energy. While both the molecules show similar qualitative trends in $F(\beta)$, it is found that CO consistently shows higher values compared to N_2. This reflects the influence of molecular parameters, such as vibrational frequencies and bond strength. CO exhibits stronger vibrational coupling, hence its free energy is elevated compared to N_2, and this effect is much more pronounced for smaller α values. The entropy $S(\beta)$ versus β for N_2 and CO
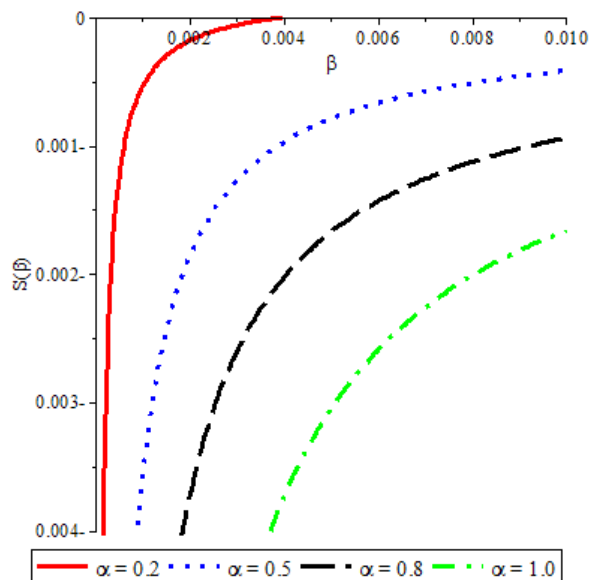
Figure 7. The Thermal Entropy as a function of β for N_2 molecule for different values of α
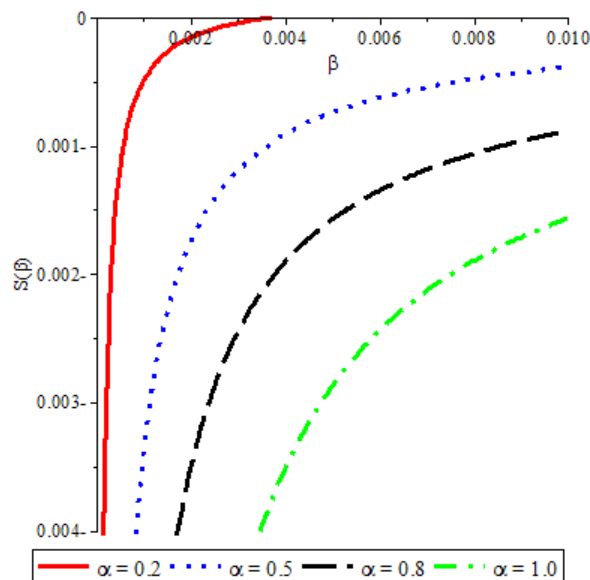
Figure 8. The Thermal Entropy as a function of β for CO molecule for different values of α

molecules is presented in Figs 7 and 8. For both molecules, the entropy exhibits clear trends related to the fractional order, α. For each molecule, an increase in α in the range from 0.2 to 1.0 results in a decrease in entropy at fixed β, meaning that higher fractional orders restrict the states accessible to the system and thus diminish randomness. At $\alpha = 0.2$, entropy is maximal, reflecting increased flexibility and more accessible states within the system.

Lowering β, which corresponds to a rise in temperature, results in an entropy increase across all α values, in accordance with thermodynamic expectations of increased disorder due to higher temperatures. The limit values of the entropy for small β are found to directly depend on α, reflecting the controlling role that fractional derivatives play in thermodynamics.

Compared to the other molecule, CO has marginally lower entropy than N_2. This is probably due to differences in molecular parameters such as mass or bond stiffness, which affect their quantum states. Finally, the variation of the specific
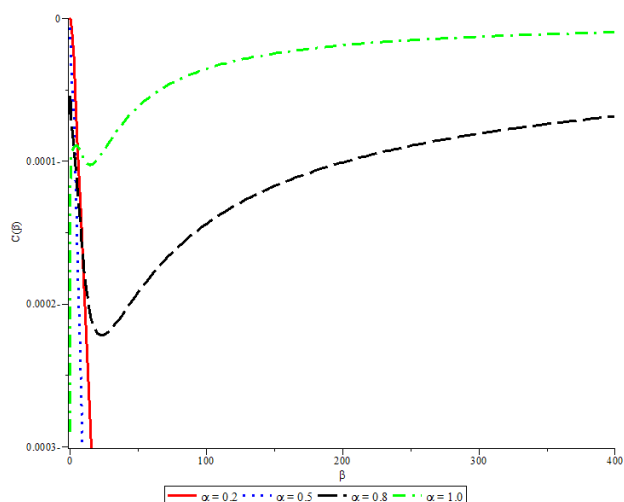
Figure 9. The Conformable Specific Heat as a function of β for N_2 molecule for different values of α
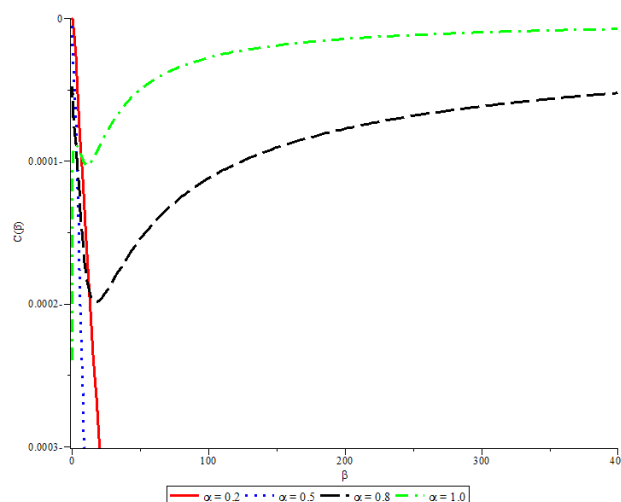
Figure 10. The Conformable Specific Heat as a function of β for CO molecule for different values of α

heat $C(\beta)$ versus β for N_2 and CO molecules clearly shows some interesting features in the thermodynamic behavior of the systems under the influence of fractional calculus. In fact, $C(\beta)$ exhibits different behavior depending on the value of α for both molecules.

For small values of β (high temperatures), the specific heat is small for all α since the system's energy levels are becoming fully populated and saturation effects start to set in. For higher values of β (lower temperatures), the specific heat begins to rise for higher values of α; the largest increase, for $\alpha = 1.0$, begins to dominate for higher values of β. In contrast, lower α values ($\alpha = 0.2$) yield reduced specific heat over the entire range, as expected from a more tightly bound energy distribution because of fractional effects.

When comparing N_2 and CO, the same qualitative trends are observed, but the magnitudes differ slightly; typically, N_2 has marginally higher values of specific heat at large β. This difference may be due to the variation in the molecular properties, such as mass, and vibrational frequencies, which determine the density of states and the energy distribution.

5. CONCLUSIONS

In this paper, the conformable SE with the pseudoharmonic potential was solved using the NU method, considering conformable fractional derivatives. The fractional parameter α played an important role in modifying the energy spectrum and the thermodynamic properties of the molecular systems studied within this framework. Furthermore, using this approach, the energy eigenvalues were analytically obtained and subsequently used to evaluate the classical partition function. Starting from the partition function, important thermodynamic properties, such as conformable internal energy, conformable free energy, conformable entropy, and conformable specific heat have been analyzed for N_2 and CO molecules.

In future work, this approach can be extended to apply the generalized conformable derivative and the NU method to higher-dimensional quantum systems. Although our present study is confined to one-dimensional systems, multidimensional potentials can exhibit a richer behavior. The extension of the methods used here, could potentially provide deeper insight into more complex molecular or solid-state systems.

Conflicts of Interest

The authors declare that there are no conflicts of interest related to the research presented in this manuscript.

ORCID

Derar Altarawneh, https://orcid.org/0000-0002-7796-9181; **Eqab M. Rabei**, https://orcid.org/0000-0003-2777-8851

REFERENCES

[1] C.P. Onyenegecha, C.A. Onate, O.K. Echendu, A.A. Ibe, and H. Hassanabadi, "Solutions of Schrodinger equation for the modified Mobius square plus Kratzer potential," The European Physical Journal Plus, **135**, 289 (2020). https://doi.org/10.1140/epjp/s13360-020-00304-z

[2] A.N. Ikot, U.S. Okorie, I.B. Okon, L.F. Obagboye, A.I. Ahmadov, H.Y. Abdullah, K.W. Qadir, et al., "Thermal properties of 2D Schrödinger equation with new Morse interacting potential," The European Physical Journal D, **76**, 208 (2022). https://doi.org/10.1140/epjd/s10053-022-00533-0

[3] A. Arda, C. Tezcan, and R. Sever, "Schrödinger Equation with a Non-Central Potential: Some Statistical Quantities," The European Physical Journal Plus, Eur. Phys. J. Plus, **131**, 323 (2016). https://doi.org/10.1140/epjp/i2016-16323-0

[4] K.J. Oyewumi, B.J. Falaye, C.A. Onate, O.J. Oluwadare, and W.A. Yahya, "Thermodynamic properties and the approximate solutions of the Schrödinger equation with the shifted Deng–Fan potential model," Molecular Physics, **112**(1), 127–141 (2013). https://doi.org/10.1080/00268976.2013.804960

[5] I.B. Okon, O. Popoola, C.N. Isonguyo, and A.D. Antia, "Solutions of Schrödinger and Klein-Gordon Equations With Hulthen Plus Inversely Quadratic Exponential Mie-Type Potential," Physical Science International Journal, **19**(2), 1-27 (2018). https://doi.org/10.9734/PSIJ/2018/43610

[6] F. Ahmed, "Effects of Cosmic String on Non-Relativistic Quantum Particles with Potential and Thermodynamic Properties," Int. J. Theor. Phys. **62**, 142 (2023). https://doi.org/10.1007/s10773-023-05397-7

[7] I.J. Njoku, C.P. Onyenegecha, C.J. Okereke, A.I. Opara, U.M. Ukewuihe, and F.U. Nwaneho, "Approximate solutions of Schrodinger equation and thermodynamic properties with Hua potential," Results in Physics, **24**, 104208 (2021). https://doi.org/10.1016/j.rinp.2021.104208

[8] H.A. Mardi, N. Nasaruddin, M. Ikhwan, N. Nurmaulidar, and M. Ramli, "Soliton dynamics in optical fiber based on nonlinear Schrödinger equation," Heliyon, **9**(3), e14235 (2023). https://doi.org/10.1016/j.heliyon.2023.e14235

[9] Y. Yulianto, and Z. Su'ud, "The Analytical Solutions of the Schrodinger Equation for a Single Electron in the Nikiforov-Uvarov Framework," Jurnal Fisika, **10**(2), 1-10 (2020). https://doi.org/10.15294/jf.v10i2.25190

[10] M. Al-Hawamdeh, A. Akour, E. Jaradat, O. Jaradat, M. Al-Hawamdeh, and A. Akour, "Involving Nikiforov-Uvarov Method in Schrodinger Equation Obtaining Hartmann Potential," East European Journal of Physics, (2), 117-123 (2023). https://doi.org/10.26565/2312-4334-2023-2-10

[11] F. Yaşuk, C. Berkdemir, and A. Berkdemir, "Exact solutions of the Schrödinger equation with non-central potential by the Nikiforov–Uvarov method," J. Phys. A: Math. Gen. **38**, 6579 (2004). https://doi.org/10.1088/0305-4470/38/29/012

[12] S.H. Dong, *Factorization Method in Quantum Mechanics*, (Springer, Berlin, 2007).

[13] U.S. Okorie, E.E. Ibekwe, A.N. Ikot, M. C. Onyeaju, and E.O. Chukwuocha, "Thermodynamic Properties of the Modified Yukawa Potential," J. Korean Phys. Soc. **73**, 1211–1218 (2018). https://doi.org/10.3938/jkps.73.1211

[14] D. Altarawneh, A.A. Shukri, and A.N. Ikot, "Solution of the Woods -Saxon potential and its application for study of thermodynamic properties," Jordan Journal Of Physics, **17**(4), 395–402 (2024). https://doi.org/10.47011/17.4.2

[15] E.P. Inyang, E.P. Inyang, I.O. Akpan, J.E. Ntibi, and E.S. William, "Analytical Solutions of the Schrödinger Equation with Class of Yukawa Potential for a Quarkonium System Via Series Expansion Method," European Journal of Applied Physics, **2**(6), (2020). https://doi.org/10.24018/ejphysics.2020.2.6.26

[16] B. Hamil, B. Lütfüoğlu, and M. Merad, "Dunkl-Schrodinger Equation in Higher Dimension," (2024). https://doi.org/10.48550/arXiv.2409.12653

[17] A.F. Nikiforov, and V.B. Uvarov, *Special Functions of Mathematical Physics*, (Birkhauser, Basle, 1988).

[18] R. Khalil, M. Al Horani, A. Yousef, and M. Sababheh, "A new definition of fractional derivative," Journal of Computational and Applied Mathematics, **264**. 65–70 (2014). https://doi.org/10.1016/j.cam.2014.01.002

[19] K. Oldham, and J. Spanier, editors, *The fractional calculus. Theory and applications of differentiation and integration to arbitrary order*, (Dover Publications Inc., USA, 2006).

[20] K.S. Miller and B. Ross, *An Introduction to the Fractional Calculus and Fractional Differential Equations*, (John Wiley and Sons, New York, USA, 1993).

[21] I. Podlubny, *Fractional Differential Equations*, (Academic Press, San Diego, California, USA, 1999).

[22] R. Herrmann, *Fractional Calculus*, 2nd ed., (World Scientific, Singapore, 2014).

[23] A. Atangana, and D. Baleanu, and A. Alsaedi, "New properties of conformable derivative," Open Mathematics, **13**(1), 889–898 (2015). https://doi.org/10.1515/math-2015-0081

[24] D. Zhao, and M. Luo, "General conformable fractional derivative and its physical interpretation," Calcolo, **54**, 903-917 (2017). https://doi.org/10.1007/s10092-017-0213-8

[25] M. Lazo, and D.F.M. Torres, "Variational Calculus with Conformable Fractional Derivatives," IEEE/CAA Journal of Automatica Sinica, **4**(2), 340-352 (2016). https://doi.org/10.1109/JAS.2016.7510160

[26] A. Kajouni, A. Chafiki, K. Hilal, and M. Oukessou, "A New Conformable Fractional Derivative and Applications," International Journal of Differential Equations, **2021**, 624543 (2021). https://doi.org/10.1155/2021/6245435

[27] H. Karayer, D. Demirhan and F. Büyükkılıç, "Conformable Fractional Nikiforov–Uvarov Method," Communications in Theoretical Physics, **66**(1), 12 (2016). https://doi.org/10.1088/0253-6102/66/1/012

[28] K.J. Oyewumi, F.O. Akinpelu, and A.D. Agboola, "Exactly Complete Solutions of the Pseudoharmonic Potential in N-Dimensions," Int. J. Theor. Phys. **47**, 1039-1057 (2008). https://doi.org/10.1007/s10773-007-9532-x

[29] O. Olendski, "One-dimensional pseudoharmonic oscillator: classical remarks and quantum-information theory," Journal of Physics Communications, **7**, 045002 (2023). https://doi.org/10.1088/2399-6528/acce20

[30] J. Bao, and B.D. Shizgal, "Pseudospectral method of solution of the Schrödinger equation for the Kratzer and pseudoharmonic potentials with nonclassical polynomials and applications to realistic diatom potentials," Computational and Theoretical Chemistry, **1149**, 49-56 (2019). https://doi.org/10.1016/j.comptc.2019.01.001

[31] A. Ikot, U. Okorie, I. Okon, L. Obagboye, A. Ahmadov, H. Abdullah, K. Qadir, M.E. Udoh, and C.A. Onate, "Thermal Properties of 2D Schrodinger equation with New Morse Interacting Potential," The European Physical Journal D, **76**, 208 (2022). https://doi.org/10.1140/epjd/s10053-022-00533-0

[32] I.I. Goldman, and V.D. Krivchenkov, *Problems in quantum mechanics*, (Pergamon Press, New York, 1961).

[33] R.Sever, C. Tezcan, M. Aktaş, and Özlem Yeşiltaş, "Exact solution of Schrödinger equation for Pseudoharmonic potential," J. Math. Chem. **43**, 845–851 (2008). https://doi.org/10.1007/s10910-007-9233-y

[34] C. Berkdemir, A. Berkdemir, and J. Han, "Bound state solutions of the Schrödinger equation for modified Kratzer's molecular potential, Chemical Physics Letters, **417**, 326-329 (2006). https://doi.org/10.1016/j.cplett.2005.10.039

[35] U.S. Okorie, A.N. Ikot, G.J. Rampho, P.O. Amadi, and H.Y. Abdullah, "Analytical solutions of fractional Schrödinger equation and thermal properties of Morse potential for some diatomic molecules," Modern Physics Letters A, 36(07), 2150041 (2021). https://doi.org/10.1142/S0217732321500413

[36] M. Al-Masaeed, E. Rabei, and A. Al-Jamel, "Analytical Solution of Conformable Schrodinger Wave Equation with Coulomb Potential," Progr. Fract. Differ. Appl. **10**(1), 137-153 (2024). http://dx.doi.org/10.18576/pfda/100113

[37] E.E. Ibekwe, E.P. Inyang, J.B. Emah, A.O. Akpan, and O.J. Yawo, "Mass spectra and thermal properties of deformed Schrödinger Equation for pseudoharmonic potential," Sri Lankan Journal of Physics, **23**(2), 63-76 (2022). http://doi.org/10.4038/sljp.v23i2.8119

[38] I. Haouam, "On the conformable fractional derivative and its applications in physics," J. Theor. Appl. phys. **18**(6) (2024). https://doi.org/10.57647/j.jtap.2024.1806.74

[39] A. Al-Jamel, M. Al-Masaeed, E.M. Rabei, and D. Baleanu, "The effect of deformations of special relativity by conformable derivative," Revista Mexicana de Física, **68**(5), 050705 (2022). https://doi.org/10.31349/revmexfis.68.050705

СУМІСНЕ РІВНЯННЯ ШРЕДІНГЕРА З ПСЕВДОГАРМОНІЧНИМ ПОТЕНЦІАЛОМ ТА ЙОГО ТЕРМОДИНАМІЧНІ ВЛАСТИВОСТІ

Дерар Алтараунех[a], **Екаб М. Рабей**[b]

[a] Кафедра прикладної фізики, Технічний університет Тафіли, Тафіла, 66110, Йорданія

[b] Кафедра фізики, Факультет природничих наук, Університет Аль-аль-Байт, P.O. Box 130040, Мафрак 25113, Йорданія

У цій роботі метод Нікіфорова-Уварова (NU) використовується для отримання точного розв'язку відповідного радіального рівняння Шредінгера (SE) для псевдогармонічного потенціалу. Ми виводимо як енергетичні стани, так і відповідні хвильові функції, а результати порівнюємо з результатами, описаними в існуючій літературі, для випадку традиційної похідної ($\alpha = 1$). Крім того, отримані енергетичні стани використовуються для розрахунку конформної функції розподілу в класичній границі. Термодинамічні властивості, включаючи конформну вільну енергію Гельмгольца, конформну середню енергію, конформну ентропію та конформну питому теплоємність, обчислюються та аналізуються для молекул N_2 та CO.

Ключові слова: *метод Нікіфорова-Уварова; псевдогармонічний потенціал; термодинамічні властивості; конформна функція розподілу*

FUSION CROSS SECTIONS FOR ^{24}Mg + ^{208}Pb REACTION IN THREE–STAGE CLASSICAL MOLECULAR DYNAMICS MODEL

Jignasha Patel[a*], **Subodh Godre**[a], **Pinank H. Jariwala**[b]

^{a}Veer Narmad South Gujarat University, Surat - 395007, INDIA
^{b}Department of Physics, Navyug Science College, Surat - 395009, INDIA
*Corresponding Author e-mail: pateljignasha87@gmail.com

Fusion cross sections for heavy-ion reactions have been calculated in various classical and semi-classical models. In the classical approach fusion cross sections have been calculated using different model such as Classical Molecular Dynamics (CMD), Classical Rigid-Body Dynamics (CRBD), a 3-Stage Classical Molecular Dynamics (3S-CMD) model and a microscopic Static Barrier Penetration Model (SBPM). In the present work 3S-CMD model is used to calculate fusion cross section. This model combines the advantages of both CMD and CRBD models. This model uses ion-ion potential obtained from dynamically evolving classical microscopic configurations of nuclei with a suitable NN-potential. The 3S-CMD model calculation proceeds in the following three stages: (1) Rutherford trajectory calculation at very large separation, followed by (2) CRBD calculation with rigid-body constraint on both nuclei up to distances close to the barrier, followed by (3) finding the trajectories of all the nucleons in a full CMD calculation for further evolution by numerically solving Coupled Newton's equations of motion for all the point nucleons. In the present work we have calculated fusion cross sections for ^{24}Mg + ^{208}Pb system in 3S-CMD model. Fusion cross sections have been calculated using a soft-core Gaussian form of NN-potential with the parameter set New Potential (NP). We also investigated the effect of this potential for ^{16}O + ^{92}Zr reaction which agree very well with the experimental fusion cross sections. The use of this NP parameter set might give better agreement in the case of 3S-CMD calculation of classical fusion cross sections for ^{24}Mg + ^{208}Pb reaction.

Keywords: *Fusion cross sections; Classical microscopic approaches; Heavy-ion reactions; Deformed nuclei*

PACS: 24.10.-i; 25.70.De; 25.60.Pj

1. INTRODUCTION

Fusion cross sections for heavy-ion reactions have been calculated in various classical and semi-classical models. In the classical approach fusion cross sections have been calculated using different model such as Classical Molecular Dynamics (CMD) [1], Classical Rigid-Body Dynamics (CRBD) [2], a 3-Stage Classical Molecular Dynamics (3S-CMD) [3] model and a microscopic Static Barrier Penetration Model (SBPM) [4]. In the present work 3S-CMD model is used to calculate the fusion cross section. This model combines the advantages of both CMD and CRBD models. This model uses ion-ion potential obtained from dynamically evolving classical microscopic configurations of nuclei with a suitable NN-potential.

The 3S-CMD model calculation [3] proceeds in three stages: (1) Rutherford trajectory calculation at very large separation, followed by (2) CRBD calculation with rigid-body constraint on both nuclei up to distances close to the barrier, followed by (3) finding the trajectories of all the nucleons in a full CMD calculation for further evolution by numerically solving Coupled Newton's equations of motion for all the point nucleons.

In the present work, we calculate fusion cross sections for the ^{24}Mg + ^{208}Pb system in the 3S-CMD model. Fusion cross sections are calculated using classical approximations and compared with the experiments. Fusion cross sections for many reactions have been calculated using a soft-core Gaussian form of NN-potential (eq.(1)), with the parameter set P4 [2]. However, the calculated fusion cross sections do not match with the experimental data for many reactions at different energies [5].

In the present work we have used a parameter set P4 and a new potential parameter set (called as NP) from ref. [6]. Using this NP potential, the fusion cross sections calculated for the ^{16}O + ^{92}Zr reaction in ref. [6] shows good agreement with the experimental data. The use of this NP parameter set might give better agreement in the case of 3S-CMD calculation of classical fusion cross sections for the ^{24}Mg + ^{208}Pb reaction.

2. CALCULATION DETAILS
2.1. Nucleon-Nucleon potential

The soft-core Gaussian form of NN-potential is given by

$$V_N(r_{ij}) = -V_0 \left(1 - \frac{C}{r_{ij}} \right) \exp\left(-\frac{r_{ij}^2}{r_0^2} \right), \tag{1}$$

where V_0, C and r_0 are respectively, the depth parameter, repulsive-core radius and range parameter. The parameters V_0, C and r_0 are chosen so that the NN-potential reproduces gross properties of the nuclei in their ground state such as, the ground state binding energy, the rms radius etc.

The Coulomb potential between protons has the form

$$V_C\left(r_{ij}\right) = \frac{1.44}{r_{ij}}(MeV) \tag{2}$$

is also added to the two-body potential.

^{24}Mg + ^{208}Pb reaction has been studied with the potential parameter set P4 [1] and New Potential (NP) [6], which is shown in Table 1. In the present 3S-CMD calculation, the individual nuclei are first generated using the variational potential energy minimization code STATIC [7] and are further "cooled" using DYNAMIC [7] method. The nuclear configurations are generated using the parameter set P4 and NP which reproduces the ground state properties close to the experimental values (see Table 2).

Fusion cross sections are calculated using the classical formula [1]

$$\sigma_{\text{fusion}} = \pi b_{\text{cr}}^2, \tag{3}$$

where b_{cr} is the maximum (critical) impact parameter for which the two nuclei fuse.

Table 1. P4 and New Potential Parameter Set for the NN-potential of eq. (1).

POTENTIAL	V_0 (MeV)	C (fm)	r_0 (fm)
P4	1155	2.07	1.2
NP	900	1.95	1.2

2.2. Construction of nuclei in their ground state

Utilizing the "STATIC" minimization technique around 2000 ground state configurations for ^{24}Mg and ^{208}Pb are produced using the P4 and NP potential parameter sets. The calculated ground state properties of the ^{24}Mg and ^{208}Pb nuclei are presented in Fig. 1 and Fig. 2. Out of these 2000 ground state configurations in each case, the ones having quadrupole deformation β_2 value close to the experimental value is selected, which is indicated in Fig. 1 and Fig. 2 by a red circle. The generated ground state properties using both potentials are shown in Table 2.

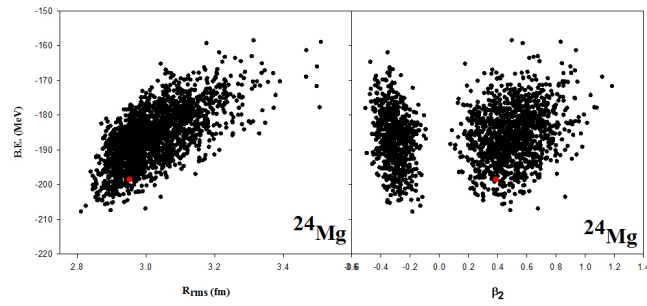**Table 2.** Ground state properties of ^{24}Mg and ^{208}Pb nuclei used in present calculation.

			BE (MeV)	R (fm)	β_2 (fm)
^{24}**Mg**	Cal.	P4	-198.72	2.94	0.37
		NP	-250.71	2.76	0.43
	Exp.		**-198.25[8]**	**3.07[9]**	**0.39[10]**
^{208}**Pb**	Cal.	P4	-1870.41	6.08	0.24
		NP	-2389.46	5.73	0.16
	Exp.		**-1636.46[8]**	**5.50[9]**	**0.00[10]**

From Table 2 it can be seen that the ground state binding energy, rms radius and β_2 of the chosen ^{24}Mg nucleus calculated using P4 potential are very close to the experimental values. None of the 2000 configuration generated for ^{208}Pb with potential P4 are very close to the experimental values of binding energy and rms radius. However, a configuration with quadrupole deformation $\beta_2 \approx 0$ is chosen which over estimates binding energy by 12% and rms radius by 6%.

In a similar way a configuration with quadrupole deformation $\beta_2 \approx 0$ is chosen for ^{24}Mg and ^{208}Pb for NP potential. For ^{24}Mg the binding energy is over estimates by 21% and rms radius is under estimates by 11%. For ^{208}Pb the binding energy is over estimates by 31% and rms radius is over estimates by 4%.

3. RESULTS AND DISCUSSION

^{24}**Mg + ^{208}Pb Reaction :** Fusion cross sections for ^{24}Mg + ^{208}Pb reaction calculated using P4 and NP potential parameter set and using eq.(2.1) are shown in Fig. 3 and 4 are compared with the experimental data of ref. [11]. The dynamical simulation is carried out in the 3S-CMD model.
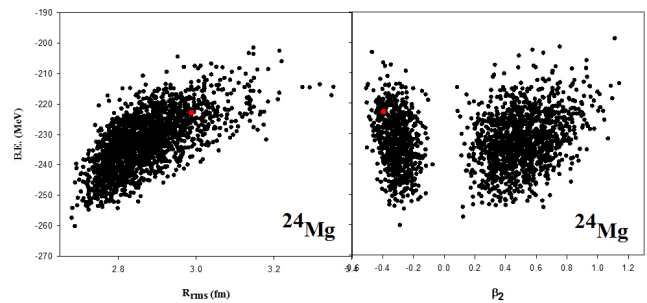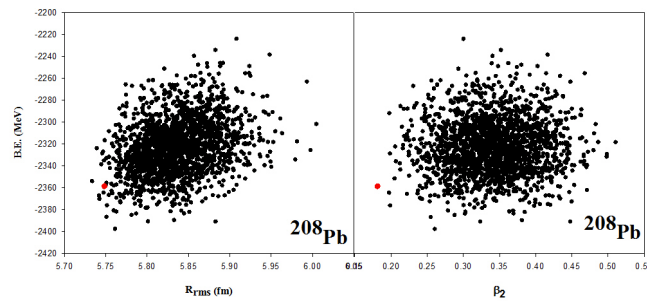
(a) Ground state configuration of ^{24}Mg
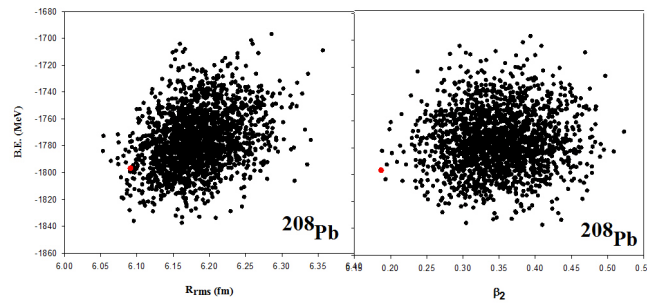
(b) Ground state configuration of ^{208}Pb

Figure 1. Ground state properties of the ^{24}Mg and ^{208}Pb nuclei generated by the "STATIC" method using P4 potential. Red circle indicate the ground state properties of the nuclei used in the present study.


(a) Ground state configuration of ^{24}Mg

(b) Ground state configuration of ^{208}Pb

Figure 2. Ground state properties of the ^{24}Mg and ^{208}Pb nuclei generated by the "STATIC" method using NP potential. Red circle indicate the ground state properties of the nuclei used in the present study.

For this system fusion cross-sections averaged over about 500 initial orientations for E_{CM} = 160-190 MeV and 1000 for E_{CM} < 160 MeV are determined using both potentials (P4 & NP) and are shown in Fig. 3.

Since the effect of reorientation is expected to be noticeable at collision energies near the Coulomb barrier, it is desirable to find fusion cross-sections at energies well below the lowest E_{CM} used in ref. [11]. Therefore, to clearly bring out the effect of reorientation, fusion cross-sections are determined in 3S-CMD calculation up to energies as low as 124.5 MeV, which is well below the lowest energy in the experiment by Back. For $E_{CM} \leq 124.0$ MeV, no pocket in the ion-ion potential is found in any of the 2000 initial random orientation that are considered. Therefore, fusion cross-section is assumed to be zero for $E_{CM} \leq 124.0$ MeV MeV in the 3S-CMD calculation for this system.

Fusion cross section calculated using potential parameter set P4 and eq.(2.1) in 3S-CMD model are highly over-estimated compared to the experimental data at all energy ranges. The reason for this overestimation is the larger rms radius of the ^{208}Pb produced in this calculation as compared to the experimental value (see Table 2). Fusion cross sections calculated using potential parameter set NP and eq.(2.1) in 3S-CMD model shows close agreement with the experimental data than the fusion cross sections calculated using P4 potential.
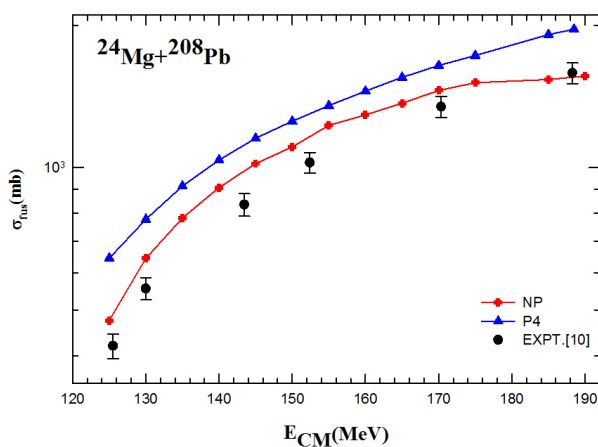
Figure 3. Fusion cross section for ^{24}Mg + ^{208}Pb reaction (log scale)
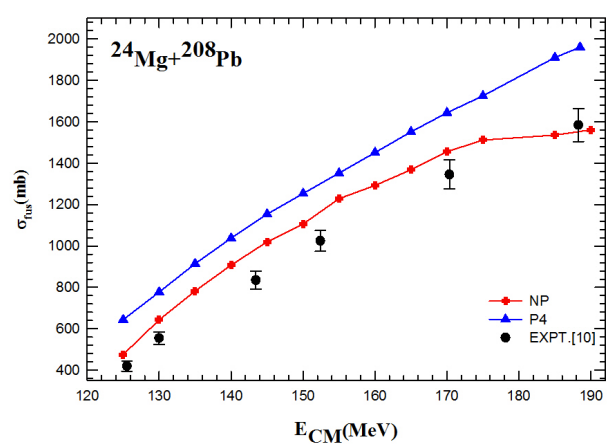
Figure 4. Fusion cross section for ^{24}Mg + ^{208}Pb reaction (linear scale)

4. CONCLUSIONS

Although fusion cross sections calculated using potential parameter set NP which gives good agreement for ^{16}O + ^{92}Zr reaction in ref.[6], however, it is slightly overestimated around the barrier energies for the medium heavy mass and heavy mass nucleus. i.e., ^{24}Mg + ^{208}Pb reactions.

However, it may be noted that the ground state properties of the nuclei generated using this potential (NP) are not close to the experiment values (see Table 2).

ORCID

 Jignasha Patel, https://orcid.org/0009-0008-1454-4283; **Subodh Godre**, https://orcid.org/0000-0001-5677-648X;
 Pinank H. Jariwala, https://orcid.org/0000-0003-1141-0761

REFERENCES

[1] S.S. Godre, and Y.R. Waghmare, "Classical microscopic calculations of ^{16}O+^{16}O and ^{40}Ca+^{40}Ca fusion cross sections," Phys. Rev. C, **36**, 1632 (1987). https://doi.org/10.1103/PhysRevC.36.1632

[2] P.R. Desai, and S.S. Godre, "Coulomb reorientation in near-barrier fusion of deformed+spherical systems in classical dynamical approach," Eur. Phys. J. A, **47**, 146 (2011). https://doi.org/10.1140/epja/i2011-11146-8

[3] M.R. Morker, and S.S. Godre, "Rotational and Vibrational Excitations of Colliding Nuclei in a Three-Stage Classical Molecular Dynamics Simulation," Proc. Symp on Nucl. Phys. **57**, 560-561 (2012). http://www.sympnp.org/proceedings/57/B86.pdf

[4] S.S. Godre, "Heavy-Ion Fusion Cross Sections in Microscopic Barrier Penetration Model," Nucl. Phys. A, **734**, E17-E20 (2004). https://doi.org/10.1016/j.nuclphysa.2004.03.009

[5] J.H. Patel, M.R. Morker, and S.S. Godre, "Near and above barrier fusion cross sections for ^{16}O+^{16}O and ^{16}O+^{208}Pb reactions in three-stage classical dynamical model," Proc. Symp on Nucl. Phys. **61**, 454-455 (2016). https://inspirehep.net/files/36e3a9830d547a60112fe0722874f366

[6] J.H. Patel, and S.S. Godre, "Fusion cross sections for ^{16}O+^{92}Zr reaction in three-stage classical molecular dynamics model," Proc. Symp on Nucl. Phys. **64**, 549-550 (2019). http://www.sympnp.org/proceedings/64/B115.pdf

[7] I.B. Desai, and S.S. Godre, "Ground-state properties of nuclei generated with a soft-core Gaussian form of NN potential," Proc. Symp on Nucl. Phys. **54**, 196-197 (2009). http://www.sympnp.org/proceedings/54/A72.pdf

[8] A.H. Wapstra, and K. Bos, "The 1977 atomic mass evaluation: in four parts part I. Atomic mass table. Atomic Data and Nuclear Data Tables," **19**(3), 177 (1977). https://doi.org/10.1016/0092-640X(77)90020-1.

[9] H. De Vries, C.W. De Jager, and C. De Vries, "Nuclear charge-density-distribution parameters from elastic electron scattering. Atomic Data and Nuclear Data Tables," **36**(3), 495-536 (1987). https://doi.org/10.1016/0092-640X(87)90013-1

[10] P. Möller, A.J. Sierk, T. Ichikawa, and H. Sagawa, "Nuclear ground-state masses and deformations: FRDM (2012)," Atomic Data and Nuclear Data Tables, **109–110**, 1-204 (2016). https://doi.org/10.1016/j.adt.2020.101393

[11] B.B. Back, R.R. Betts, J.E. Gindler, *et al*., "Angular distributions in heavy-ion-induced fission," Phys. Rev. C, **32**, 195 (1985). https://doi.org/10.1103/PhysRevC.32.195

ПЕРЕРІЗИ СИНТЕЗУ ДЛЯ РЕАКЦІЇ ^{24}Mg + ^{208}Pb У ТРИСТАДІЙНІЙ КЛАСИЧНІЙ МОДЕЛІ МОЛЕКУЛЯРНОЇ ДИНАМІКИ

Джигнаша Патель[a], **Subodh Годре**[a], **Пінанк Х. Джарівала**[b]

[a] Університет Південного Гуджарату імені Віра Нармада, Сурат - 395007, Індія

[b] Департамент фізики, Науковий коледж Навуг, Сурат - 395009, Індія

Перерізи синтезу для реакцій важких іонів були розраховані за допомогою різних класичних та напівкласичних моделей. У класичному підході перерізи синтезу були розраховані з використанням різних моделей, таких як класична молекулярна динаміка (CMD), класична динаміка твердого тіла (CRBD), 3-етапна модель класичної молекулярної динаміки (3S-CMD) та мікроскопічна модель проникнення статичного бар'єру (SBPM). У цій роботі для розрахунку перерізу синтезу використовується модель 3S-CMD. Ця модель поєднує переваги моделей CMD та CRBD. Ця модель використовує іон-іонний потенціал, отриманий з динамічно еволюціонуючих класичних мікроскопічних конфігурацій ядер з відповідним NN-потенціалом. Розрахунок моделі 3S-CMD відбувається у такі три етапи: (1) розрахунок траєкторії Резерфорда на дуже великій відстані, потім (2) розрахунок CRBD з обмеженням твердого тіла на обох ядрах до відстаней, близьких до бар'єру, а потім (3) знаходження траєкторій усіх нуклонів у повному розрахунку CMD для подальшої еволюції шляхом чисельного розв'язання зв'язаних рівнянь руху Ньютона для всіх точкових нуклонів. У цій роботі ми розрахували перерізи синтезу для системи ^{24}Mg + ^{208}Pb у моделі 3S-CMD. Перерізи синтезу були розраховані з використанням м'якої гауссової форми NN-потенціалу з набором параметрів Новий потенціал (NP). Ми також дослідили вплив цього потенціалу на реакцію ^{16}O + ^{92}Zr, які дуже добре узгоджуються з експериментальними перерізами синтезу. Використання цього набору параметрів NP може забезпечити кращу узгодженість у випадку розрахунку 3SCMD класичних перерізів синтезу для реакції ^{24}Mg + ^{208}Pb.

Ключові слова: *перерізи синтезу; класичні мікроскопічні підходи; реакції важких іонів; деформовані ядра*